DISTRIBUTED POWER ELECTRONICS FOR EXTENDED EFFICIENCY AND LIFETIME OF UTILITY-SCALE PHOTOVOLTAIC SYSTEMS

MD Nazmul Hasan

UNIVERSITAT ROVIRA i VIRGILI

Distributed Power Electronics for Extended Efficiency and Lifetime of Utility-Scale Photovoltaic Systems

MD NAZMUL HASAN

DOCTORAL THESIS

2019

UNIVERSITAT ROVIRA I VIRGILI
DISTRIBUTED POWER ELECTRONICS FOR EXTENDED EFFICIENCY AND LIFETIME OF UTILITY-SCALE PHOTOVOLTAIC SYSTEMS
MD Nazmul Hasan

MD NAZMUL HASAN

Distributed Power Electronics for Extended Efficiency and Lifetime of Utility-Scale Photovoltaic Systems

Ph.D. Thesis

Supervisors:

Professor Dr. Carlos Olalla Martínez

Professor Dr. Luis Martínez-Salamero

Department of Electrical, Electronic and Automatic Control Engineering

Group of Automatic Control and Industrial Electronics (GAEI)

UNIVERSITAT ROVIRA i VIRGILI

Tarragona, Spain

March 2019

UNIVERSITAT ROVIRA I VIRGILI
DISTRIBUTED POWER ELECTRONICS FOR EXTENDED EFFICIENCY AND LIFETIME OF UTILITY-SCALE PHOTOVOLTAIC SYSTEMS
MD Nazmul Hasan

UNIVERSITAT ROVIRA I VIRGILI
ESCOLA TÈCNICA SUPERIOR D'ENGINYERIA
DEPARTAMENT D'ENGINYERIA ELECTRONICA, ELÈCTRICA I AUTOMÀTICA
Av. Països Catalans, 26 Campus Sescelades
43007 Tarragona

Luis Martínez Salamero i Carlos Olalla Martínez, professor catedràtic i investigador, respectivament, del Departament d'Enginyeria Electrònica, Elèctrica i Automàtica de la Universitat Rovira i Virgili.

Luis Martínez Salamero and Carlos Olalla Martínez, full professor and research associate, respectively, of the Department of Electronic, Electrical and Automatic Control Engineering of Universitat Rovira i Virgili.

FEM CONSTAR que aquest treball, titulat "Distributed Power Electronics for Extended Efficiency and Lifetime of Utility-Scale Photovoltaic Systems" i presentat per Md. Nazmul Hasan per a l'obtenció del títol de Doctor, ha estat realitzat sota la nostra direcció al Departament d'Enginyeria Electrònica Elèctrica i Automàtica d'aquesta universitat.

WE CERTIFY that the present study, entitled "Distributed Power Electronics for Extended Efficiency and Lifetime of Utility-Scale Photovoltaic Systems" presented by Md. Nazmul Hasan for the award of the degree of Doctor, has been carried out under our supervision at the Department of Electronic, Electrical and Automatic Control Engineering of this university.

Tarragona, 15 de febrer de 2019

Els directors de tesi doctoral

Doctoral thesis supervisors

Luis Martínez Salamero

Carlos Olalla Martínez

UNIVERSITAT ROVIRA I VIRGILI
DISTRIBUTED POWER ELECTRONICS FOR EXTENDED EFFICIENCY AND LIFETIME OF UTILITY-SCALE PHOTOVOLTAIC SYSTEMS
MD Nazmul Hasan

Acknowledgement

I would like to thank my supervisor Dr. Carlos Olalla, Professor, Department of Electrical, Electronic and Automatic Control Engineering, URV, Tarragona, Spain, for his total support and co-operation to materialize my PhD thesis. I also acknowledge that without his initiatives, advice and guidance, this thesis work would not have been possible. I am also indebted to him for his cordial supervision to write this thesis.

I would like to express my sincere gratitude to my second supervisor Professor Luis Martínez Salamero. All through my PhD tenure, he helped me with his depth knowledge and vast experience in the field of Electronics.

My sincere thanks goes to Professor Abdelali El Aroudi who provided me the information about the research group and encouraged me to join as a PhD researcher.

I would like to thank my fellow doctoral students for their feedback, cooperation and of course friendship. My thanks are to all staffs of GAEI laboratory of DEEEA, URV for their cooperation and material support.

Finally, I acknowledge my parents, close relatives and friends for their constant inspiration towards the completion of this work.

UNIVERSITAT ROVIRA I VIRGILI
DISTRIBUTED POWER ELECTRONICS FOR EXTENDED EFFICIENCY AND LIFETIME OF UTILITY-SCALE PHOTOVOLTAIC SYSTEMS
MD Nazmul Hasan

To my family and friends,

who trust bestowed upon me

UNIVERSITAT ROVIRA I VIRGILI
DISTRIBUTED POWER ELECTRONICS FOR EXTENDED EFFICIENCY AND LIFETIME OF UTILITY-SCALE PHOTOVOLTAIC SYSTEMS
MD Nazmul Hasan

Abstract

This thesis is focused on the mitigation of mismatch due to ageing in Photovoltaic (PV) systems. In the past, the degradation of the short-circuit current has been considered to be the main factor hindering the energy production of PV systems. Nonetheless, the dispersion of current also increases with ageing, and it has been the topic of past researches. Although estimations have been carried out using measurements at the module level, submodule level dispersion might be higher. This thesis obtains novel data at the submodule level and examines the differences with respect to the data reported in the past. It is shown that estimation of energy loss due to ageing based on module level dispersion data has been underrated and, considering submodule level mismatch data, lifetime energy improvement can be possible up to 4-6%. It is also pointed out that the lifetime of PV systems could be extended if the submodule level dispersions are treated efficiently. In order to mitigate the ageing mismatch in PV systems, an isolated dc-dc bidirectional low power unity gain converter is proposed. A design procedure and experimental realization of the converter is presented. A control scheme that allows bidirectional power flow is also proposed. High frequency ferrite core transformer provides the galvanic isolation between primary and secondary side of the converter. In addition, resonant inductors are integrated in the transformer which reduces the size and cost of the converter. Experimental results show power transfer efficiencies more than 90% for loads between 1 W to 8 W. The performance of the converter for mismatch mitigation is verified. In the laboratory, three prototype converters are employed in a PV module following the Differential Power Processing (DPP) PV-IP architecture approach. It is observed that the proposed converters can fully mitigate mismatch among three submodules and provide the maximum available power. The impact of the proposed technology for mitigation of ageing mismatch on Levelized Cost of Energy (LCOE) in PV systems is also discussed.

Contents

List of Figures

List of Tables

UNIVERSITAT ROVIRA I VIRGILI
DISTRIBUTED POWER ELECTRONICS FOR EXTENDED EFFICIENCY AND LIFETIME OF UTILITY-SCALE PHOTOVOLTAIC SYSTEMS
MD Nazmul Hasan

List of Abbreviations

PV	Photovoltaic
$\boldsymbol{I_{sc}}$	Short Circuit Voltage
$\boldsymbol{I_{mp}}$	Maximum Power Current
$\boldsymbol{V_{oc}}$	Open Circuit Voltage
$\boldsymbol{V_{mp}}$	Maximum Power Voltage
$\boldsymbol{P_{mp}}$	Maximum Power Point
LCOE	Levelized Cost of Energy
SD	Standard Deviation
CV	Coefficient of Variation
STC	Standard Test Condition
NOCT	Nominal Operating Cell Temperature
MPP	Maximum Power Point
FPP	Full Power Processing
DPP	Differential Power Processing
PDF	Probability Density Function
DCM	Discontinuous Conduction Mode
SEPIC	Single-ended Primary-Inductor Converter

SRC Series Resonant Converter

PRC Parallel Resonant Converter

SPRC Series Parallel Resonant Converter

ZVS Zero Voltage Switching

ZCS Zero Current Switching

FHA First Harmonic Approximation

PWM Pulse Width Modulation

PCB Printed Circuit Board

Chapter 1

Introduction

In order to combat the global warming issue and to cut the greenhouse effect, reducing fossil fuel use is a must. Solar energy, wind energy, hydro power, biomass and others are alternatives to finite non-renewable energy sources. In order to reduce the use of fossil fuels as much as possible, efficient use of renewable energy is essential. Usually, coupling of renewable energy to the power grid is accomplished by the use of power electronic converters. To some extent, improving the efficiency of renewable energy sources depends on power electronics technology.

Among the renewable energy sources, photovoltaic (PV) energy has been considered one of the most promising technologies. Extensive research has been done in order to improve the performance and to reduce the production costs of PV modules. Such investigations have induced a large decline of PV power production costs, which have resulted in an exponential increase of the global PV market in the recent years, as shown in Fig. 1.1. One of the characteristics that limits the performance of PV systems is its operating lifetime, which is considered to be typically 25 years. During this lifetime, PV modules do not provide constant energy. Their power production decreases linearly due to ageing down to 80% of the initial rated power at year 25. Ageing not only results in this linear degradation, but also causes mismatch in the current production of PV modules. This aspect is well known, but its effect is considered to be sufficiently small. Therefore, it is typically overlooked in PV system design.

In the literature [3], it has been shown that the yearly average power degradation of PV systems is -0.6%. Data regarding the ageing mismatch is also reported in the past, but with a lower level of detail. In [3], it has also been shown that the mismatch in short

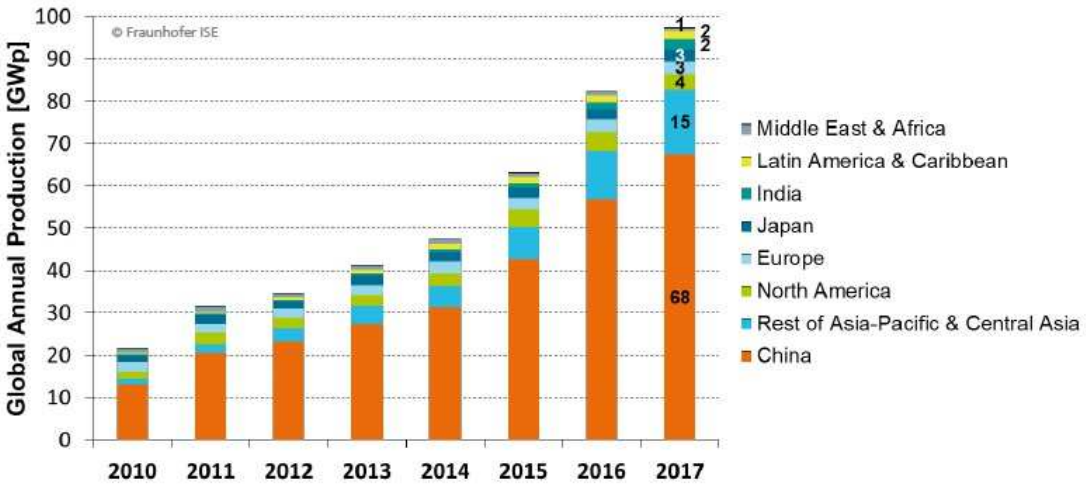

Figure 1.1. Global cumulative PV installation until 2017 (includes off-grid) (from [1]).

circuit current (I_{sc}) of PV modules increases with time up to a coefficient of variation (CV) of 10% at year 25. This research aims to further investigate the effects of ageing mismatch in the energy production of PV systems. The initial hypothesis is that ageing mismatch and its effects are larger than what has been predicted in the literature. If that hypothesis is correct, it may motivate the use of different power electronics architectures which can couple the PV system to the grid while mitigating the power loss due to mismatch.

In this research, the effect of ageing on PV modules is investigated by experimentally measuring I-V parameters of a PV system. The measurements are used to generate a statistical model that predicts the effects of ageing on mismatch. In addition, this thesis proposes a power electronic converter that can mitigate mismatches and improve the energy efficiency of PV systems.

1.1 Operation of Photovoltaic Systems

PV cells are semiconductor devices that convert light energy directly into electricity. Commercial PV cells are made of mono or poly crystalline silicon which can produce current in a range of 5-10 A. However the voltage across a PV cell is very low and below 1 V. The voltage-current and voltage-power curve of a typical PV cell are shown in Fig. 1.2.

PV modules are composed of many cells connected in series. Typically a PV module, as shown in Fig. 1.3, contains about 60 to 100 cells all in series, so that a larger voltage can be seen at the output, and power electronics converters can be used to adapt the system to the load or the grid. One important characteristic of the power converters, and

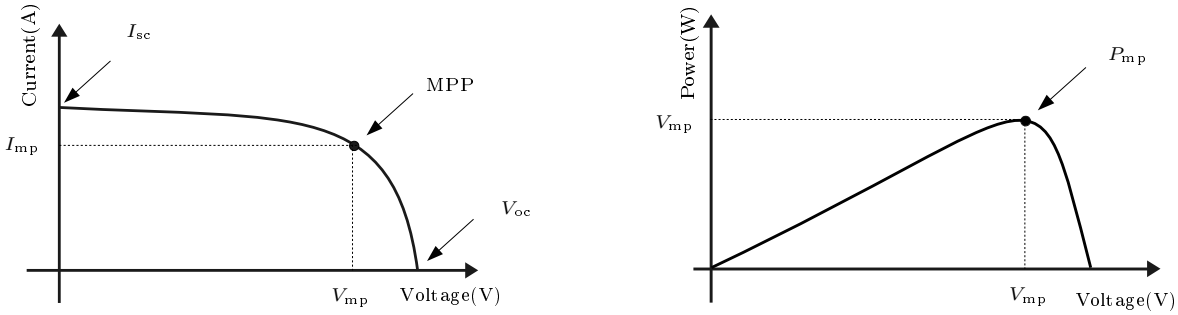

(a) V-I characteristics of PV cell. (b) V-P characteristics of PV cells.

Figure 1.2. PV cell characteristics.

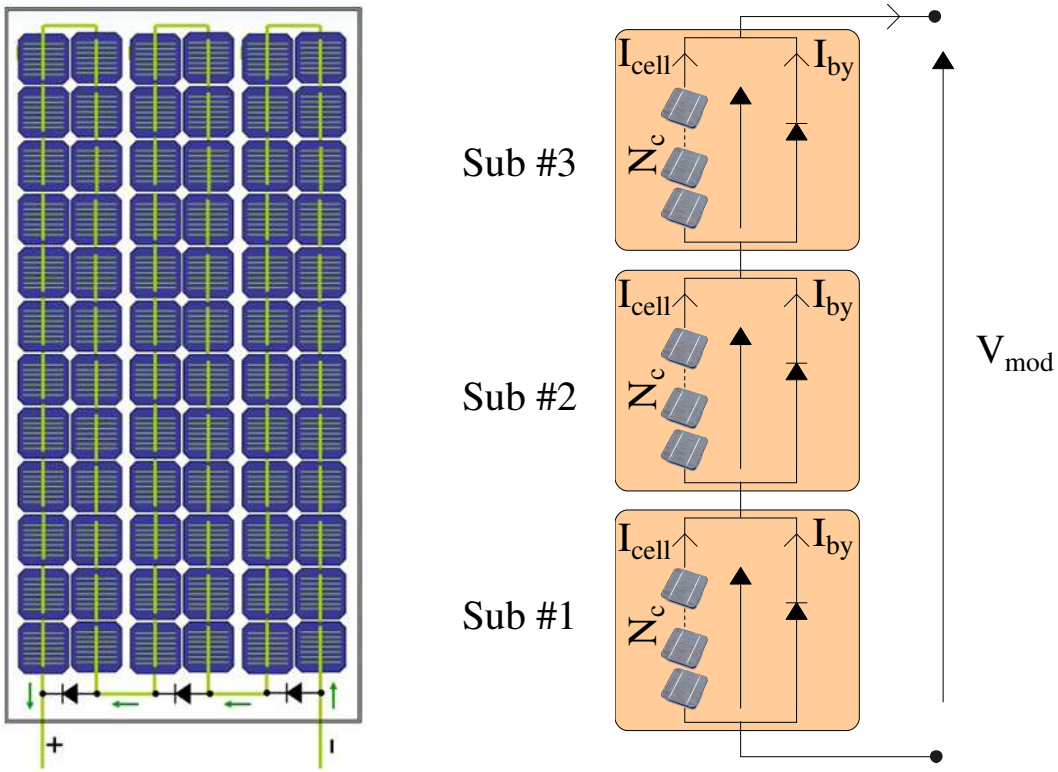

(a) Conventional PV module. (b) Series connected sub-strings.

Figure 1.3. PV module.

of PV systems in general, is that the installation cost usually decreases with an increasing number of PV modules in series. In that case, to get maximum power from a string of many PV modules connected in series each cell has to produce the same amount of current.

In case of series connected PV modules without mismatch, the same amount of current flows through each PV module. Therefore, at the output side of the PV system, sufficiently large amount of DC voltage can be seen while the current remains the same as it is for a single PV cell. This DC voltage is then inverted to AC voltage by an inverter and

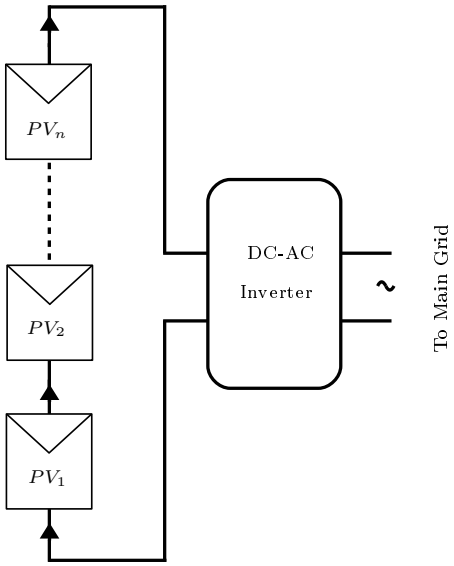

Figure 1.4. PV modules connected to the grid through an inverter.

connected to the main grid, as shown in Fig. 1.4. While conducting this operation, the voltage of the PV system is controlled in such a way that maximum power is transferred. Usually this is the standard operating condition for all PV systems. If current generation of the PV system is required to increase, more strings in parallel can be added.

However, the presence of mismatch among the cells due to dirt, manufacturing tolerances, partial shading, ageing and some other reasons, causes dispersion in current production. When such scenario happens, the overall current production of the module is dominated by the least current generated cell and the module is forced to generate a current close to that cell. Therefore, due to the series connections of the cells, a portion of available energy is lost within the cells. In case of severe mismatch conditions, due to hot spots induced by power losses on reverse-biased cells operating in breakdown [8], cell failures may occur, damaging the PV system. This risk of system failure is minimized by connecting bypass diodes in parallel with groups of cells which is known as a submodule or a substring. Typically, a module consists of two or three submodules. However, those bypass diodes cannot eliminate the power loss due to mismatch.

1.2 Effect of Ageing on PV Systems

Reduction in current production in one module or submodule by any means affects the whole PV system in such a way that the total power loss is higher than the loss caused by the affected module or submodule [3, 9, 10]. Since this research is focused on ageing

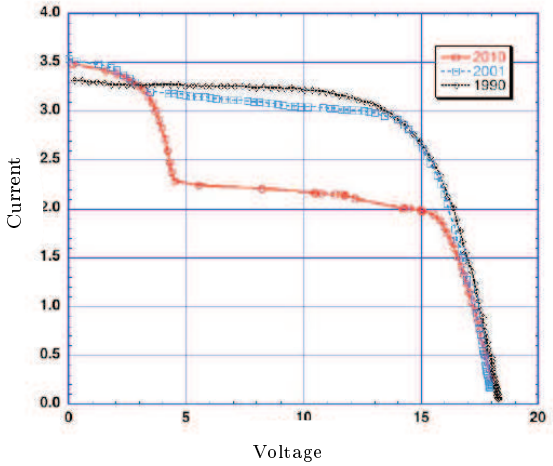

Figure 1.5. Comparison of V-I curves of a module after 11 and 20 years (from [2]).

related mismatch, a practical example case of mismatch due to ageing after 11 years and 20 years [2] is shown in Fig. 1.5. In the V-I curve of Fig. 1.5, it can be seen that the mismatch within the same module is so large that bypass diode is activated above 4 V. Besides of the corresponding power loss, due to the unconventional V-I curve of the PV system shown in figure, voltage versus output power characteristics may become nonconvex [10] with multiple maxima which limits the tracking of maximum power point of the system and thus results in overall power loss.

In general, the long-term performance of a PV system is affected by two key factors: degradation and mismatch. The degradation of power of PV module has to be sufficiently low in order to ensure low cost of energy. For instance, in the studies on the levelized cost of solar energy, it has been reported that the key factor is to keep this degradation rate below 1% per year [11]. Numerous researches based on experimental measurements have been done in order to characterize this degradation rate [2, 12, 13, 14, 15]. Based on these studies, it has been reported that the median degradation rate for Poly-Si modules lies within the range of 0.5-0.6%/year, while the mean degradation is slightly above, in the range of 0.8-0.9%/year [11]. In spite of having some level of skewness in the current and voltage parameters, populations are usually considered normal in those studies. Additionally, the degradation is usually assumed to be linear in time, although a higher begging-of-life decline in output power has been reported, specially in case of thin-film modules [16].

The dispersion of I-V parameters, such as the maximum power voltage (V_{mp}) and

current (I_{mp}), among the submodules is the second characteristic that affects the long term performance of PV systems. This dispersion may hinder the operation of maximum power point tracking (MPPT) of the system and thus reduce the overall efficiency of the system. However, it should be noted that, such a loss of available power is only because all modules are operated at the same current level, which does not correspond to their individual maximum power point due to dispersion. This loss can be recovered by distributed power electronic converters [4]. However, only few researchers have dealt with the dispersion characteristics of PV systems due to ageing [2, 12, 13]. In those papers, a linear increment of the coefficient of variation (CV) of the short-circuit current has been reported such that with an initial CV of 1%, PV systems end up with a CV of 10% after 25 years (0.36% per year). The impact of this dispersion has been shown to cause energy loss [4, 17, 18]. It has been reported that after 25 years, energy yield penalty is in the range of 2.5-3.0% of the total lifetime energy and the average power loss at year 25 is above 7%. It is important to note that those predictions consider module-level dispersion. In addition, the prediction of energy loss is based on the CV of short circuit current while modules operate at maximum power point current. It could be argued that the dispersion found in module level measurements is minimized by large number of cell connected in series, since the cells that are responsible for dispersion are, to some extent, compensated by the cells within the same module. Therefore, considering module level mismatch data for submodule level mismatch mitigation might be a conservative approach and submodule level measured CV of maximum power current may result in higher recoverable power loss due to the ageing mismatch.

1.3 Distributed Power Electronics in Mitigation of Partial Shading

To extract the maximum available power from a PV system affected by mismatch, several architectures based on distributed power electronics have been proposed in the recent past. For example, by employing dc optimizers [19, 20, 21, 22] as shown in Fig. 1.6(a), maximum available power can be extracted. This architecture can be introduced at the module [19, 20] or submodule level [21, 22]. However, in this architecture, the power converters have to process all the power associated with the system (and they are also

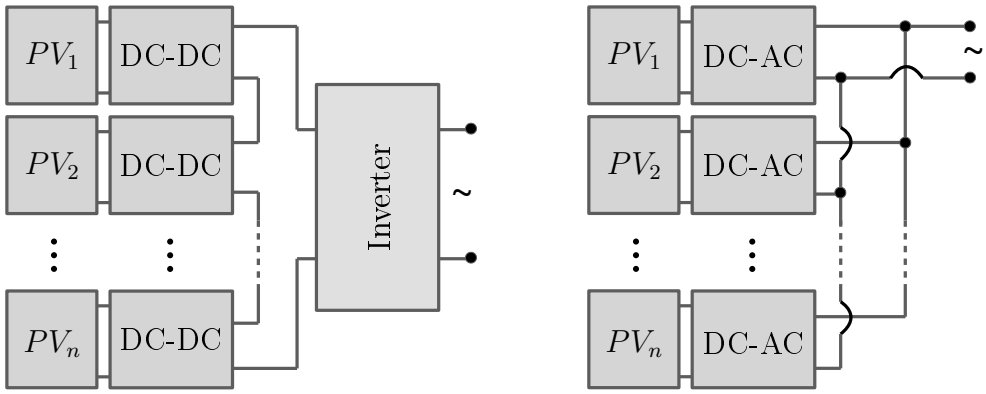

(a) PV system architectures with module/-submodule level dc optimizer.

(b) PV system architectures with module-level DC-AC inverters or micro-inverters.

Figure 1.6. Mismatch mitigation by FPP architecture.

known as full power processing (FPP) converters), hence the efficiency of the system relies mostly on the performance of the converters. For instance, if the converters can improve an efficiency of 3% and, due to the losses within the converters 3% power is lost, then the net energy yield improvement is equal to zero. A different type of FPP architecture based on DC-AC micro-inverters has been proposed in [23, 24, 25, 26, 27] as shown in Fig. 1.6(b). In this approach, the effect of mismatches can be reduced by compromising the insertion losses. But the limitation of FPP regarding system efficiency due to conversion losses remains. Nonetheless, one significant improvement is that, in this case, only one power conversion stage is required.

There is an alternative to the FPP architecture, where the original connection of the PV system remains the same while the power converters only process the mismatch power. The main current flows directly through the PV string and insertion loss is eliminated. This architecture is known as differential power processing (DPP) method. In DPP architecture, the converters are placed in parallel to submodules, and balance submodule voltages by matching submodule currents. DPP architectures have several advantages over FPP architecture. First, since they only process mismatch power, loss due to conversion does not have significant effect on the total energy improvement. Secondly, since DPP architectures process comparatively low power, the power rating of the distributed power converters can be significantly reduced and therefore, their corresponding cost is smaller. Figure 1.7 presents a comparative example of FPP and DPP architectures. It can be seen that, for the same mismatch condition, the FPP architecture has to process all the power of the PV modules, and the output power is 189.3 W. On the contrary, DPP converters

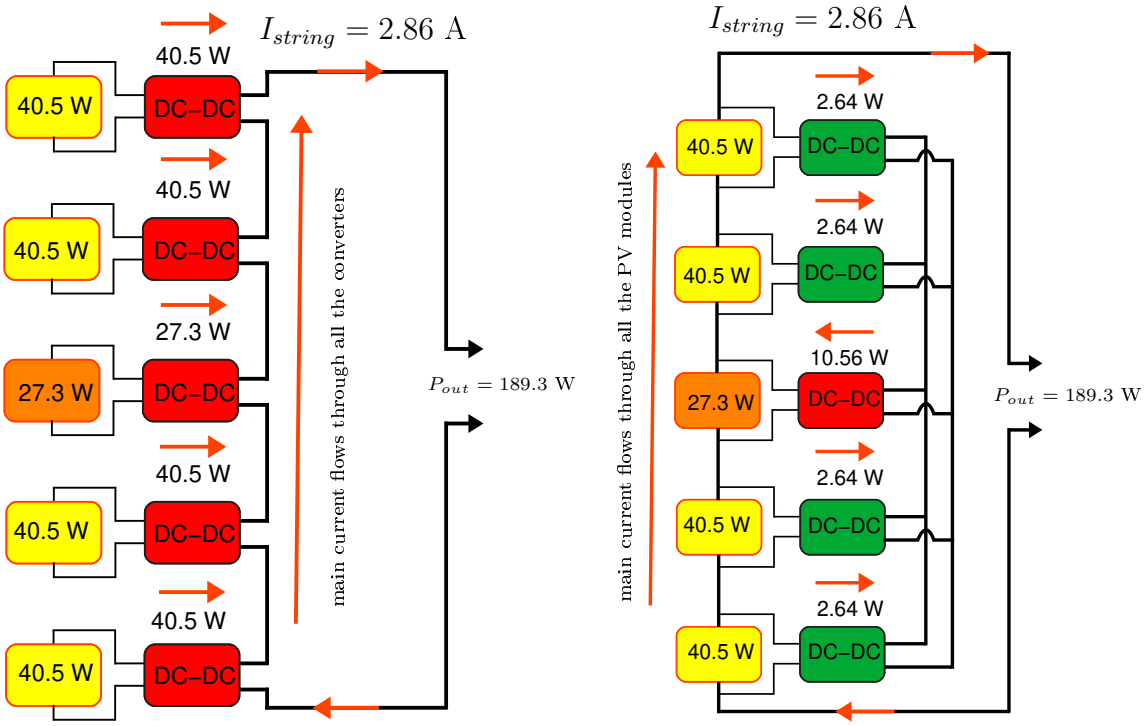

(a) Mismatch mitigation by FPP architecture (processes power 189.3 W).

(b) Mismatch mitigation by DPP architecture (processes power 21.12 W).

Figure 1.7. FPP Vs. DPP architecture in PV system mismatch mitigation.

only process the mismatch power of 21.12 W for the same output power.

A detailed comparison of FPP and DPP architectures has been presented in [17, 28]. It has been shown that 90% efficient DPP converters can extract 1-3% higher energy with respect to 97.5% efficient FPP converters. [17]. In addition to that, it has been reported that DPP architectures can be more cost effective than FPP since DPP converters process only 20-30% of full system power, which results in lower power rating converter requirement with low cost [17]. These architectures also have different impact on lifetime and reliability of PV systems. For example, the effect of power converter failure is not only limited to energy yield improvement, it might also have adverse impact on the whole PV system. The impact of these two different approaches on lifetime and reliability of PV systems has been investigated in [18]. It has been reported that in case of 5% converter failure rate after 25 years, the FPP approach gets severely affected. On the contrary, the DPP architectures can still provide significant mismatch mitigation, and yield more than 80% of the rated power even after 30 years [18, Fig. 7(b)].

Several DPP architectures have been proposed in the recent years. Of them, as shown in Fig. 1.8, three commonly used architectures are listed below.

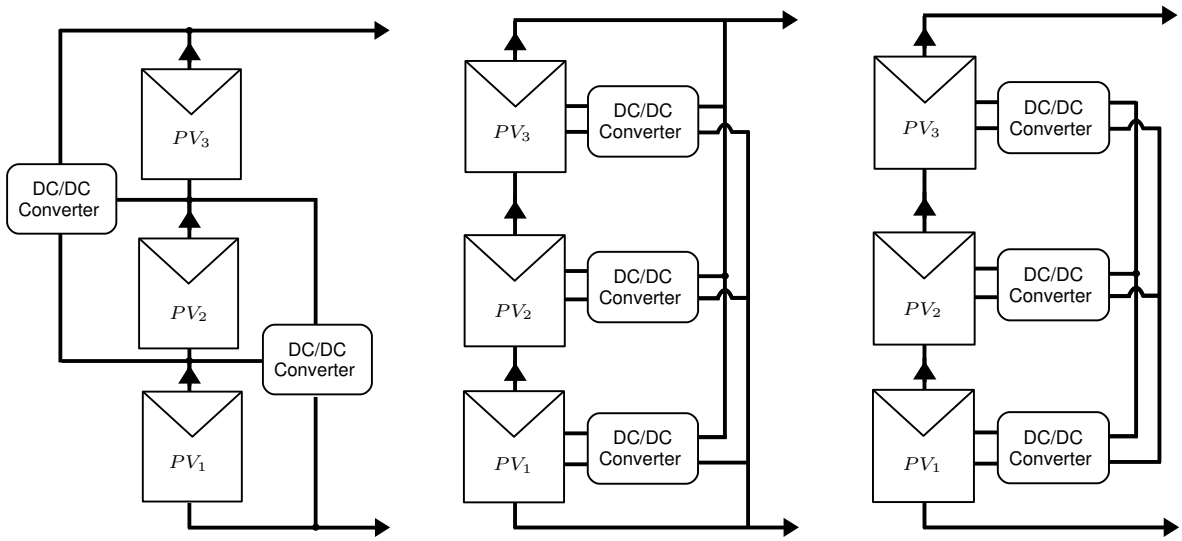

(a) PV-PV architecture. (b) PV-to-bus architecture. (c) PV-IP architecture.

Figure 1.8. Types of DPP architectures.

(i) PV-to-PV architecture

(ii) PV-to-bus architecture

(iii) PV-to-bus isolated port architecture (referred as PV-IP)

It is worth noting that these DPP architectures also suffer from several drawbacks. For example, although the PV-to-PV architecture requires one less converters than the number of substring in series, they process higher power due to their cascade connection [29, 30]. On the other hand, the PV-to-Bus and the PV-IP architectures require isolated power converters [31]. One significant drawback is that all DPP architectures require extra cabling between different modules.

Considering the discussion above, it is our interest to study the on-field application of distributed power electronics by means of a DPP architecture in case of ageing related mismatch mitigation.

1.4 Motivation and Objectives

The characterization of submodule level degradation and dispersion of I-V parameters is long due. In order to investigate the reliability and cost-energy ratio of PV systems on the long-term, characterizing degradation and dispersion of I-V parameters of PV systems with higher granularity, such as at submodule level is compulsory.

The first objective, treated in Chapter 2, is to characterize the ageing related dispersion in a PV system. In order to do that, a measurement procedure of submodule level I-V parameters is described. Considering the findings of the measurements, a simulation-based model is introduced in order to evaluate the effect of ageing on PV systems. A comparison between previous findings based on module level measurements with the new proposed model is also presented. The effect of ageing mismatch on the lifetime of a PV system is also evaluated in Chapter 2.

The second objective is tackled in Chapter 3. The aim is to design and implement a power electronics converter that can be used to mitigate submodule level ageing mismatch. To do that, the best DPP architecture is evaluated. Also, the optimum power rating of the converter and an appropriate topology is analyzed and presented in that chapter. The design procedure of the converter is explained and the experimental realization of the converter is also detailed. Finally, the performance of the converter is evaluated in the laboratory.

Chapter 4 discusses how the levelized cost of energy (LCOE) can be reduced by employing the proposed technology.

Finally, a summary of this research is presented in Chapter 5.

Chapter 2

Ageing Mismatch in PV Systems

The degradation rate of power production of PV systems due to ageing has been investigated and well documented. The studies have focused on the experimental measurement of module level data. Specifically, the degradation of the short-circuit current (I_{sc}) has been considered as responsible for the reduction in power production. However, the effect of dispersion of I_{sc} and I_{mp} at submodule level has not been explored so far. Therefore, the impact of these dispersion characteristics on energy yield prediction has not been analyzed yet. This chapter describes a measurement procedure, and presents the results of a series of measurements at submodule level that will allow to overcome that limitation. Finally, the effect of using power converters at submodule level on the lifetime of the PV system is also evaluated.

2.1 Introduction

There is an increasing interest in the study of the degradation characteristics of the parameters of PV modules aiming to predict the decrease of power production with time and, on the other hand, to circumvent this problem by introducing ad hoc corrective electronics. The decrease in power production in PV modules due to ageing is considered to be mainly the result of degradation of short circuit current. However, the dispersion in degradation rate of I_{sc} among the modules, expressed as coefficient of variation (CV), which can be defined as the ratio of the standard deviation (SD) to the mean (average), also increases due to ageing. This increased CV (or SD) of I_{sc} causes mismatch and therefore, is another source of power loss due to ageing of PV systems. Precise prediction

of energy capture requires the knowledge of degradation rate along with the increase rate of CV of PV parameters.

In order to observe the effect of ageing on I-V parameters of PV modules, many researchers have measured the parameters of new and old PV modules, exposed under open sky, at different atmospheric conditions [2, 11, 12, 13, 14, 15, 32], and degradation characteristics of PV parameters have been reported extensively. The dispersion characteristics of I-V parameters of PV modules, however, have not been considered in detail. In [33] 11 year-old PV modules have been measured to study the degradation characteristics of I-V parameters of PV modules. After 20 years of exposure, the same PV modules have been measured again in [2], where a consistent increase in SD of I_{sc} and maximum power point current (I_{mp}) have been reported. By averaging all the available data, it has been shown that the coefficient of variation of I_{sc} at module level increases with time from 1% to 10% in 25 years, which corresponds to a linear increment of 0.36% per year [3].

The results in [3] focus on degradation and do not discuss dispersion in detail. First, at maximum power the modules operate at I_{mp} and, therefore I_{mp} is likely to have more impact on PV module power generation. In addition to that, due to the concave V-I characteristics of PV cells, the CV of I_{sc} and I_{mp} measured at cell level may differ from that of the modules. The above discussions suggest that the recoverable loss due to ageing could be different from what has been predicted in the literature if submodule level ageing characteristics are being considered. However, no report has been published regarding submodule level degradation characteristics due to ageing.

In order to mitigate the mismatch due to ageing, power electronics can be deployed at submodule level. In the past, research has been done to improve the energy production by introducing power electronics at submodule level in the presence of partial shading [29, 31, 34, 35, 36]. Those papers have also investigated the energy capture in the presence of ageing related mismatch. It has been shown that 90% of the loss due to ageing can be regained by introducing submodule power converter with only 20% rating of the full power, and through the lifespan of a PV system almost 3% energy gain improvement can be possible [4, 17]. However, the results in [17] and [4] use models that employ module-level dispersion and can therefore be conservative.

In this chapter the dispersion of I-V parameters in terms of CV is examined at submodule level. The dispersion is assessed with experimental measurements, which are used

Table 2.1. Module and submodule parameters.

Electrical Data @STC (Model: TSM-230 PC/PA05)	Module	Submodule
Peak Power Watts-P_{MAX} (Wp)	230	76.67
Power Output Tolerance-P_{MAX} (%)	0/+3	0/+3
Maximum Power Voltage-V_{MP} (V)	29.2	9.73
Maximum Power Current-I_{MP} (A)	7.90	7.90
Open Circuit Voltage-V_{OC} (V)	37.1	12.37
Short Circuit Current-I_{SC} (A)	8.53	8.53
Module Efficiency η_m (%)	14.1	14.1

to develop more realistic models of ageing effects. The models are then used to predict the recoverable power loss.

The chapter is organized as follows. A procedure used to measure submodule level I-V parameters is described first. Then, the results obtained from the measurement are presented and analyzed. A statistical model is developed in order to predict available energy loss due to ageing. A prediction of the energy yield improvement is provided and a comparison with the existing literature is also discussed. Finally, simulation results are presented to justify that the use of submodule level power converters can extend the lifetime of PV systems.

2.2 Measurement Procedure

2.2.1 Submodule Specifications

The submodules measured in this research are poly-crystalline PV panels from Trina Solar Limited, model TSM 230 PC05. Each PV panel contains three submodules which are the combination of 20 cells (3x20). These modules were bought in May 2010 and installed in July 2010 in Universitat Rovira i Virgili, Tarragona, Spain (41.1189^0 N, 1.2445^0 E). The tilt angle of these solar panels is 15^0 with respect to the horizontal and they are oriented to south. The array is divided in two strings of 7 modules, connected to the grid through 2 StecaGrid 2000+ inverters. The individual junction boxes of the modules are modified with additional connectors so that the submodules can be accessed in order

Figure 2.1. Sample of the module string under measurement.

to carry out the measurement without changing their mechanical position and electrical characteristics. The datasheet parameters of the PV panel at standard test conditions (STC: Air Mass AM 1.5, irradiance 1000 W/m^2, cell temperature 25^{0}C) are presented in Table 2.1. Submodule datasheet parameters at STC, derived from the module data are also shown in Table 2.1. Some of the modules under measurement are shown in Fig. 2.1.

2.2.2 Measurement Procedure

The measurements are carried out under clear sky, within two hours of solar noon, and with irradiance above 800 W/m^2. Before measuring, the modules are cleaned with non reactive liquid to remove dirt. Temperature, voltage and current of the submodule under test are measured according to the IEC-60904 standard [37, 38], with tolerances below 0.5^{0}C for temperatures and below 0.2% for voltages and currents.

The connection diagram of the measurement is shown in Fig. 2.2. A voltage sweep is done by a programmable dc electronic load (BK precision 8512 (500 V/30 A/600 W)) to change the operating point of the PV submodules and the experimental data are recorded with a PPA 1520 power analyzer. As it can be seen in Fig. 2.2, also a temperature sensor

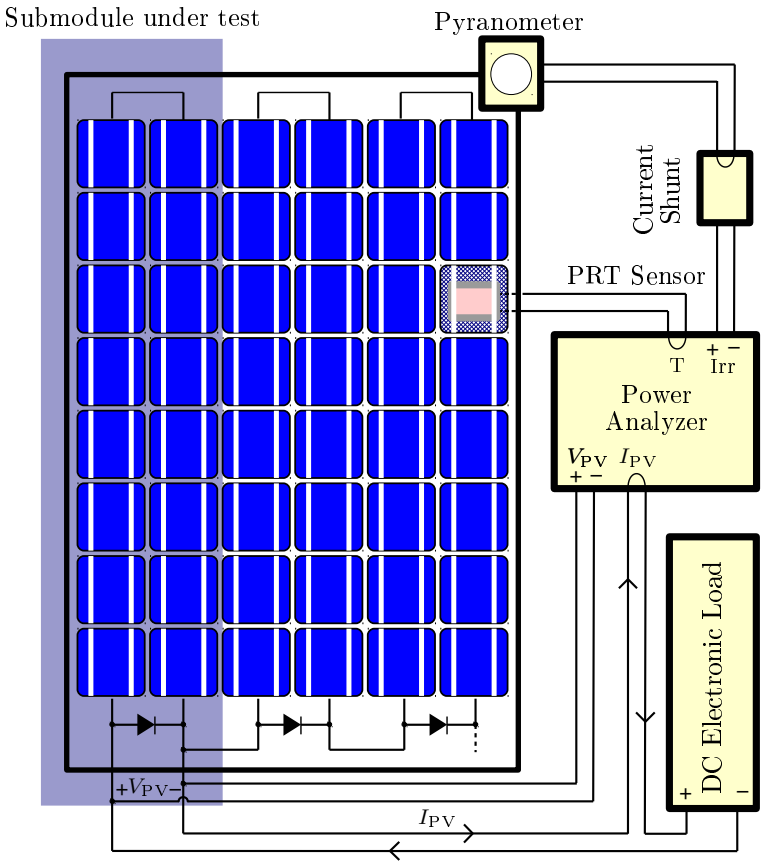

Figure 2.2. Block diagram of the measurement setup. PV module Trina TSM-PC05 230. Pyranometer Hukseflux SR11-TR. Temperature sensor: class A platinum resistance thermometer. DC load BK Precision 8512. Power analyzer and logging: N4L PPA 1520.

and a pyranometer are connected to the power analyzer. The temperature sensor (PT100) is attached to the back cover of the PV panel to record the temperature. Solar irradiance is recorded via a Hukseflux SR11-TR pyranometer. The SR11-TR pyranometer complies with the first class specifications of the ISO 9060 standard and the WMO Guide. The pyranometer is coupled to the plane of each individual PV module with an in-house developed coupling accessory so that the small position deviations between different modules do not affect the results. A current shunt (HF01A from Newtons4th) is used along with the pyranometer to improve the accuracy of the irradiance reading. All the instruments are calibrated at the time of the measurements.

For each submodule measurement, 15 voltage steps are set by the electronic load with a delay of 100 ms for each step which results in 1.5 seconds. Data acquisition is done at a frequency of 200 Hz by the data logger. Extra care is taken in the case of moving the pyranometer from submodule to submodule in order to avoid shading, given that the instrument exhibits very long settling time. Also, it is verified that the maximum

Table 2.2. Adaptation Table.

Parameters	Correction for	Correction factor
V_{oc}	Module temperature	$0.32\%/^0$C
I_{sc}	Module temperature	$0.047\%/^0$C
I	Solar Irradiance	(1000 W/m^2)/ (Actual Irradiance)

variation of irradiance during the measurement is 1 W/m^2 and the temperature variation is less than 1^0C [32].

2.2.3 Data Processing

The measured data are processed in two steps. First, to construct the V-I curve, the measured data are processed by an algorithm developed in MATLAB. The algorithm averages the multiple values captured at each step of the measurement sweep. For instance, three consecutive values of voltage with a tolerance of 10 mV are averaged and considered as one single data point, and the corresponding three current/irradiance/temperature are also averaged and taken into account. This improves the basic accuracy of the readings.

Secondly, in order to compare I-V parameters of different measurements, data are adapted (or normalized) to the Nominal Operating Cell Temperature (NOCT) of 45^0C, and considering an irradiance of 1000 W/m^2. Those conditions are very close to the real conditions of the measurements. The normalization are carried out by following the methods described by Zoellick [39] and Coleman [33], using the temperature correction factors provided in the datasheet of the PV modules, which are shown in Table 2.2.

Figure 2.3 shows the normalized (NOCT) V-I curves of the measured submodules, in 2017 (2.3(a)) and 2018 (2.3(b)). The data adapted to NOCT are used to extract the short circuit current (I_{sc}), the open circuit voltage (V_{oc}), and the maximum power current, voltage and power (I_{mp}, V_{mp} and P_{mp}). Adjustment of the current according to temperature is not necessary since the influence of small temperature changes on PV current is insignificant.

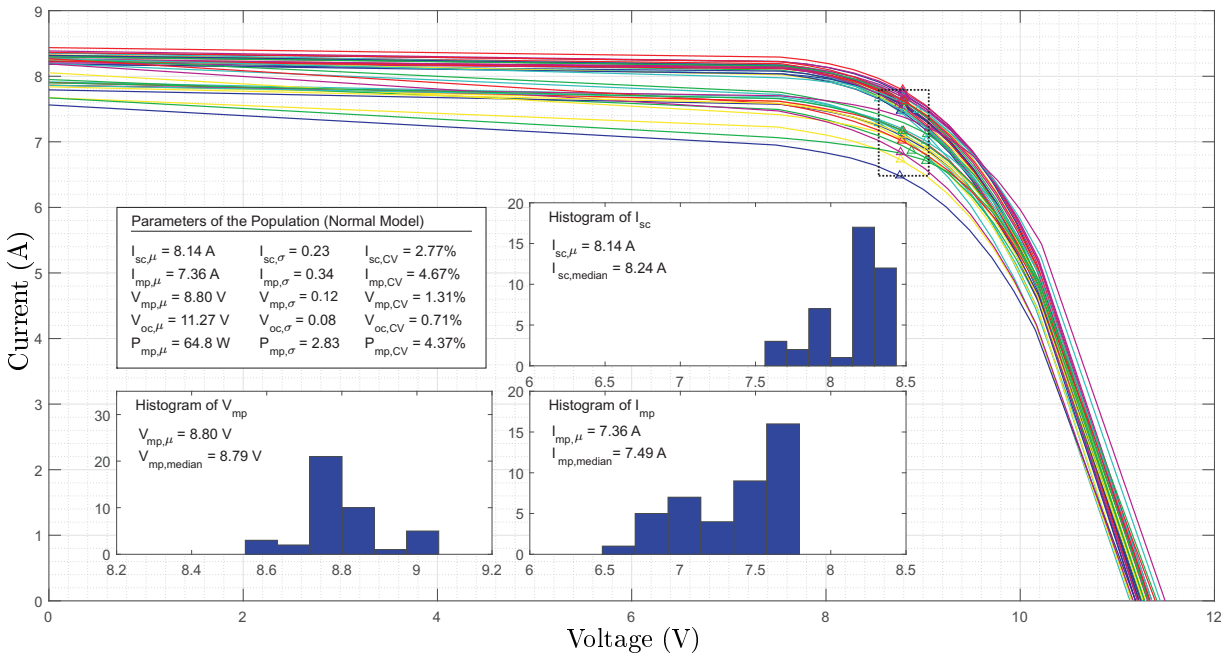

(a) Measurements in March 2017.

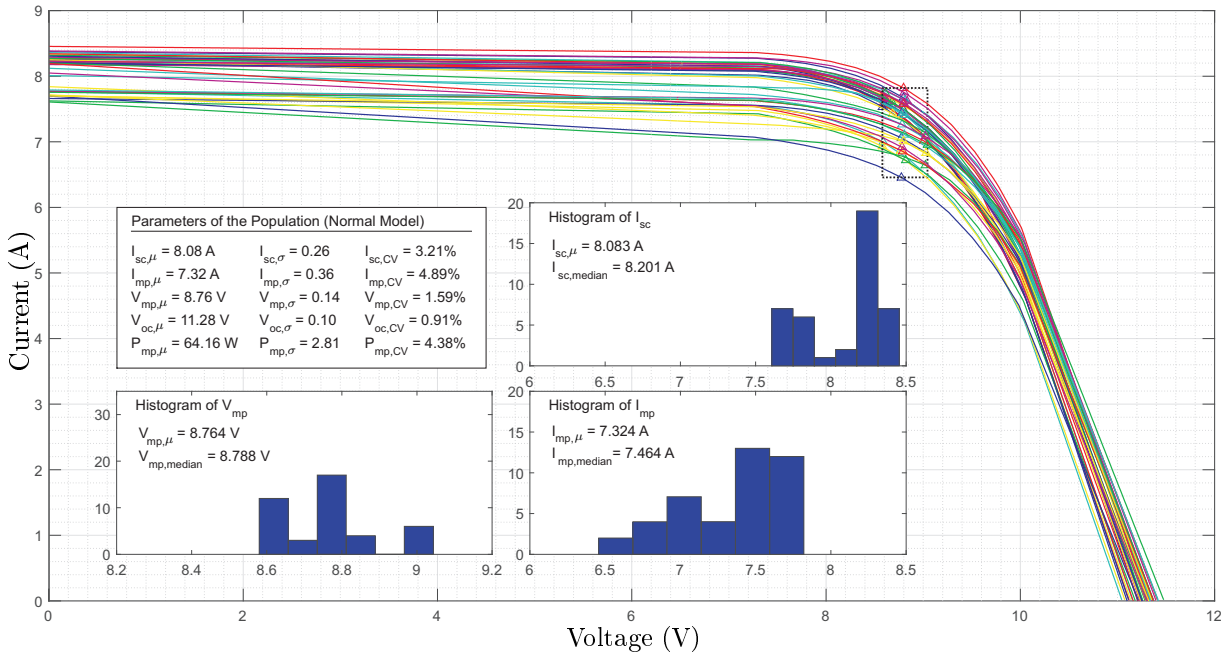

(b) Measurements in March 2018.

Figure 2.3. V-I curves of the 42 submodules, measured in 2017 (7 years old) and in 2018 (8 years old). The Δ marks point to the MPP of the curves, which are within the limits of the dotted black box. Four boxes describe the statistical attributes of the curves. The top left box shows the average value, the standard deviation and the coefficient of variation of I_{sc}, I_{mp}, V_{mp}, V_{oc}, and P_{mp}. The bottom left box shows the histogram of the 42 V_{mp} values, and compares the average and median values. The top and bottom right boxes show the histograms of I_{sc} and I_{mp}. In both cases, from the histogram and the median values it can be seen that the distribution presents skewness.

Table 2.3. Accuracy Table for PPA-1520.

Voltage
$Error$ = 0.05% Rdg + 0.1% Rng + (0.005% × kHz Rdg) + 5 mV [1]
Current
$Error$ = 0.05% Rdg + 0.1% Rng + (0.01% × kHz Rdg) + 300 µA
External shunt current sensor
$Error$ = 0.05% Rdg + 0.1% Rng + (0.005% × kHz Rdg) + 5 µV

[1] Rdg = meter reading, Rng = range employed in the instrument, 30 A rated instrument is used.

2.2.4 Accuracy and Precision of the Measurement Procedure

The accuracy and precision of the instrument are two fundamental aspects that need to be taken into account. In this section, the quality of the measurements is discussed. The data-logger used in this measurement is a Newtons4th 1520 power analyzer. The instrument contains a 30 A current sensor and a '×10' mode, which improves the accuracy of the readings. The derivations below show the basic accuracy of each reading carried out by the instrument, according to the accuracy table provided by the manufacturer manual as shown in Table 2.3.

Voltage Error: The voltage probe is attached directly to the submodule connectors. According to Table 2.3, the error of a voltage measurement, using the average value of V_{mp} in 2017, is:

$$\begin{aligned} V_{mp,error,2017} &= 8.80\ \mathrm{V} \times 0.05\% + 10\ \mathrm{V} \times 0.1\% + (0.005 \times 0) + 5\ \mathrm{mV} \\ &= 19.4\ \mathrm{mV} \\ \%\ error &= \frac{19.4 \times 10^{-3}}{8.8} \times 100\% \\ &= 0.22\% \end{aligned}$$

It can be seen that this error represents 0.22% of the V_{mp} measurement and is very close to the IEC 60904 standard (0.2%). Although the basic accuracy of one measurement is slightly above the requirements, several data points are averaged during the data processing, and our research focuses on the dispersion and degradation of current parameters of PV submodules. Therefore, maintaining the accuracy of the measurement of I_{sc} and I_{mp} within the standard is more relevant.

Current Error: From Table 2.3, and as an example, the error using the average value of I_{mp} in 2017, is equal to:

$$\begin{aligned} I_{mp,error,2017} &= 7.36\ \text{A} \times 0.05\% + 10\ \text{A} \times 0.1\% + (0.005 \times 0) + 300 \times 10^{-6}\ \text{A} \\ &= 14\ \text{mA} \\ \%\ error &= \frac{14 \times 10^{-3}}{7.36} \times 100\% \\ &= 0.19\% \end{aligned}$$

This error is slightly smaller than that of the voltage and within the limit specified by IEC 60904 standard (0.2%). In addition, the averaging of several data points further improves this basic accuracy of a single measurement.

Pyranometer Error: According to the datasheet, the accuracy of the irradiance measurement depends on a calibration uncertainty of ±1.8%. Nevertheless, the uncertainty accounts for the capability of the instrument to repeat the '*true*' value, whilst the precision (or the repeatability) of the measurement is more relevant in this case, since we are interested in differences between the current production of the different submodules. Hukseflux provides a method [40] that allows to evaluate the uncertainty of the measurement, which results in error of values around ±20 W/m^2 for irradiance above 1000 W/m^2. Also relevant to this case is the accuracy of the data-logger. Since the instrument outputs a 4-20 mA signal, we use a current shunt (HF01A) that allows to reduce the reading error to (for 1000 W/m^2):

$$\begin{aligned} I_{rr,error,2017} &= 0.05\% \times 14 \times 10^{-3} + 0.1\% \times 30 \times 10^{-3} + (0.005\% \times 0) + 5 \times 10^{-6} \\ &= 42\ \mu\text{A} \end{aligned}$$

Which is equivalent to 4.2 W/m^2.

Temperature Sensor Error: The temperature of each submodule has been sensed by the PT100 temperature sensor. The accuracy of the sensor is 0.1^{0}C ±0.05%. The real condition of the measurement is close to the NOCT, i.e. the cell temperature was close to 45^{0}C. Hence, the temperature error can be evaluated as

$$\begin{aligned} Temp_{error} &= 0.1^0\text{C} + 45 \times 0.05\% \\ &= 0.1225^0\text{C} \end{aligned}$$

Table 2.4. Measurement of I-V parameters of two consecutive days.

Parameter	Day 1	Day 2
The average I_{SC} (A)	8.1778	8.1788
The average I_{mp} (A)	7.4353	7.4527
STD of I_{SC}	0.18071	0.18078
STD of I_{mp}	0.27813	0.26917
CV of I_{SC} (%)	2.21	2.21
CV of I_{mp} (%)	3.74	3.61

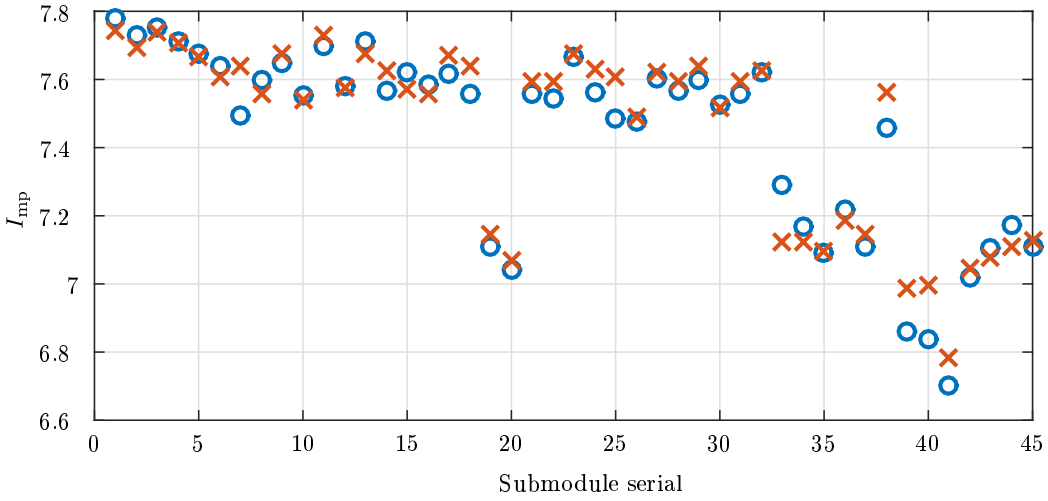

Figure 2.4. Distribution of I_{mp} from the measurements of two consecutive days.

According to Table 2.2, this negligible error in temperature measurement should not have significant effect on the voltage or current.

Discussion: It is important to note that the measurements are used to calculate differences among the parameters of submodules, so that accuracy (or error against the true value) of the results is not as important as their precision (or repeatability).

The repeatability of our measurement procedure are tested by carrying out two sets of measurements in two consecutive days (where ageing effect can be neglected), under similar temperature and clear sky irradiance conditions.

Table 2.4 shows the results of this experiment, where the average values of I_{sc} and I_{mp} are shown, along with their statistical characteristics assuming a normal model (standard deviation and CV). It can be seen that short-circuit average values are almost identical, although the maximum power point average currents show higher error (due to the moving

sweep that limits the amount of points for averaging). However, the STD and CV of the statistical model exhibit very minor differences.

Further detail of the precision of the I_{mp} measurements is given in Fig. 2.4, where the agreement between the I_{mp} measured at day 1 and day 2 can be observed. The mean tolerance is 0.2% and this results in a variation of the corresponding CV of only 0.13%.

2.3 Submodule Level Mismatch

In the previous section, the measured submodule level data are normalized to 1000 W/m^2 and NOCT condition. The findings from the measurement are presented in this section. Moreover, a comparison with existing literature is provided. It is worth mentioning that since there is no submodule level measurement data available till to date, all our submodule level measured data are compared with module level measured data that have been presented in previous studies. Two sets of measurements are presented. The first measurement was carried out in March 2017, when the PV modules were 7 years old. The second measurement was performed one year later, in March 2018.

2.3.1 Measurement Results

In Fig. 2.3, as expected, it can be seen that the voltage parameters V_{oc} and V_{mp} exhibit smaller standard deviation and CV with respect to the current parameters I_{sc} and I_{mp}. In consequence, the CV of P_{mp} is in good agreement with that of I_{mp}. In addition, the histograms in the figures show negligible differences between the average and the median values of V_{mp}, whereas there is some level of discrepancy between the average and the median values of I_{sc} and I_{mp}. This also agrees with the previously mentioned skewness of these parameters.

Table 2.5 shows a summary of the statistical results for every parameter, considering the average of measurements μ, the degradation of the average per year, the coefficient of variation and its change per year. No data of the first year of use is available, thus datasheet values are taken as a reference. It can be clearly seen how the current parameters I_{sc} and I_{mp} present large degradation rates around 1%, whereas the V_{oc} and V_{mp} remain mostly unaltered with time. After 8 years, the mean degradation rate of I_{sc} is -0.86%/year

Table 2.5. Statistical comparison of submodule parameters at NOCT: Datasheet, 7 years old and 8 years old.

Parameter	Year	I_{sc} (A)	I_{mp} (A)	V_{mp} (V)	V_{oc} (V)	P_{mp} (W)
Average μ	From Datasheet	8.68	7.94	8.77	11.3	69.58
	7 years old	8.14	7.36	8.80	11.27	64.8
	8 years old	8.08	7.32	8.76	11.28	64.16
μ Change	Datasheet v. 7 years	-6.22 %	-7.30 %	0.34 %	-0.26 %	-6.87 %
	Datasheet v. 8 years	-6.91 %	-7.81 %	-0.11 %	-0.18 %	-7.79 %
μ Change/year	Datasheet v. 7 years	-0.89 %	-1.04 %	0.05 %	0.04 %	-0.98 %
	Datasheet v. 8 years	-0.86 %	-0.98 %	-0.01 %	-0.02 %	-0.97 %
CV	From Datasheet	1 %	1 %	-	-	1 %
	7 years old	2.76 %	4.62 %	1.36 %	0.71 %	4.37 %
	8 years old	3.22 %	4.92 %	1.60 %	0.89 %	4.38 %
CV Change/year	Datasheet v. 7 years	0.25 %	0.51 %	-	-	0.48 %
	Datasheet v. 8 years	0.27 %	0.49 %	-	-	0.42 %

and that of I_{mp} is slightly above and equal to -0.98%. These values are in accordance with reported degradation rates of poly-Si modules [3].

A more significant result with respect to mismatch due to ageing can be observed in the CV values depicted in Table 2.5. First, the mismatch observed in I_{sc} and I_{mp} is significantly larger than that of V_{oc} and V_{mp}, in line with previous studies. However, the rate of increase of the CV of I_{sc} is 0.25-0.27% per year, a value slightly below the 0.36%/year reported at the module level in [3]. In contrast, the rate of increase of the CV of I_{mp} is well above those values and corresponds to 0.49-0.51%/year. This last result demonstrates that the CV of I_{mp} is larger than that of I_{sc}.

It has to be pointed out that the statistical analysis shown above considers that the Probability Density Function (PDF) that describes the set of measurements is normal. However, this hypothesis of normal distribution has to be validated. In order to do that, as an example, the distribution of maximum power point current is shown in Fig. 2.5 when the system is 7 years and 8 years old. In Fig. 2.5, it is quite evident that there is a difference between the mean and the median values of the maximum power current, which indicates a non-normal distribution since in a normal distribution the mean, median, and mode are equal. The distribution of I_{mp} shows negative skewness with a long tail of current values that exhibit significantly lower performance. This skewness is well known

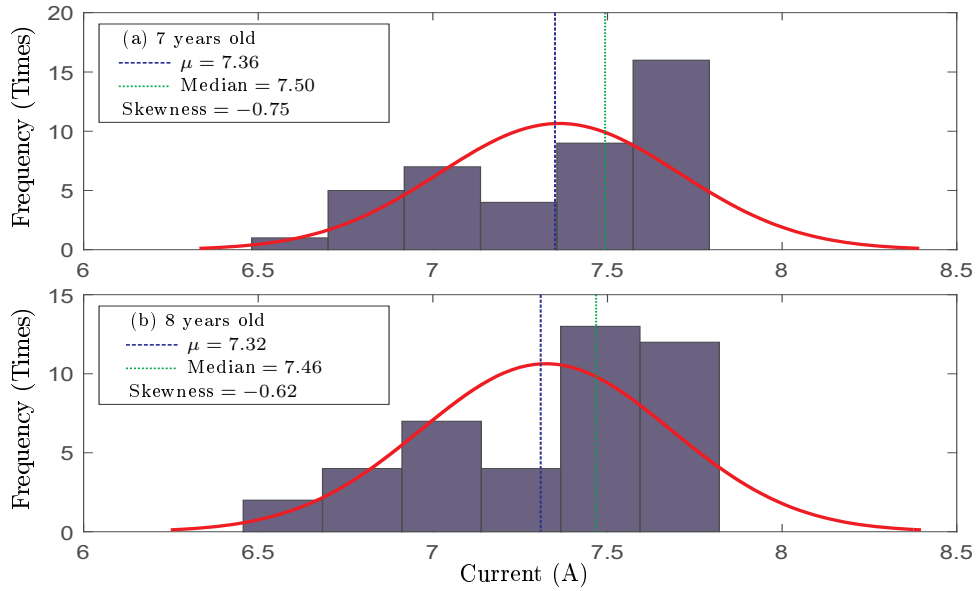

Figure 2.5. Histogram of the I_{mp} measurements when the system is 7 years old (a) and 8 years old (b). Red line: fitting of the measurements with a normal distribution. Blue dashed line: mean value. Green dotted line: median value.

and has been reported in the past [2, 32, 33, 41, 42].

In order to provide an appropriate statical model, in the following section we explore a probability density function in which skewness can be taken into account. The new probability density function is expected to provide better fitting of the PV parameters statistical data.

2.3.2 Submodule Level Mismatch Modelling

This subsection presents a subexponential heavy-tailed distribution [43] that can describe appropriately the properties of the measurements. Heavy tailed distributions have been used in the past in the context of PV systems, for example in [44]. In this research, only the measurements of I_{mp} are considered since the MPP current is the main parameter affecting the efficiency of PV systems. The results of Fig. 2.5 point to a negative skewness, which is in line with previous reports [3]. The distribution tends to include most of its contents within a small range around the median, whereas there is a decreasing chance of cases where the current is smaller. It is worth to point out that in our set of measurements, the histogram of I_{mp} shows an unexpected "gap" near the median. This gap should typically not exist [13] but, other than that, the measurements are in good agreement with the literature.

One-tailed arrangements, including the Weibull, Burr or the log-normal distribu-

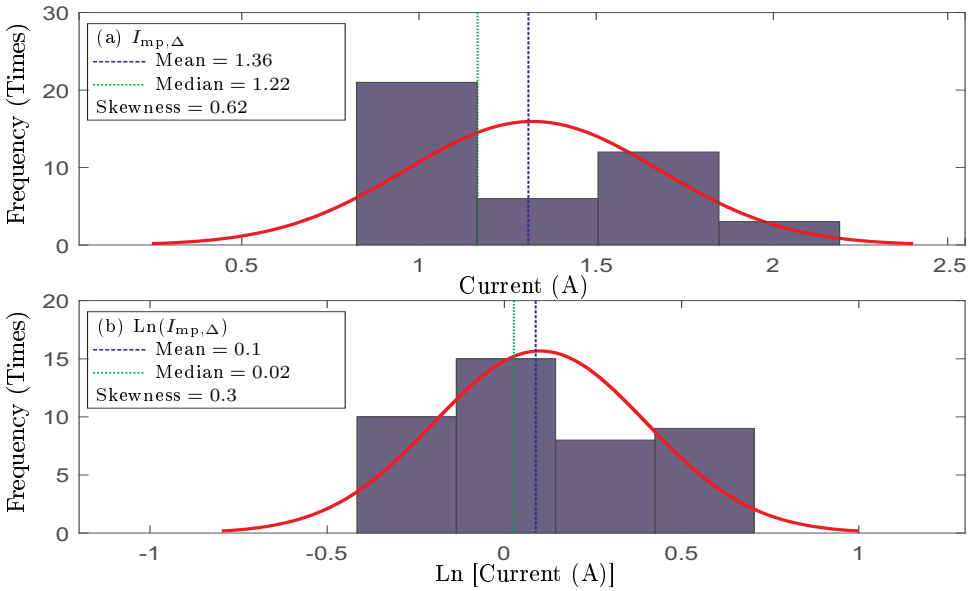

Figure 2.6. Histogram of $I_{\mathrm{mp},\Delta} = 8.68 - I_{\mathrm{mp}}$ when the system is 8 years old (a) and histogram of its natural logarithm (b). Red line: fitting of the measurements with a normal distribution. Blue dashed line: mean value. Green dotted line: median value.

tions [43], can be used to model such a probability density function. In that sense, the log-normal distribution presents the advantage that its relationship with the normal distribution can be used to characterize the PDF easily. Nonetheless, the log-normal distribution can only be used to represent positive skewness (i.e. right-tailed distributions), while Fig. 2.5 shows negative skewness. In order to adapt the probability density function describing the MPP current to the positive skewness of the log-normal distribution, the following transformation is carried out. The measurements are subtracted from the short-circuit current specified in the datasheet.

$$I_{\mathrm{mp},\Delta} = 8.68 - I_{\mathrm{mp}} \tag{2.1}$$

Fig. 2.6(a) shows the new histogram of the 8-years old $I_{\mathrm{mp},\Delta}$ measurements after the transformation. Now the x-axis points to the decrease of the MPP current with respect to the datasheet short-circuit current. In addition, the appropriateness of the log-normal distribution can be observed in Fig. 2.6(b), where the histogram of natural logarithm of the measurements is depicted. If the log-normal distribution is pertinent, then the logarithm of the variable presents a normal distribution [43]. Although some level of skewness (which is related to the aforementioned lack of measurements near the median in this set) still exists, it can be seen that the normal distribution is in good agreement

Table 2.6. Predicted statistical parameters after 1, 7, 25 and 50 years.

Parameter	Year 1	Year 7	Year 25	Year 50
$\Delta\mu$ (A)	0.74	1.32	2.68	4.61
CV (%)	1	4.62	12.45	25.5
σ	0.0794	0.3435	0.7477	1.0367
μ^*_Δ	-0.3068	0.2432	0.9473	1.5047
σ^*_Δ	0.1070	0.2563	0.2740	0.2219

with the histogram.

The log-normal distribution is characterized by its mean and standard deviation, noted μ^*_Δ and σ^*_Δ respectively. These parameters can be easily related to μ_Δ and σ_Δ from the normal distribution as follows [45]:

$$\mu^*_\Delta = \mathrm{Ln}\left(\frac{\mu^2_\Delta}{\sqrt{\sigma^2_\Delta + \mu^2_\Delta}}\right), \tag{2.2}$$

$$\sigma^*_\Delta = \sqrt{\mathrm{Ln}\left(\frac{\sigma^2_\Delta}{\mu^2_\Delta} + 1\right)}. \tag{2.3}$$

Considering that the changes of the 8-years old μ and CV of I_{mp} in Table 2.5 are linear (such as in [12]), the corresponding probability density function for $I_{\mathrm{mp},\Delta}$ along with modified versions of μ^*_Δ and σ^*_Δ for the proposed log-normal distribution after 1, 7, 25 and 50 years should present the parameters of Table 2.6. The parameters of the 7 years old distribution are verified in Fig. 2.7, where the histogram of $I_{\mathrm{mp},\Delta}$ from the measurements and a fitting of the log-normal distribution is carried out, using an equivalent maximum likelihood parameter estimation [46]. It can be seen that the parameters from the fitting are in good agreement with those from Eq. 2.2 and Eq. 2.3 in Table 2.6.

It is worth noting that the CV of an I_{mp} population depends on its average. Since the average is decreasing with time, the assumption of linear changes in the CV accounts for the deceleration of the widening of the population. The evolution of the I_{mp} model with time is depicted in Fig. 2.8.

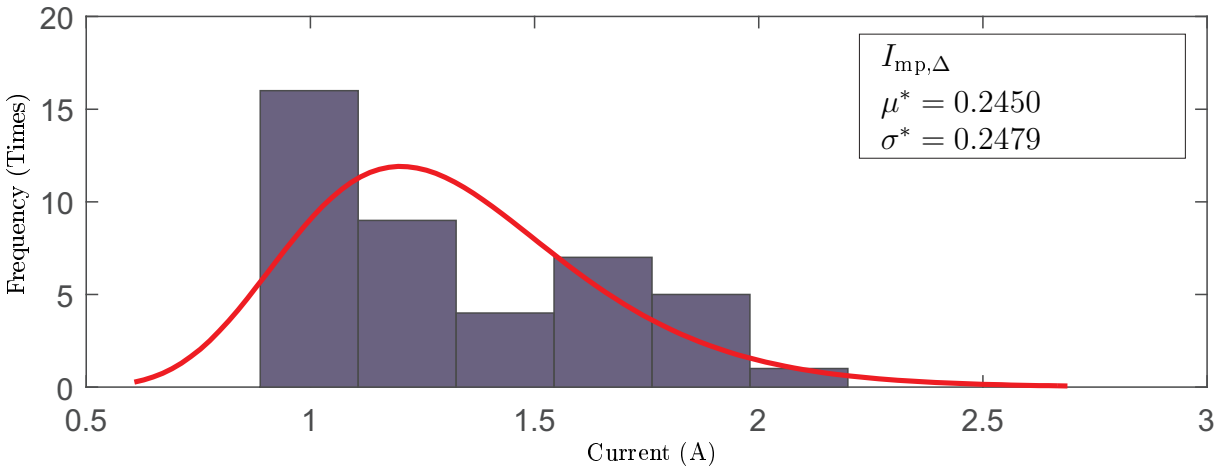

Figure 2.7. Histogram of $I_{mp,\Delta} = 8.68 - I_{mp}$ when the system is 7 years old. Red line: log-normal fitting of the measurements. The μ^*_Δ and σ^*_Δ parameters of the log-normal fitting agree with those in Table 2.6.

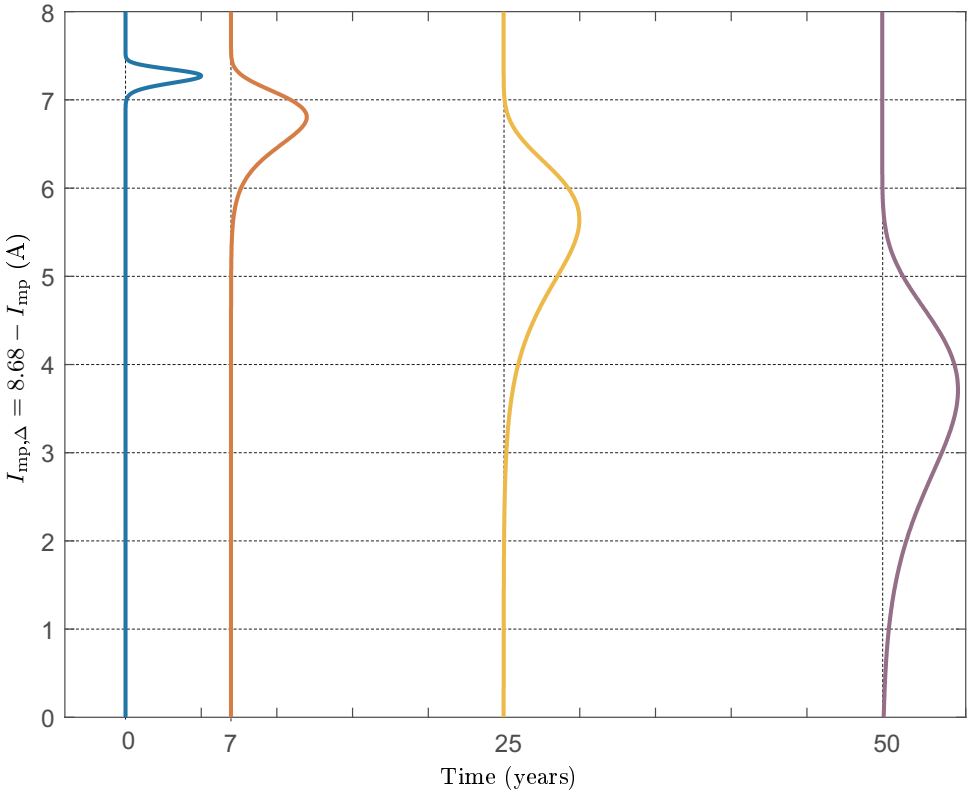

Figure 2.8. Predicted distributions of I_{mp} based on Log-normal model when the system is 1, 7, 25, and 50 years old.

2.4 Prediction of Performance Loss due to Ageing Considering Submodule Level Mismatch

A model has been proposed in the previous section to predict the nature of the population of the maximum power current with field exposure time. It is important to note that it

is impossible to predict the individual degradation rate of each submodule. What can be done instead is predicting the linear increment of CV of the maximum power current and, according to this CV, generating a population of I_{mp}. With this population of I_{mp}, power generation after a number of years can be predicted. The model presented in the previous section is employed in a simulation of 25 years of life of the PV system under test. The objective of the simulation is to predict the effect of the newly measured submodule-level mismatch, with respect to previous module-level results. In order to decouple degradation and mismatch loss, the simulation considers the energy obtained in a conventional series connection of the modules with respect to the maximum available energy if all submodules could operate at their corresponding maximum power points.

Since the simulation depends on the statistical model developed above, a Monte Carlo approach is used, such that 100 populations following the statistical model proposed above are generated. The populations are simulated using the tool described in [47] and the average value of the outputs is taken as the most expected value [4].

Before assessing the effect of experimentally measured submodule mismatch data on the prediction of future power generation, it is worth to discuss how the newly proposed log-normal model overcomes the limitation of generating random populations following the normal model (as used in the past). Following the measurement, the average and standard deviation of year 1 and year 25, as specified in Table 2.6 are used. Since the new submodule level measurements present higher incremental rate of CV of I_{mp} compared to the previous findings, considering a normal population causes problems to generate a realistic population. Figure 2.9 shows how the PDF with normal model causes problems in the generation of a realistic population. It can be seen that the normal model introduces unfeasible cases where for some submodules the current increases with time, which is in practice impossible. This problem had been already detected in [4] (with a lower chance of incidence, due to smaller CV values), where it was solved by generating as many populations as necessary until such a condition was not detected. Figure 2.10 shows one possible result following that approach. However, in Fig. 2.10 it can be seen that even if the currents are decreasing for all cases, this scenario is still unrealistic since some cases present nearly no dependence on time. In consequence, the prediction of power generation in presence of mismatch due to ageing used in the past contained inaccuracies.

The newly described log-normal model does not generate any ambiguous value of

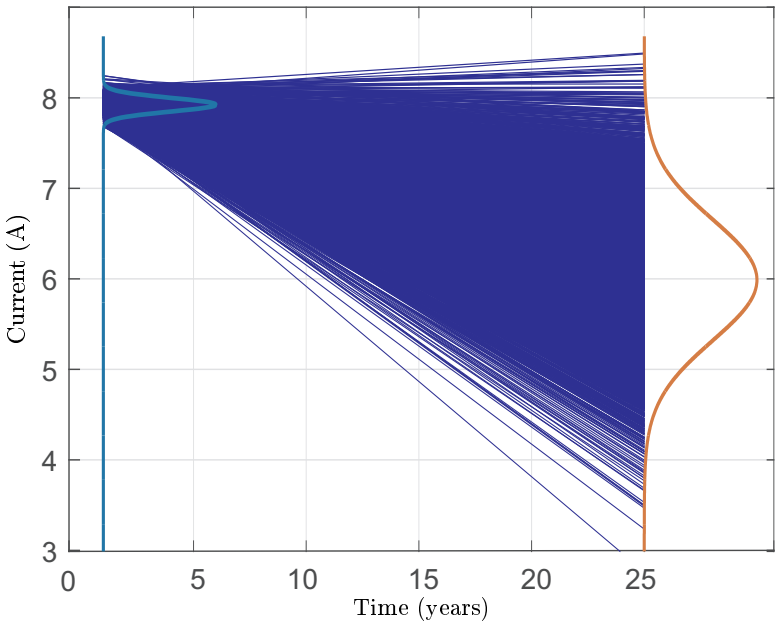

Figure 2.9. Population of I_{mp} with a normal PDF.

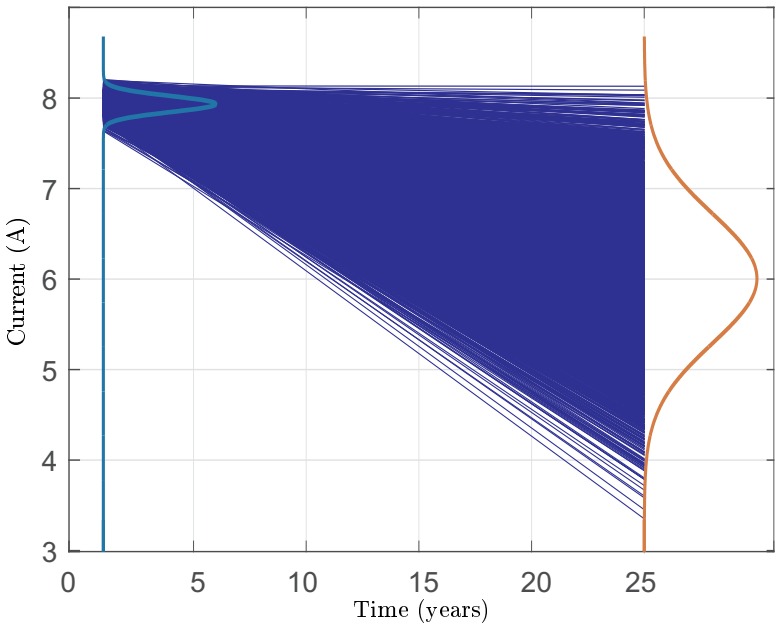

Figure 2.10. Population of I_{mp} with a normal PDF and restrictions.

submodule current with ageing effect and thus it does not require the detection of the unrealistic cases. An example of generated submodule current population with log-normal model is shown in Fig. 2.11.

To justify the use of the proposed model, the effect of both, the conventional normal model and the proposed log-normal model on the efficiency of the system can be compared. Figure 2.12 shows an example case of a 25 years old system where the efficiency with normal model and log-normal model can be observed. It can be seen that, although the

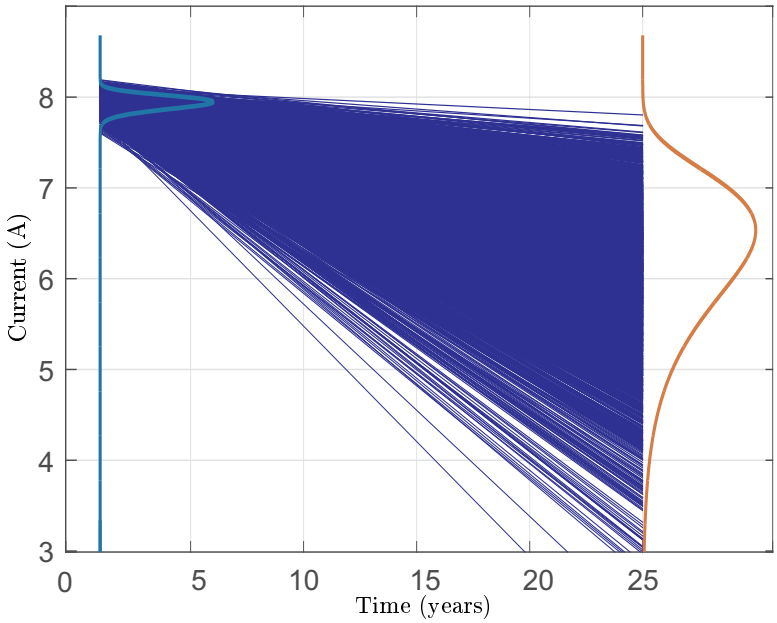

Figure 2.11. Population of I_{mp} with the proposed log-normal PDF.

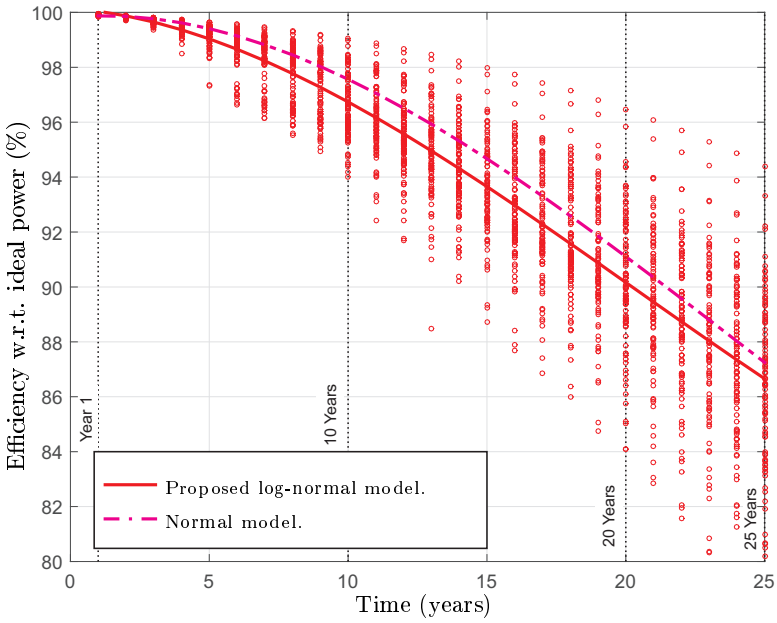

Figure 2.12. Efficiency of the system with respect to the ideal power: using the reported submodule-level measurements and the proposed log-normal model (solid line) and using the submodule-level measurements and a normal model (dash-dotted line).

final value of efficiency is very similar in both cases (around 87%), the shape of the curve with the proposed log-normal model exhibits a larger loss at the early stages of ageing, which results in larger energy yield penalties. In this specific case, the lifetime recoverable loss with the normal model is 4.83%, whereas it increases up to 5.58% with the log-normal approach.

As our interest is to investigate the influence of the newly reported submodule-level

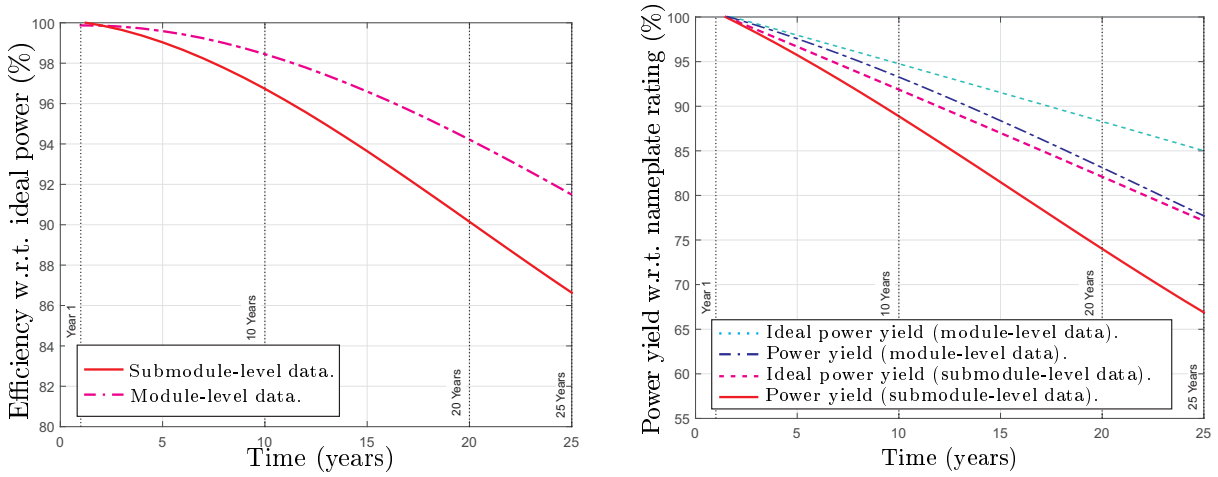

(a) Efficiency and time.

(b) Power yield and time.

Figure 2.13. Comparison between module and submodule-level models. (a) Efficiency of the system with respect to the ideal power with submodule-level measurements (solid line) and using module level measurements from [3] with a normal model (dash-dotted line). (b) Power yield of the system with respect to the nameplate rating if all submodules could operate in their corresponding MPP with module-level data (dotted line) and submodule-level data (dashed line). Power yield of the system with respect to the nameplate rating in a conventional series connection with module-level data (dash-dotted line) and submodule-level data (solid line).

measurement data on system efficiency, a comparison between the models with module-level data from [3] and submodule-level measurement data is done. The system efficiency with respect to the ideal power (if all submodules could operate at their MPP) for both cases is shown in Fig. 2.13(a). In order to maintain the comparison in good agreement with the data in [3], the module-level models consider a degradation of -0.6% and an increase of the CV of +0.36% of the maximum power point current. In the figure, it can be seen that the submodule-level efficiency curve is the same shown in Fig. 2.12 and exhibits a 87% efficiency after 25 years. In contrast, the module-level curve predicts a remarkably higher efficiency of about 91.5%.

Now, the effect of this difference in system efficiency comes from the fact that submodule level mismatch rate is higher than that of module level, and this can be understood by comparing the power yield in both cases. Figure 2.13(b) presents the simulation results of power yield improvement for both cases, the ideal and the actual power (in %) in case of a conventional series connection of the modules, again with the module-level data from [3]. The recoverable loss in that case is 3.17%, in good agreement with the recoverable power predicted for a similar system in [4]. In comparison with module-level data, the submodule-level simulations reveal two main points. The data presented in this research

Table 2.7. Simulation results: efficiency and power Loss.

	Module-Level Data from [4]	Submodule-Level Data
Last Year Efficiency (%)	91.5 %	87 %
Total Lifetime Loss (%)	3.17 %	5.58 %

predicts a 1% yearly degradation, hence the steeper decline of the power yield. More significantly, the predicted recoverable power loss accounts for 5.58%, which represents an increase of 76% with respect to the 3.17% predicted above. A summary of the different predictions can be seen in Table 2.7.

2.5 Comparison with Previously Reported Predictions

In order to evaluate the effect of the novel findings regarding submodule level mismatch, two scenarios, that were reported in [4], are re-investigated and compared. Those two scenarios were referred as: (A) Ageing Mismatch in Utility-scale Systems, and (B) Aging Mismatch in Residential Systems.

2.5.1 Ageing Mismatch in a Utility-scale System

The first scenario considers an existing utility-scale system (8 MW) that consists of strings of 16 modules. Each module includes 3 submodules (20 cells each) in series, with a submodule peak power rated at 81 W. As reported, the module-level data predicted an efficiency loss of about 7% after year 25, which resulted in an overall lifetime loss of 2.74%. The novel submodule-level data show that the recoverable loss in year 25 increases up to 12%, whereas the overall lifetime loss is twice as large as before, nearly 5%. The simulation results for both cases are shown in Fig. 2.14.

2.5.2 Ageing Mismatch in a Residential System

Similarly, Monte Carlo simulation is carried out for a residential system (2.9 kW) consisting of 2 strings of 7 modules rated at 210 W, each module having 3 submodules rated at 70 W peak power each [4]. It can be seen that the module-level data yielded last year (after year 25) and lifetime losses of 8.2% and 3.26% respectively. In contrast, the

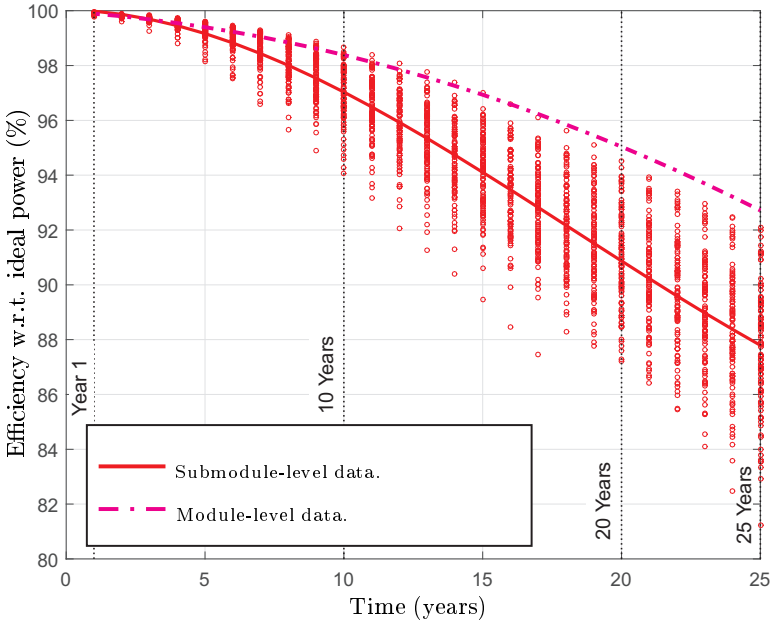

Figure 2.14. Comparison between the results with module-level data in [4] and the results with new submodule-level models: Utility-scale system (Scenario IV in [4]).

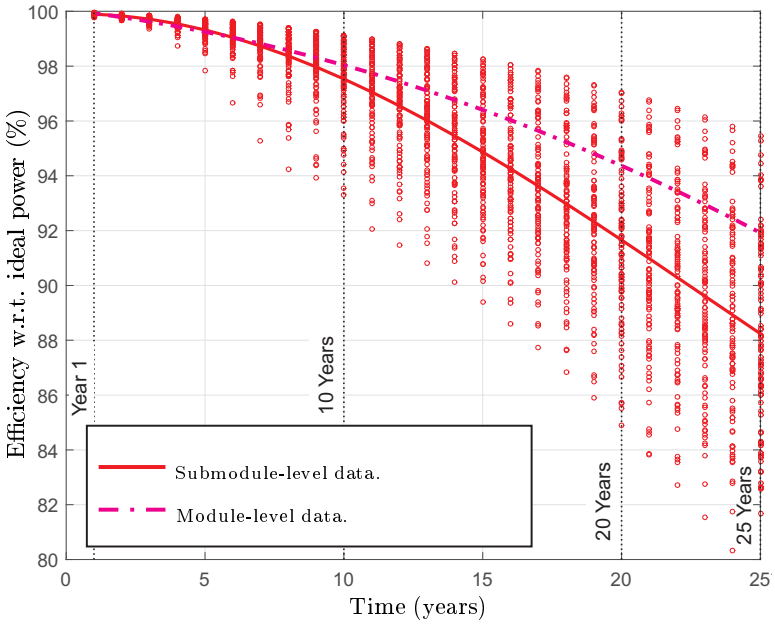

Figure 2.15. Comparison between the results with module-level data in [4] and the results with new submodule-level models: Residential system (Scenario V in [4]).

submodule-level model provides much the same results of the previous case, with a 25 years loss of 12% and a lifetime loss of 4.55%. The efficiency for both cases is shown in Fig. 2.15.

The prior module-level predictions and the novel results can be inspected in Table 2.8. In summary, the novel data predicts that the recoverable loss after 25 years of operation does not depend heavily on the number of PV modules in series and it is close to 5%.

Table 2.8. Life time power loss in representative systems.

	Module-Level Data from [4]	Submodule-Level Data
Recoverable Power Loss Utility-Scale System (%)	2.74 %	4.99 %
Recoverable Power Loss Residential System (%)	3.26 %	4.55 %

This number nearly doubles the previous predictions, with a 75% and 80% increase in each case.

2.6 Impact of Distributed Power Electronics on Lifetime of a PV system

The manufacturer of TSM-230 PC/PA05 provides a warranty of 80% nameplate power production after 25 years, which can be translated to 0.8% linear degradation per year. However, in Fig. 2.13(b), it can be seen that even in case of ideal condition where all submodules operate at their MPP, the power production is slightly less than 80% (approximately 77%). This is simply because we have considered a 1% annual degradation of maximum power, in accordance with the measurements of this chapter (presented in Table 2.5). Considering 0.8% linear degradation per year, a simulation is carried out on the aforementioned PV system to observe the ideal power yield of the system with respect to the nameplate rating. The result is compared with the data sheet and presented in Fig. 2.16. It can be seen that, if all the submodules could operate at their MPP, at the end of year 25, the system can produce 80% of the nameplate power which agrees with the manufacturer warranty.

It is worth to mention that, the warranty for producing 80% of the nameplate power at the end of 25 years is applicable only for individual modules. In the case of series-connected PV modules where the performance of the modules is not only limited by their individual performances, the scenario might be different. Although it has been shown that failures due to dispersion require a high level of localized mismatch [18], in presence of ageing mismatch, a PV system that consists of a number of modules in series is likely to produce less energy than what has been expected and therefore, the lifetime of the PV system is reduced. In this part of the thesis, the effect of using distributed power

(a) Prediction of power generation by the manufacturer.

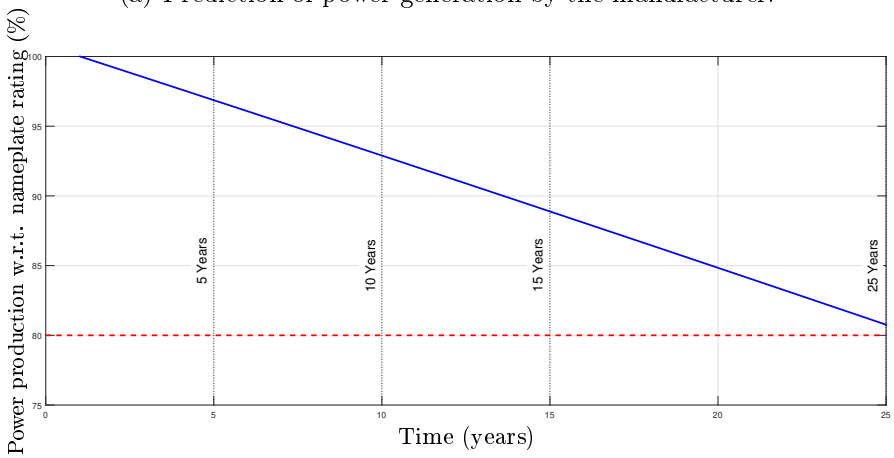

(b) Prediction of power generation with a degradation of P_{mp} of -0.8% per year.

Figure 2.16. Prediction of power production of Trina TSM-230 PC/PA05 modules over 25 years of lifetime.

electronics at submodule level on the lifetime of PV systems is discussed. In order to investigate the impact of using power converters at submodule level on the lifetime of 50 years of a PV system, a simulation is carried out based on the findings of the submodule level measurements. The result is then compared with the power output of the same PV system where conventional bypass diodes are connected in parallel to the submodules.

2.6.1 Lifetime Extension of PV Systems by Means of Ageing Mismatch Mitigation

Typically the lifetime of a PV system is considered to be 25 years. However, this consideration is arbitrary. In this research, and as an example case, the lifetime of a PV system is considered to end where power production falls below 50% of the nameplate rating. Based on that, simulations are carried out considering two cases,

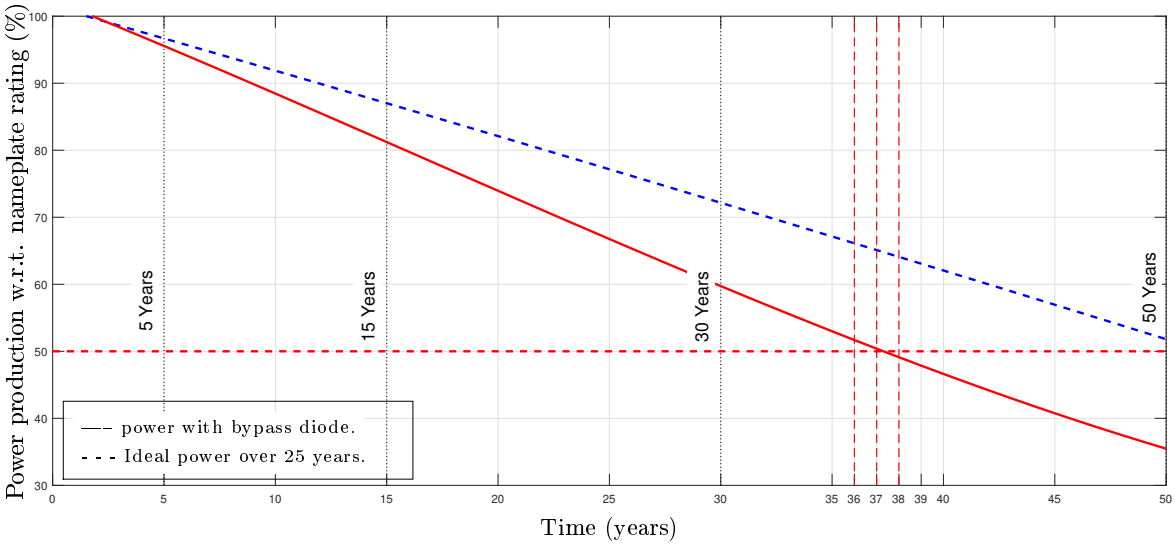

Figure 2.17. Lifespan of a PV system with bypass diode.

(a) **The conventional connection:** only conventional bypass diodes are connected across the submodules in a series connected PV system.

(b) **DPP architecture with PV-IP approach connection:** power converters are connected in parallel with the submodules in a series connected PV system to mitigate ageing mismatch.

The simulations are performed on a PV string of 42 submodules connected in series, using the dispersion presented in Table 2.5.

(a) The conventional connection: In this case, the conventional connection of the PV system is considered where all the submodules are connected in series and bypass diodes are connected in parallel to each submodule. In order to evaluate the performance of the system, the simulation is performed by deploying dispersion and degradation of maximum power current through 50 years of lifetime. The ideal power yield i.e. the power output of the system if all the submodules could operate at their MPP and the actual power yield where each submodule contain a parallel bypass diode, with respect to nameplate rating (shown as 100%) are presented in Fig. 2.17. It can be seen that, from year 38 the PV system with conventional connection is producing less than 50% of the nameplate power while, according to the degradation rate, the system is supposed to provide approximately 65% of the nameplate power. Consequently, at the end of year 50, the system only produces approximately 35% of the nameplate power. Therefore, it can be easily understood that this loss of available power results from the dispersion of I-V

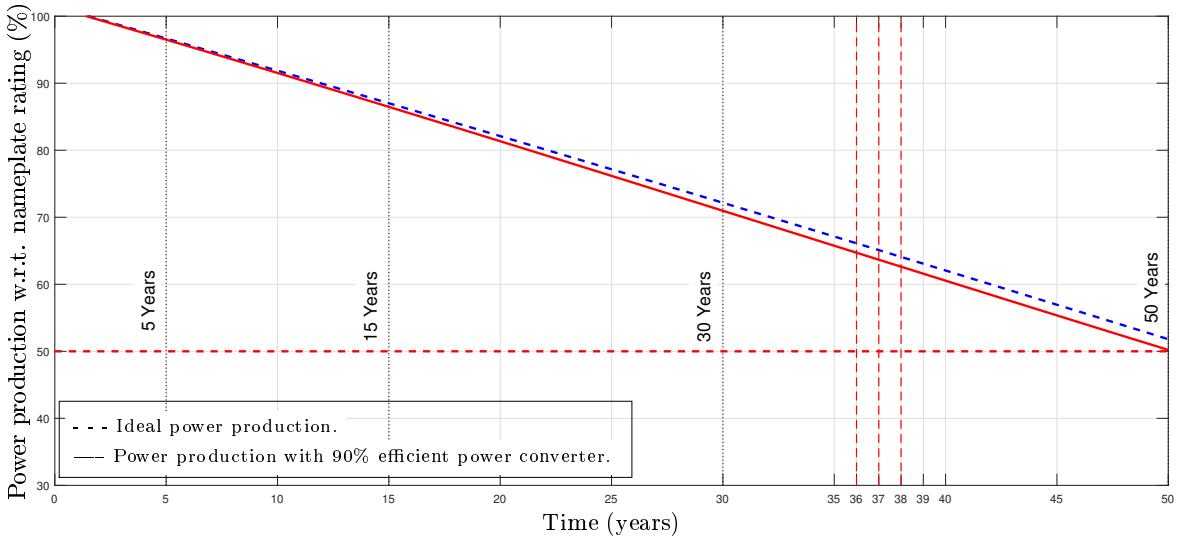

Figure 2.18. Lifespan of a PV system with distributed power electronics

.

parameters of the submodules and conventional series connection can not optimize the system.

(b) **DPP architecture with PV-IP approach connection:** With the same dispersion and degradation rate which has been considered in the previous case, the simulation is performed again and compared with ideal power production. In this case it is considered that 90% efficient power converters are connected in parallel with the submodules following the PV-IP approach of DPP architecture. The results are presented in Fig. 2.18. It can be seen that, all through the lifespan, the power yield by the PV system is very close to the ideal power. Therefore, even at the end of year 50, the system can produce 50% of the nameplate power which is 15% higher than that of the conventional system connection.

2.7 Conclusions

A model of submodule level mismatch based on a 8 years old Poly-Si PV system has been presented in order to have a better estimation of recoverable power loss due to ageing related mismatch. The objective of this model is to predict the CV of I_{mp} of the system after 25 years, which needs to be validated in the future by taking further measurements. A comparison has been done with previous literature where module level data have been considered for submodule level. It has been demonstrated that the CV of I_{mp} at sub-

module level is larger than I_{sc} what has been reported before on the basis of module level measurement. Due to the fact of having higher incremental rate of CV of maximum power current at submodule level, the loss estimation of a PV system, based on module level data and I_{sc} is inappropriate. In other words, it can be said that the proposed model shows that the recoverable energy loss due to ageing might have been underestimated in the past. In absence of partial shading or any other source of mismatch, the recoverable loss during 25 years of operation of a PV system is between 4 and 6%. These quantities may offer an opportunity for submodule-level power electronics converters to mitigate mismatch and provide nearly 100% recovery of the energy loss [48]. It is important to note that the characterization of ageing effect on submodule level has been done with relatively low number of samples and only two years of measurements have been considered, however, the consistence of the degradation and dispersion rates of I-V parameters of the submodules validates the approach. In addition to that, the findings regarding the degradation rate of maximum power from the submodule level measurements are also in accordance with the previously reported data.

The effect of distributed power electronics on the lifetime of PV systems has also been evaluated. It has been shown that deploying power converters at submodule level not only increases the lifetime power production, but also prolongs the lifetime of the PV system. Considering that the end of life of a PV system could be established at 50% of the nameplate power, a system with distributed power electronics could reach a lifetime of 50 years, whereas a conventional PV system would have a lifetime of only 38 years. In the next chapter, the impact of distributed power electronics as well as topologies that can be used in case of ageing related mismatch will be discussed in detail.

UNIVERSITAT ROVIRA I VIRGILI
DISTRIBUTED POWER ELECTRONICS FOR EXTENDED EFFICIENCY AND LIFETIME OF UTILITY-SCALE PHOTOVOLTAIC SYSTEMS
MD Nazmul Hasan

Chapter 3

Design and Implementation of an Isolated DC-DC Converter for Mitigation of Ageing Mismatch

In this chapter, a power converter that is well suited to mitigate the ageing mismatch is proposed. It is worth to mention that DPP architectures with different types of power converters have been proposed in the past. However, they were focused on mitigation of partial shading effects, and none of them considered submodule level mismatch data. In this chapter, we discuss possible candidates that can deal with the specific characteristics of submodule level mismatch. Finally, the realization of the converter is verified with experimental results.

3.1 Introduction

A comparison of the performance of various DPP architectures in case of partial shading has been presented in [49]. In that paper, it has been shown that the PV-bus architecture with exact MPPT control provides the highest efficiency improvement (18.1%). However, the architecture is not fully suitable for inverter interaction due to the generation of non-convex power-current curve. In contrast, the PV-IP architecture has provided an efficiency improvement of 17.4%, which is close to the performance with the PV-bus architecture, and consistently exhibits a convex power curve which is beneficial for the inverter interaction. Finally, it has been shown that the PV-PV architecture provides the

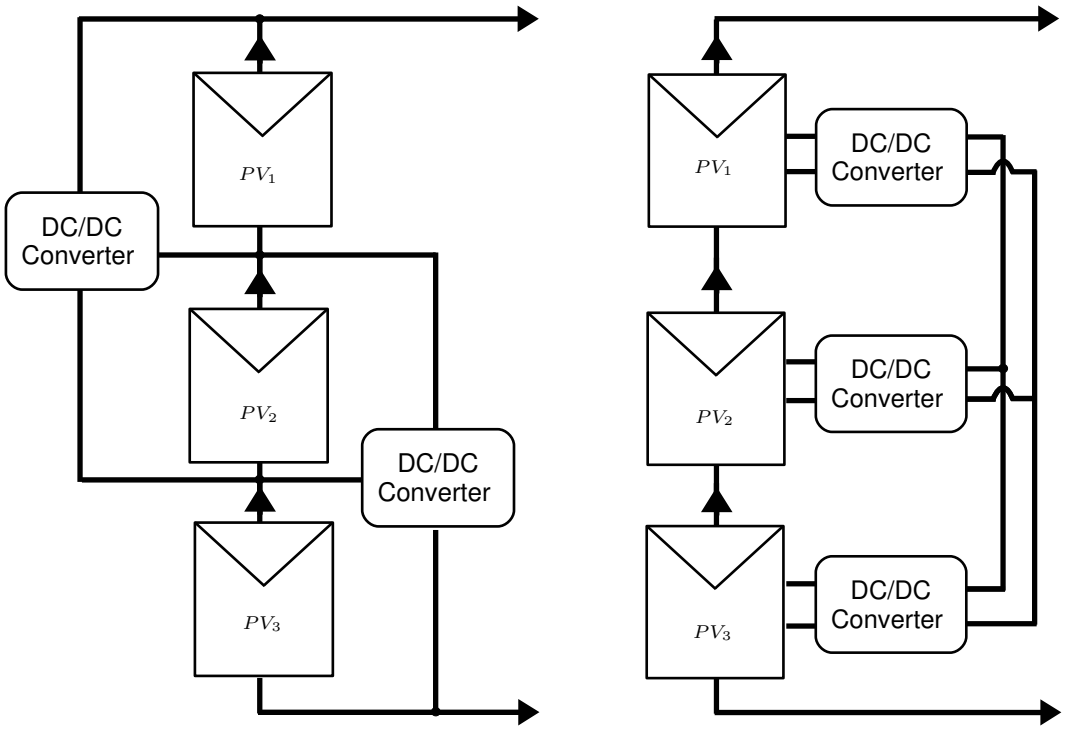

(a) PV-PV DPP architecture. (b) PV-IP DPP architecture.

Figure 3.1. Types of DPP architecture.

lowest efficiency improvement of 10.5% in case of uneven lighting condition. However, it is important to note that in [49], all DPP converters have been considered to be 33% of the PV power rating. The power rating requirement of the converter for every individual architecture has not been discussed in [49]. Therefore, it is worth investigating which architecture requires the optimum power rating of the converters since their cost and size are directly proportional to the power rating and have significant impact on LCOE. A general comparison regarding this issue has also been shown in [18] but no specific submodule level dispersion has been considered.

In order to investigate how the DPP converters of different architectures process ageing mismatch power over 25 years, simulations are done based on the findings of the previous chapter. The simulations are performed on 42 submodules of 14 modules, connected in series. Since the fundamental power processing techniques of the PV-bus and the PV-IP architectures are similar, the simulations are done for the PV-IP architecture and the PV-PV architecture only. For completeness, those two architectures are redrawn in Fig. 3.1. In case of ageing of 25 years, following the data presented in Table 2.5, the simulation results are presented by means of histogram in Fig. 3.2. The histogram shows how much percentage of the total power processed during the time of life, the converters operated

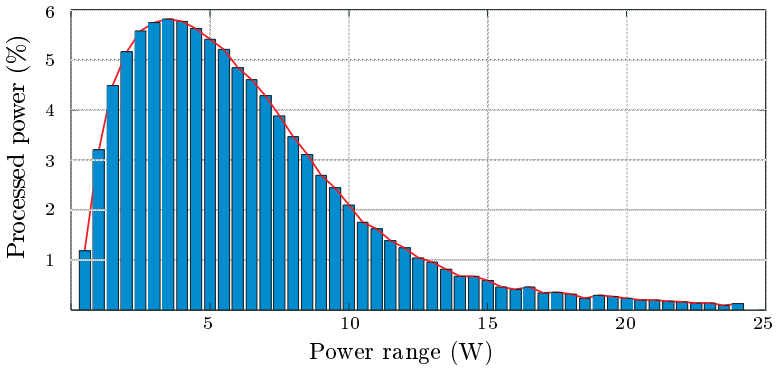

(a) PV-IP architecture.

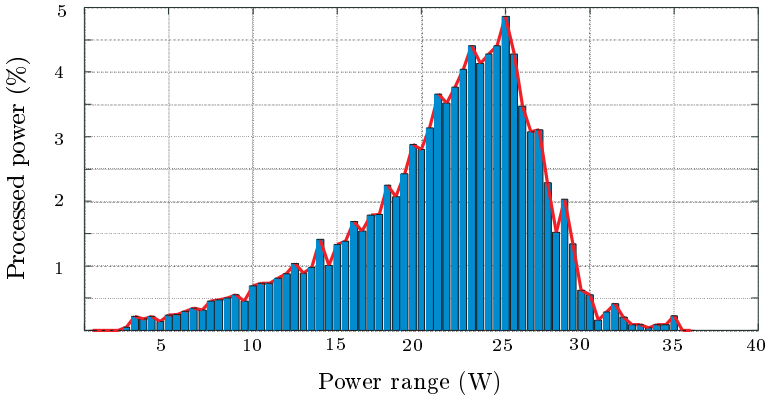

(b) PV-PV architecture.

Figure 3.2. Histrogram of processed power by the converters after 25 years.

at any particular power. The histogram provides a clear classification of which operating points are more relevant in each case. A summary of the findings can be described as follows,

(i) PV-IP architecture:

- With a power converter rated at 15 W, 95.34% of the total power would be processed.
- With a power converter rated at 10 W, 84.5355% of the total power would be processed.

(ii) PV-PV architecture:

- With a power converter rated at 30 W, 98.2927% of the total power would be processed.
- With a power converter rated at 20 W, 35.7833% of the total power would be processed.

Table 3.1. Specifications of the converter.

Parameters	Range	Nominal Value
Input voltage	$\in$ [5, 15] V	10 V
Output voltage	$\in$ [5, 15] V	10 V
Power output	$\in$ [0.5, 15] W	10 W

It can be seen that in case of the PV-IP architecture, converters rated at 15 W can process more than 95% of mismatch power over 25 years. In contrast, the PV-PV architecture requires converters with a power rating of 30 W in order to process the same amount of mismatch power. In addition to that, in the case of PV-IP, most of the processed power falls within the range of 2 W to 5 W. On the contrary, the range in the case of PV-PV converters is 20 W to 28 W. The discussion suggests that the PV-IP architecture with converters rated at 15 W and showing their peak efficiency in the range of 2 W to 5 W can mitigate the ageing mismatch at the submodule level with a high level of success.

3.2 Specifications of the Converter

Based on the analysis of the previous section, the specifications of the converters can be considered. From the histogram of percentile power processed by different architectures for mitigation of ageing mismatch over 25 years, it is justified that if PV-IP architecture is selected, the overall power rating of the converter can be reduced, which will certainly be more cost effective. Given that the converters will operate mostly around the V_{mp} of the submodule, an input voltage rating of the converter is selected. The specifications of the converters are presented in Table 3.1.

3.3 Topology Selection

As justified above, the low power efficiency of the converter is a relevant parameter. In order to balance currents in PV-IP architectures, as explained in Chapter 1, DC-DC converters require properties of bidirectional power transfer, 1:1 turn ratio and isolation between the input and the output. Some candidates with characteristics of bidirectional power transfer, isolation and unity gain are listed below.

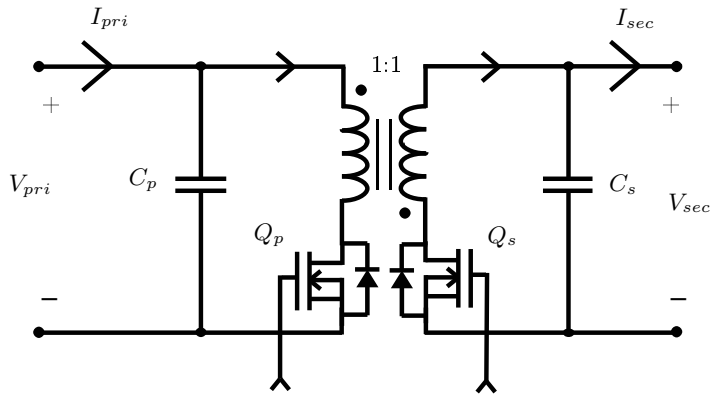

Figure 3.3. Bidirectional Flyback converter.

Flyback Converter: In the past, the requirements for isolated bidirectional power transfer have been satisfied with simple architectures such as the flyback converter (shown in Fig.3.3) [31] which can be operated in discontinuous conduction mode (DCM) and with closed-loop regulation of the voltages. Although the flyback converter presents poor transformer utilization, it is well-suited for the application, given that transformer use increases with the power level, resulting in conversion efficiency around 90% for loads above 2 W [48]. The approach has been demonstrated to be effective in PV plants affected by partial shading increasing the energy yield of the system by more than 5% [4]. Nonetheless, these converters are not very effective where the mismatch among the submodules are relatively low, for instance, in cases where the converter has to process power below 2 W. Although, the flyback converter has the advantages of low part count and simplicity in control, the isolation transformer exhibits leakage inductance which produces losses. An extra snubber circuitry can minimize the effects of the leakage inductance, but switches with high voltage rating are required. In addition to that, low transformer utilization increases the overall size and cost of the converter. Input and output ripple currents also affect the low power efficiency adversely.

SEPIC Converter: A bidirectional symmetric non-isolated SEPIC converter has been proposed in [50]. If an isolation transformer is introduced, as shown in Fig. 3.4, this converter can also meet the required specifications. Unlike the buck-boost converter, the input current of a SEPIC converter is continuous. However, like in a buck-boost converter, the output current of the SEPIC converter is pulsating. The energy transfer of a SEPIC converter requires a large capacitor with large current capacity. Furthermore, in case of an isolated SEPIC converter, the leakage inductance exhibited by the transformer causes

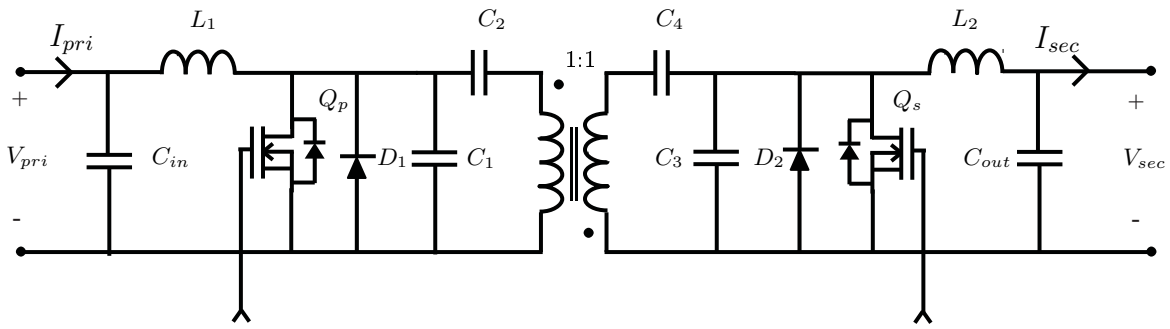

Figure 3.4. Bidirectional SEPIC converter.

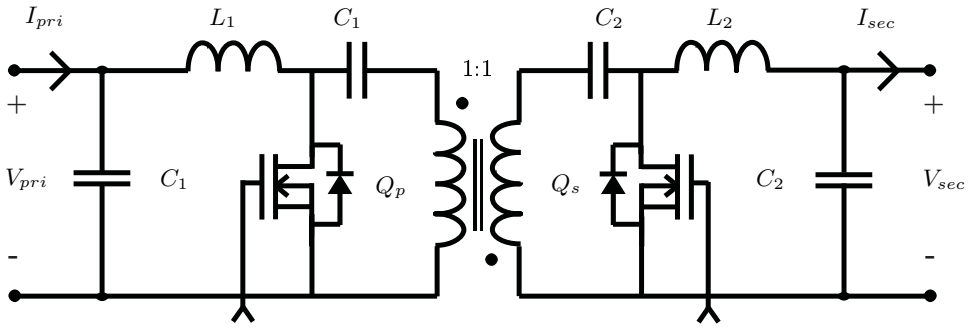

Figure 3.5. Bidirectional Ćuk converter.

losses at low power.

The Ćuk Converter: The Ćuk converter can also be considered as a possible candidate in this context. It has relatively low part count. However, the Ćuk converter suffers from several drawbacks. For instance, like the SEPIC converter, the isolated Ćuk converter requires large capacitors with large current carrying capacity. Moreover, the leakage inductance exhibited by the isolation transformer and the hard switching nature of the Ćuk converter affect the low power efficiency adversely. An isolated bidirectional Ćuk converter is shown in Fig. 3.5.

Resonant Converter: As an alternative to the switched-mode power converters, a resonant converter can also be considered. Given that resonant converters can be operated in Zero Voltage Switching (ZVS) or Zero Current Switching (ZCS) mode, their low-power efficiency can overcome the disadvantages of having large number of switches. Two basic structures of resonant converters are the series resonant converter (SRC) and the parallel resonant converter (PRC). The SRC, shown in Fig. 3.6, features some advantages like low switching loss and low EMI while operating at ZVS. However, it is difficult to optimize the SRC for a wide range of input voltages and load variations. In addition, voltage regulation at very light loads is not possible with the SRC [51, 52].

The parallel resonant converter, shown in Fig. 3.7, overcomes the limitation of the

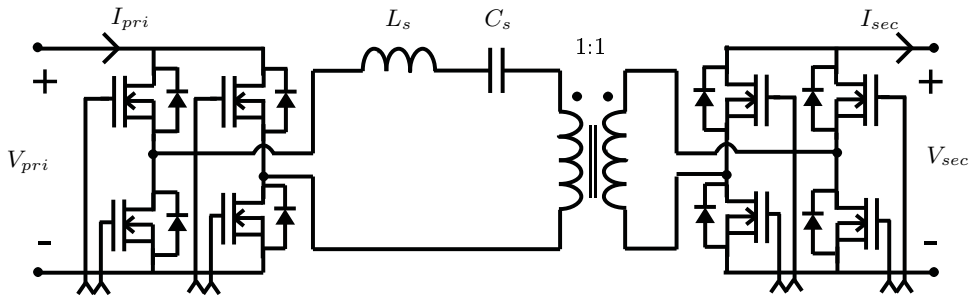

Figure 3.6. Bidirectional series resonant converter.

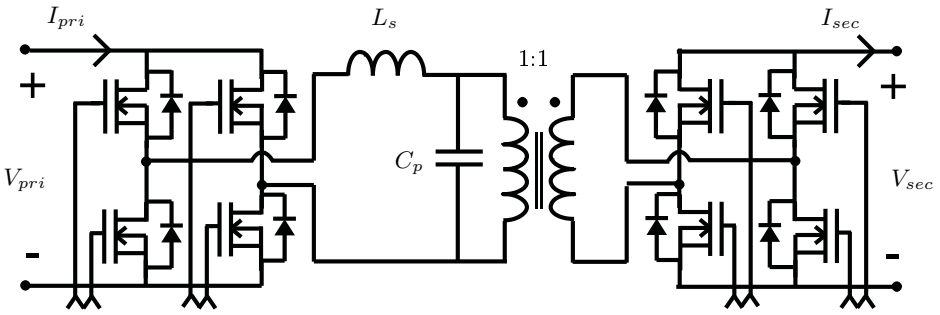

Figure 3.7. Parallel resonant converter.

SRC with regulated output voltage at no load and continuous output current. However, since the primary current barely depends on the load condition, a significant amount of circulating current may flow through the resonant tank at light load or even at no load condition. Again, larger circulating current with higher voltages also limits the range of the input voltage [51, 52]. In addition to that, due to the circuit nature, PRC is not actually a bidirectional converter.

Apart from the SRC and the PRC, there are other types of resonant converters which are actually combinations of the SRC and PRC. The series parallel resonant converter (SPRC) can regulate the output voltage at very light load conditions. Wide load variation can be possible with slight change in switching frequency. Moreover, at light-load, the circulating current through the resonant tank is smaller than that of the PRC [53]. Typically there are two types of SPRC named as LLC resonant converter (shown in Fig. 3.8) and LCC resonant converter (shown in Fig. 3.9).

Considering all the merits and demerits, in this research, a comparison of the performance of the Ćuk and an LLC resonant converter is described in Appendix A. A simulation showing the efficiency for both cases (considering conduction, gate charge and switching losses) is deployed in the Appendix. In addition, the simulation also considers losses due to leakage inductance in case of the Ćuk converter. The efficiency comparison

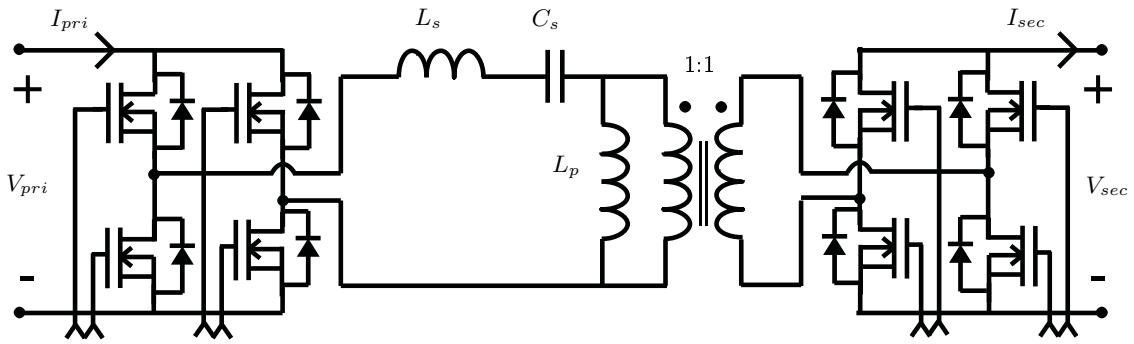

Figure 3.8. LLC resonant converter.

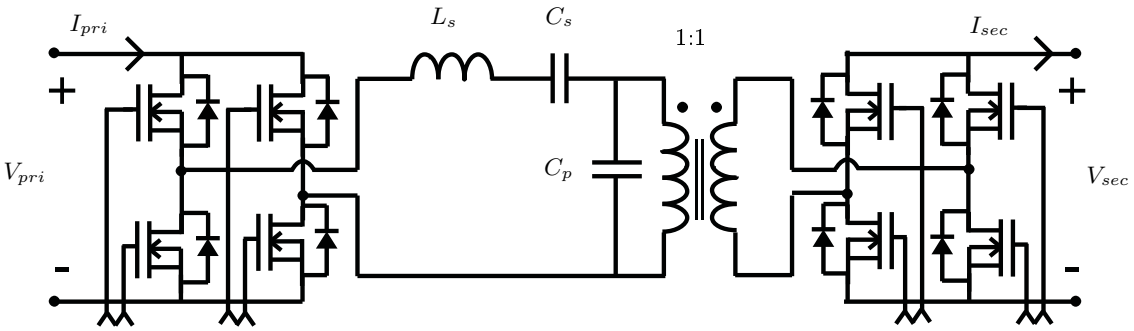

Figure 3.9. LCC resonant converter.

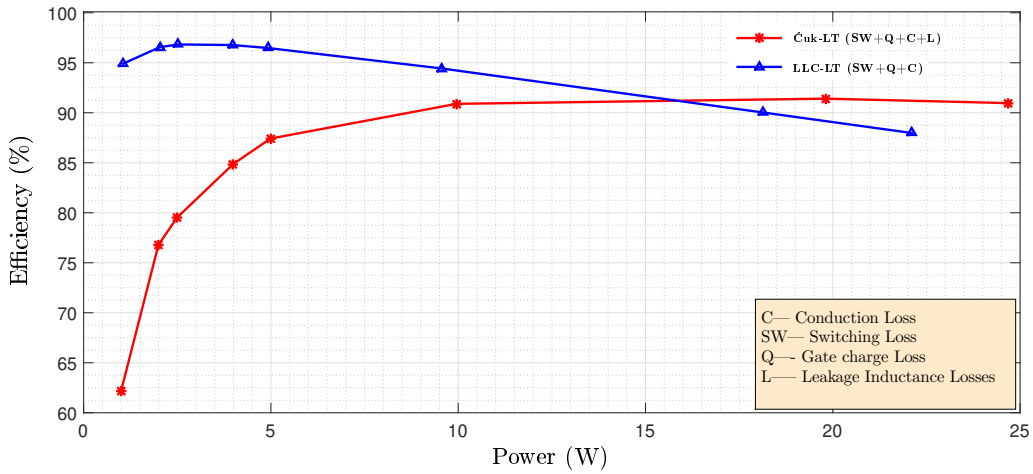

Figure 3.10. Efficiency comparison of the Ćuk and the resonant converter.

in the range of 1 W to 25 W is presented in Fig. 3.10.

It can be seen in Fig. 3.10 that, up until 15 W, the LLC resonant converter provides a very good efficiency of more than 90%. In contrast, the efficiency of the Ćuk converter up until 10 W is well below 90%. Additionally, the peak efficiency of the LLC resonant converter falls in the range of 2 to 5 W. Since our interest is to design a converter which can provide good efficiency at the range of 1 W to 15 W and with peak efficiency at the

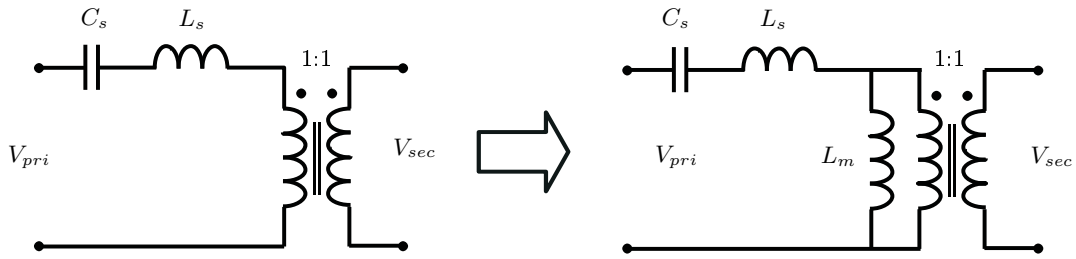

(a) SR converter with ideal transformer. (b) SR converter transformed into LLC converter.

Figure 3.11. Realization of an isolated series resonant converter.

range of 2 W to 5 W, in this research, the resonant converter is considered as a possible candidate. Nonetheless, it is yet to be seen how the LLC topology can be modified to allow fully symmetric bidirectional power transfer. In this chapter, a resonant converter is developed that is appropriate for the specific application of submodule level ageing mismatch mitigation.

3.4 Design of a Resonant Converter

A topology that features resonant conversion with isolation and bidirectional power transfer is proposed in this section. In addition, the design of the converter is described with the aim to keep the switching loss within a limit so that it does not affect the low power efficiency. A possible approach to control the bidirectional power transfer operation of the converter is also presented.

3.4.1 Fundamentals of Resonant Conversion

For the application we are interested in, a series resonant converter can be used, since it has unity gain for all loads at resonant frequency. However, for achieving unity gain, the SRC has to be operated at resonant frequency and therefore, ZVS operation can not be achieved. Additionally as isolation between input and output is required, a transformer has to be introduced. The effect of this transformer is that a magnetizing inductance of the transformer appears in parallel with the load, and hence the converter is in fact an LLC converter. Figure 3.11 shows how in presence of isolation transformer, the SRC becomes an LLC converter. In fact, one important advantage of the LLC topology is that no extra inductance is required. The leakage inductance of the transformer can be used as the resonant inductance of the converter.

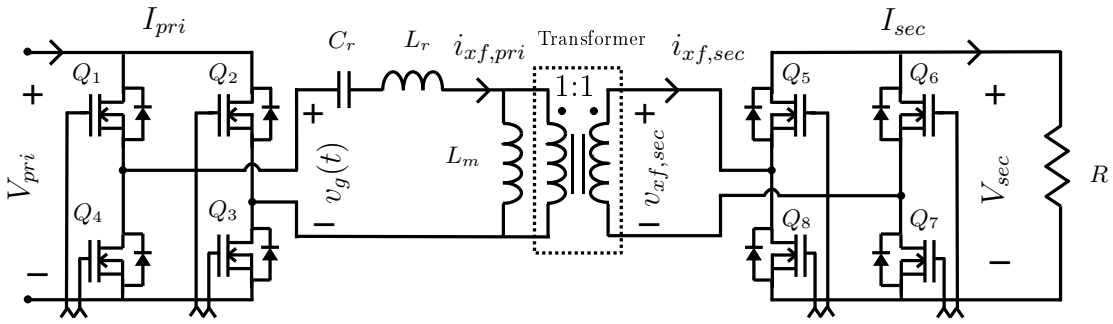

Figure 3.12. Conventional isolated bidirectional LLC converter.

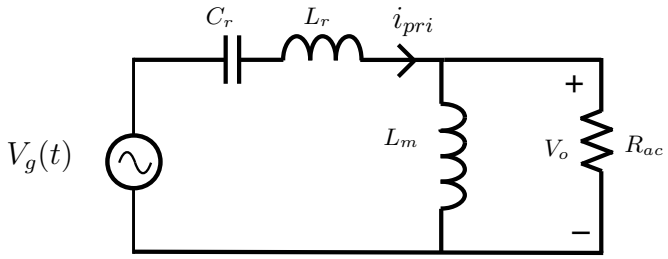

Figure 3.13. Equivalent circuit of a conventional isolated LLC converter.

3.4.2 LLC Converter

A conventional isolated LLC converter is shown in Fig. 3.12. If the switch network is controlled to produce a square wave of frequency $f = \omega/2\pi$ Hz, then the output voltage waveform $v_g(t)$ of the switch network can be expressed as a Fourier series [54],

$$v_g(t) = \frac{4V_g}{\pi} \sum_{n=1,3,5..}^{\infty} \sin \omega t \tag{3.1}$$

The fundamental component of the output voltage is,

$$v_{g1}(t) = \frac{4V_g}{\pi} \sin \omega t \tag{3.2}$$

One of the useful and simple approaches to analyze the gain characteristics of a resonant converter in the frequency domain is the First Harmonic Approximation (FHA), where it is assumed that the power transfer from input through resonant tank is associated only with the fundamental components of the voltage and current of the converter. The FHA ac equivalent circuit of Fig. 3.12 is shown in Fig. 3.13, where $R_{ac} = \frac{8}{\pi^2}R$ is the effective value of a resistive load R. The equivalent impedance Z_{eq}, the current through

the inductor I_{Lr}, and the output voltage V_o can be found by the following equations,

$$Z_{eq}(s) = sL_r + \frac{1}{sC_r} + \frac{sL_m R_{ac}}{sL_m + R_{ac}} \tag{3.3}$$

$$I_{Lr}(s) = \frac{v_{g1}}{Z_{eq}(s)} \tag{3.4}$$

$$V_o(s) = \frac{I_{Lr}(s) sL_m R_{ac}}{sL_m + R_{ac}} \tag{3.5}$$

As described in [55], the gain of the converter is as follows

$$K(Q, m, F_x) = \frac{F_x^2(m-1)}{\sqrt{(mF_x^2 - 1)^2 + F_x^2(F_x^2 - 1)^2(m-1)^2 Q^2}} \tag{3.6}$$

where Q is the quality factor,

$$Q = \frac{\sqrt{L_r/C_r}}{R_{ac}} \tag{3.7}$$

R_{ac} is the reflected load resistance of R due to rectifier

$$R_{ac} = \frac{8N_p^2}{\pi^2 N_s^2}.R \tag{3.8}$$

N_p and N_s are the number of primary and secondary turns of the transformer respectively and in this case, $N_p = N_s$

F_x is the normalized switching frequency,

$$F_x = \frac{f_{sw}}{f_r} \tag{3.9}$$

f_{sw} is the switching frequency,

f_r is the resonant frequency,

$$f_r = \frac{1}{2\pi\sqrt{L_r C_r}} \tag{3.10}$$

and m is the ratio of total primary inductance to resonant inductance,

$$m = \frac{L_r + L_m}{L_r} \tag{3.11}$$

The frequency vs. voltage gain characteristics of the LLC converter for a set of loads (corresponding to a set of Q) and m=6 is shown in Fig. 3.14. It can be observed that unit conversion gain for all loads can be achieved by switching the converter at a constant

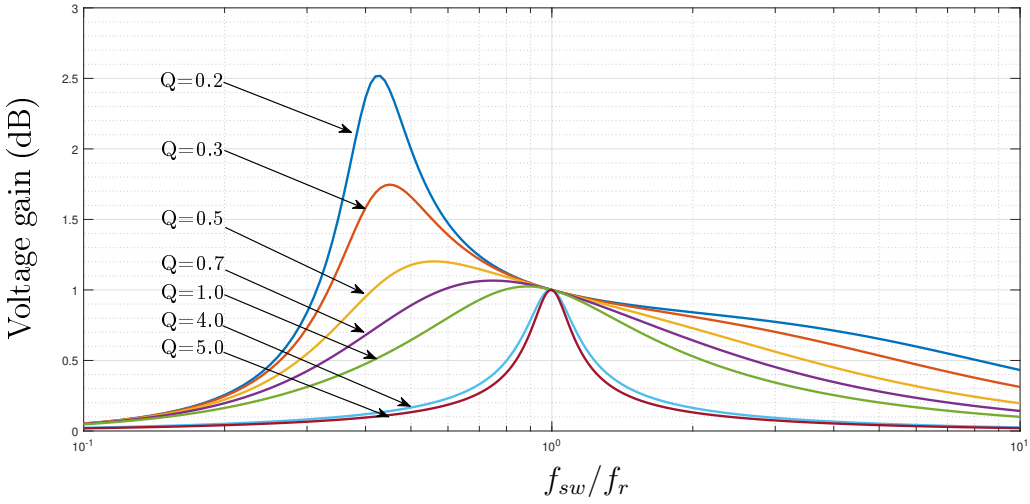

Figure 3.14. Frequency response of the LLC converter for a set of loads with $m = 6$.

frequency of $f_{sw}/f_r = 1$. In order to operate the converter such that unity gain can be achieved for a range of loads, the elements of the resonant tank can be calculated for a fixed switching frequency by evaluating Eq. 3.6 - Eq. 3.11.

For a more accurate design, the capacitor output voltage ripple noted as Δv, can also be considered. The output voltage ripple of a LLC converter can be calculated as follows,

$$\Delta v = \frac{T I_{Lr,max}}{8\pi C} \tag{3.12}$$

where C is the output capacitor and T is the switching period.

For instance, if the converter is switched at 150 kHz and 100 µF capacitor is used at the output, for the heaviest load of 15 W, the output voltage ripple of the LLC converter will be

$$\Delta v = \frac{1.5\sqrt{2}}{150 \times 10^3 \times 8\pi \times C} = 5.6 \text{ mV}$$

It is worth mentioning that the part count of a bidirectional LLC converter is comparatively high as shown in Table 3.2. This may increase the LCOE which will be discussed in Chapter 4 of this thesis. However, as shown in Table 3.3, low stress and conduction loss allow us to select very low power components for this converter.

3.4.3 Modified LLC Converter

The conventional LLC converter shown in Fig. 3.12 does not exhibit the same input/output characteristics in both power transfer directions. In order to obtain fully symmetrical

Table 3.2. List of the components required for the LLC converter.

Parameter	LLC
Inductor	2
Transformer	1
Switch	8
Capacitor	2

Table 3.3. Losses and stress level of the LLC converter.

Parameter	LLC
Transistor current, I_{on}	I_{in}
Transistor voltage, V_{OFF}	V_g
Primary copper loss, I_p^2R	I_{Lr}^2R
Secondary copper loss, I_s^2R	I_{Lr}^2R

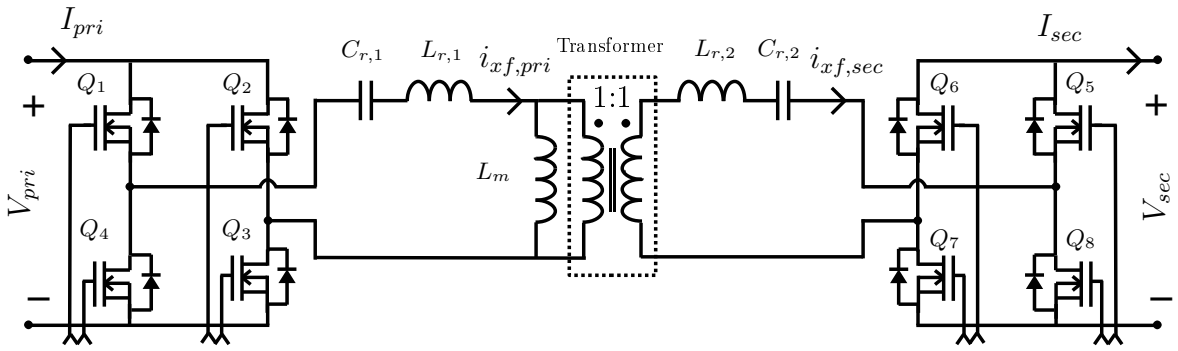

Figure 3.15. Proposed bidirectional LLC converter.

and bidirectional power transfer, an additional resonant tank in the secondary side of the transformer is proposed in this thesis. The resulting symmetrical tank can be seen in Fig. 3.15. This type of modified tank has been proposed in the past [56, 57]. However, in those works the converter was used for comparatively high power applications and in a different context. A detail of the resonant tank is shown in Fig. 3.16.

A comparison of the frequency response between the conventional LLC converter and the proposed modified LLC converter with the same quality factor and resonant-magnetizing inductance ratio is shown in Fig. 3.17 (top most curves presents the lowest Q). It can be seen that the frequency response of the proposed bidirectional LLC converter is slightly different from the conventional LLC converter. However, the gain character-

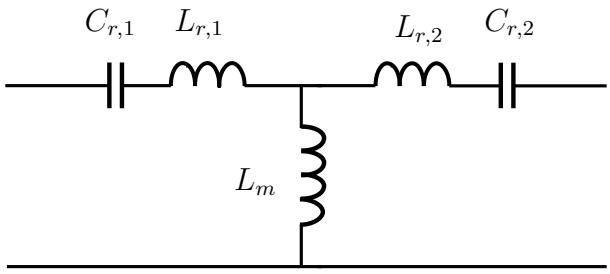

Figure 3.16. Resonant tank of the modified LLC converter.

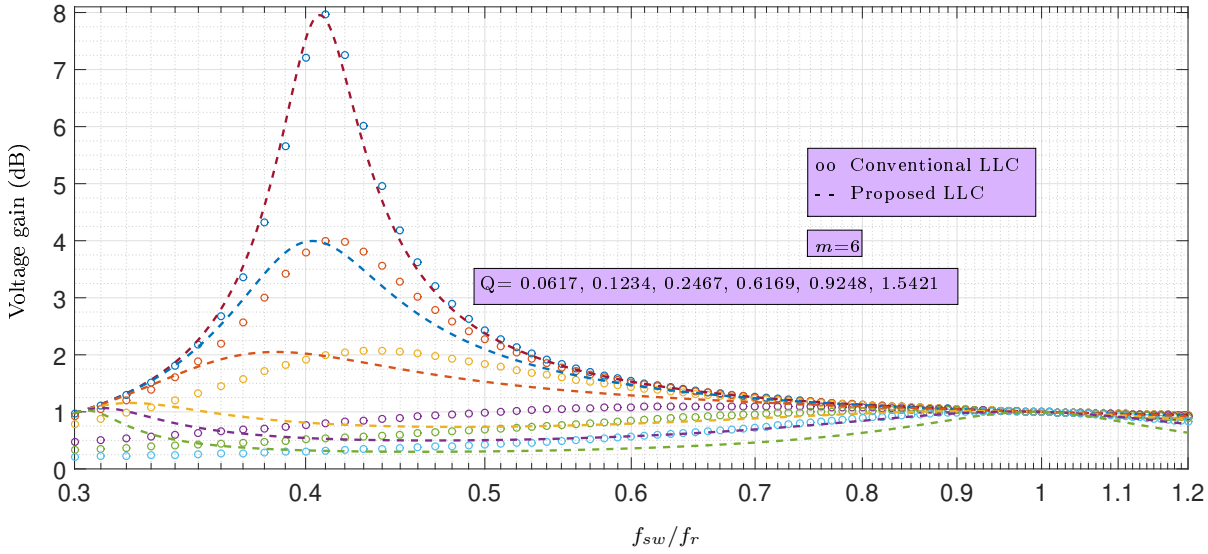

Figure 3.17. Frequency response of the conventional LLC converter and the proposed LLC converter.

istics of both converters have similarities around the resonant frequency. Our interest is to design the proposed converter based on switching it below but near the resonant frequency. Considering that, the new LLC converter will be designed by following the conventional LLC converter design approach [55].

3.4.4 Operation of the Converter

The LLC converter can be operated in three modes described below, considering a 1:1 turn ratio of the isolation transformer.

- ◇ Switching frequency f_{sw} lower than f_r
- ◇ Switching frequency f_{sw} equal to f_r
- ◇ Switching frequency f_{sw} higher than f_r

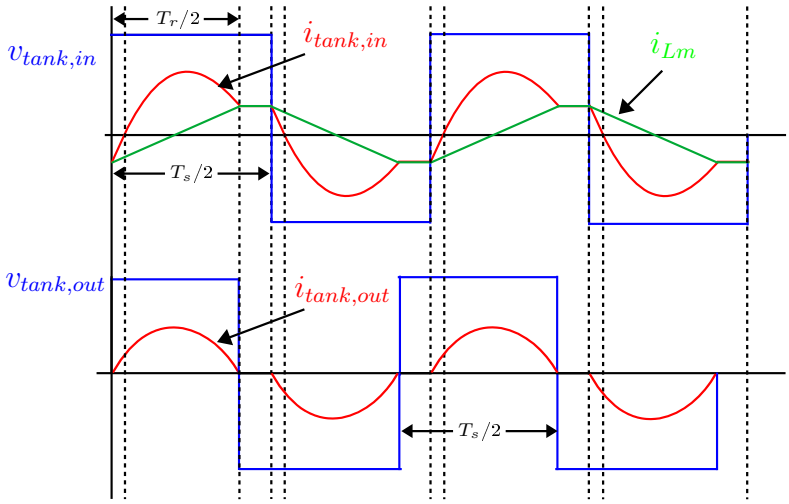

Figure 3.18. Typical waveforms of the LLC converter at switching frequency lower than the resonant frequency.

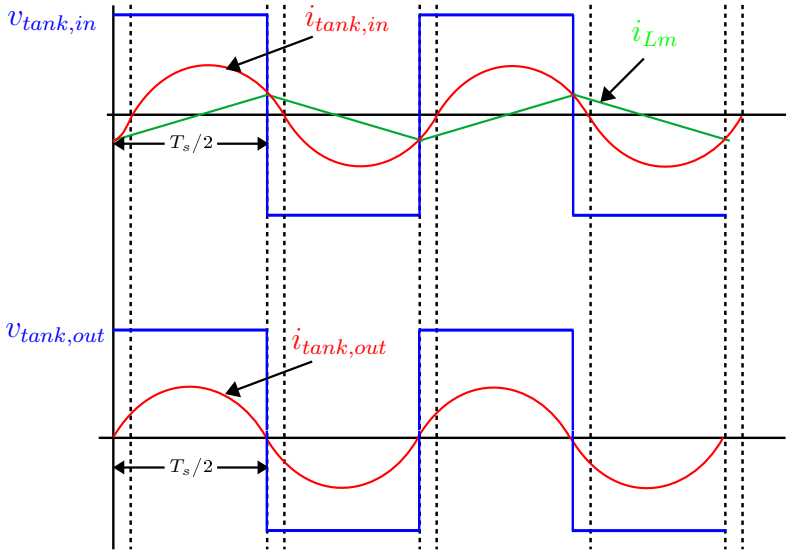

Figure 3.19. Typical waveforms of the LLC converter at switching frequency equal to the resonant frequency.

Switching frequency below resonant frequency: The resonant inductor current, I_{Lr} reaches the magnetizing current before the end of the first switching half cycle and, both the resonant inductor and magnetizing inductor feed the secondary rectifier with higher voltage than the input voltage. This results in a boost operation of the converter. The typical waveforms of voltage and current of this mode are shown in Fig. 3.18.

Switching frequency equal to the resonant frequency: In this mode, as shown in Fig. 3.19, at the end of the first switching half cycle, the resonant inductor current reaches the magnetizing current and the secondary rectifier current reaches zero by the end of the half cycle. Hence, the output voltage will always be equal to the input voltage.

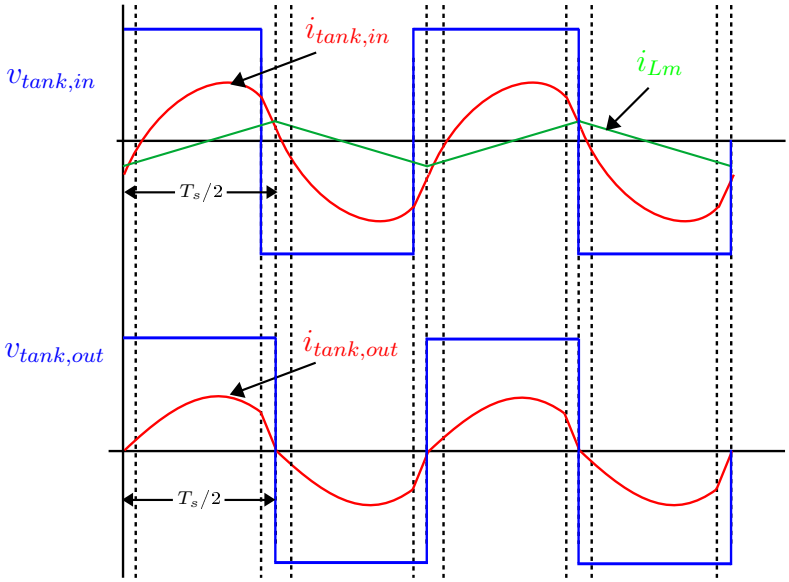

Figure 3.20. Typical waveforms of the LLC converter at switching frequency higher than the resonant frequency.

The full power delivery operation is done in this mode.

Switching frequency above the resonant frequency: Buck operation is done in this mode. Each half cycle delivers part of input power to the output. The resonant inductor does not have enough time to reach the magnetizing current and is interrupted by the other half cycle. Therefore, the converter operates at higher input voltage than the output. The typical waveforms of voltage and current of this mode are shown in Fig. 3.20.

3.4.5 Design of the Converter

The FHA model of the proposed bidirectional LLC converter with 1:1 turn ratio is shown in Fig. 3.21. In order to get symmetrically bidirectional power transfer, the resonant elements of both sides of the tank must be equal. Hence,

$$L_{r,1} = L_{r,2} = L_r \tag{3.13}$$

$$C_{r,1} = C_{r,2} = C_r \tag{3.14}$$

Now, the input impedance of the proposed converter can be written as follows,

$$Z_{in,LLC,sym} = \frac{1}{sC_r} + sL_r + \frac{1}{\frac{1}{sL_m} + \frac{1}{\frac{1}{sC_r}+sL_r+R_{ac}}} \tag{3.15}$$

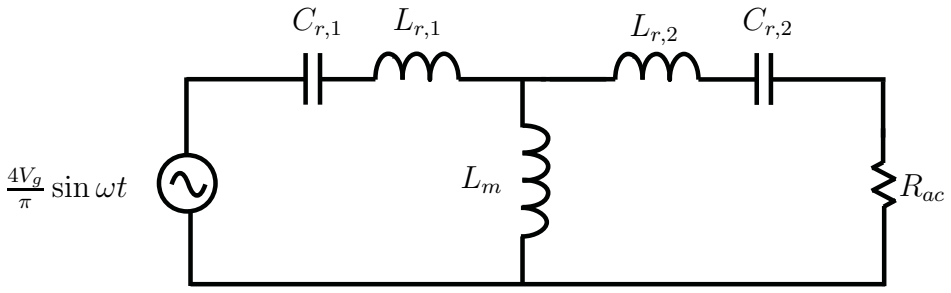

Figure 3.21. FHA model of the bidirectional LLC converter.

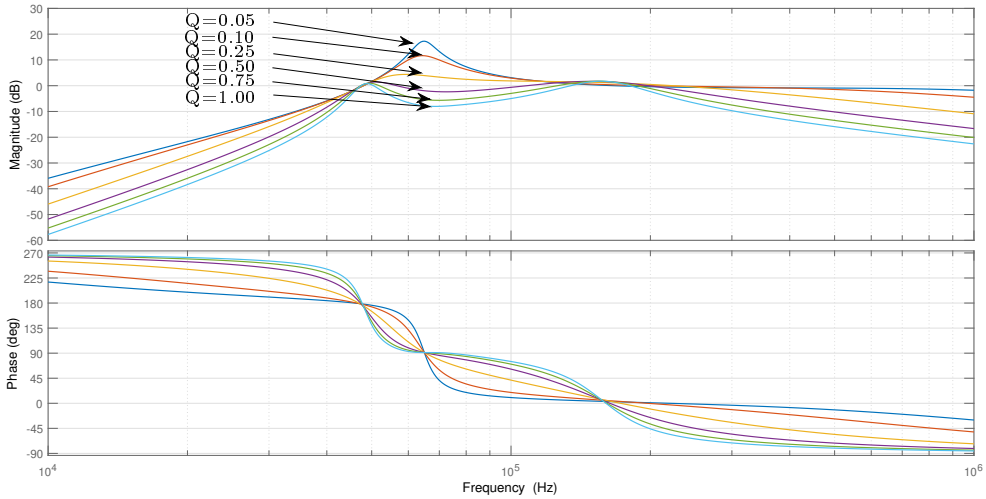

Figure 3.22. Frequency response of the proposed LLC converter for a set of load with m= 6.

The forward transfer function of the converter can be expressed by the following equation

$$H_{LLC,sym} = \frac{sL_m}{sL_m + (\frac{1}{sC_r} + sL_r + R_{ac})\frac{R_{ac}}{Z_{in,LLC,sym}}} \tag{3.16}$$

The frequency vs. voltage gain and phase of the proposed LLC converter for a set of loads (corresponding to a set of Q) and m=6 is shown in Fig 3.22. It can be observed that unit conversion gain for a range of loads can be achieved by switching the converter at the resonant frequency, $f_{sw}/f_r = 1$.

In this research, we propose an alternative mode of operation below the resonant frequency. Variable conversion gain can be achieved by selecting the switching frequency such that the gain is always above *unity* for a range of loads. For example, considering the frequency response shown in Fig. 3.22, we could switch the converter at a frequency such that the gain is higher than *unity* for the loads of interest. Above those loads, the converter exhibits gain lower than 0 dB, which naturally limits the power transfer capacity

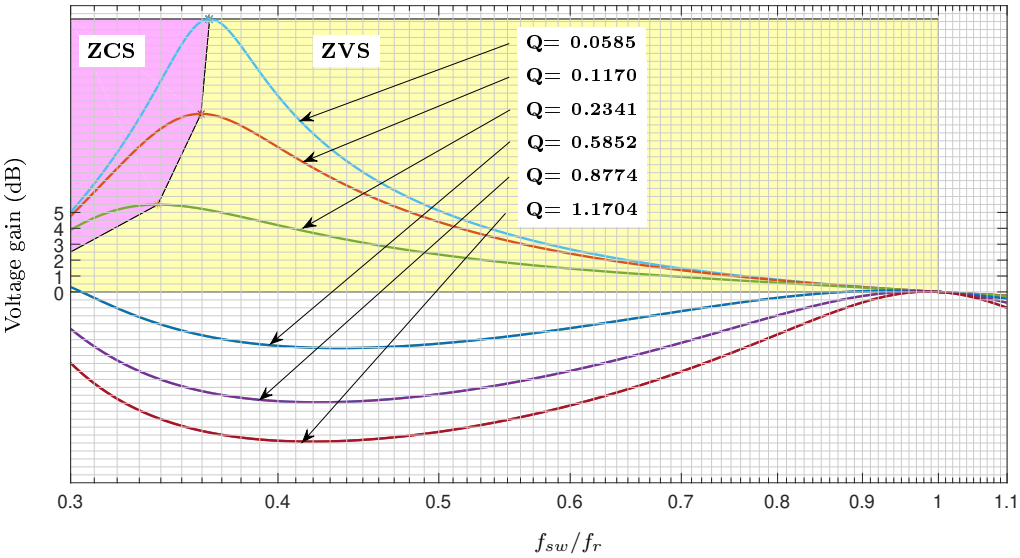

Figure 3.23. Selecting Q.

of the converter. Since operating below the resonant frequency will modify the constant gain operation of the converters, voltage balancing can be achieved by turning ON and OFF the converter, as in a burst mode operation. Operating the converter in this mode presents several advantages such as (a) the operating point of the converter will always be in inductive zone, and thus ZVS can be achieved resulting in high efficiency at very low power, (b) the converter presents an inherent power limit so that it will never transfer power over that range.

If the nominal value of the input-output voltage and maximum power of the converter, presented in Table 3.1 are considered, due to the full bridge rectifier at the output side, the equivalent *ac* resistance for a maximum load of 15 W, will be

$$R_{ac} = \frac{8R}{\pi^2} = 5.40\Omega \tag{3.17}$$

Considering this maximum *ac* equivalent resistance, the design steps of the converter are presented as follows.

Step 1 : selecting the maximum value of Q

In order to get an average output voltage equal to the input voltage, the gain of the converter has to be more or close to the *unity* with a transformer of 1:1 turn ratio. However, in case of burst mode operation, the gain of the converter has to be more than *unity*. Considering this, the quality factor Q of the proposed LLC converter must be selected. The relation between the quality factor and load resistance is shown in Eq 3.7. The equation implies that with the increase in load current, Q increases. The frequency

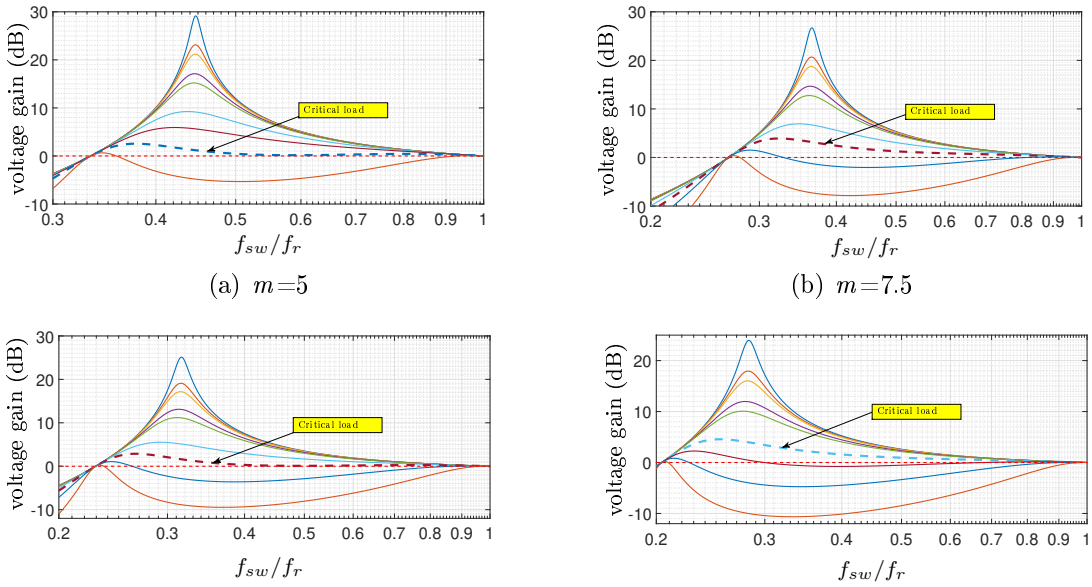

(a) m=5 (b) m=7.5

(c) m=10 (d) m=12.5

Figure 3.24. Effect of variation of m on voltage gain.

response of the proposed LLC converter for a set of Q with constant resonant-magnetizing inductance ratio is shown in Fig. 3.23. It can be seen that for Q=0.8774, the converter gain is still close to *unity* (0 dB) for the heaviest load, at a frequency where ZVS can be achieved for lighter loads. In contrast, for Q=1.1704, the converter gain is less than *unity* for the heaviest load. Hence, maximum value of Q can be selected to approximately 0.8774. In this thesis Q= 0.85 is selected.

Step 2: Selecting m

As mentioned earlier, m is the ratio of magnetizing inductance (L_m) to resonant inductance (L_r). Figure 3.24 shows the effect of variation of m on the gain characteristics of the converter while the quality factor remains same for all the cases. It can easily be understood that for the same Q, lower values of m provide higher gain and narrow range of frequency modulation, which increases the flexibility in control and voltage regulation for a wide range of input-output voltages. However, lower values of magnetizing inductance increase circulating current and hence conduction loss. On the contrary, higher values of m reduce the circulating current and thus higher efficiency can be achieved. In Fig. 3.24, the highest loads (critical load) are also shown for different m at which the operation can be done, i.e. more than *unity* gain can be possible for a wide range of switching frequency.

From the discussion above, it can be understood that there is a tradeoff between efficiency and flexibility in control for selecting the m. However, for the power rating we

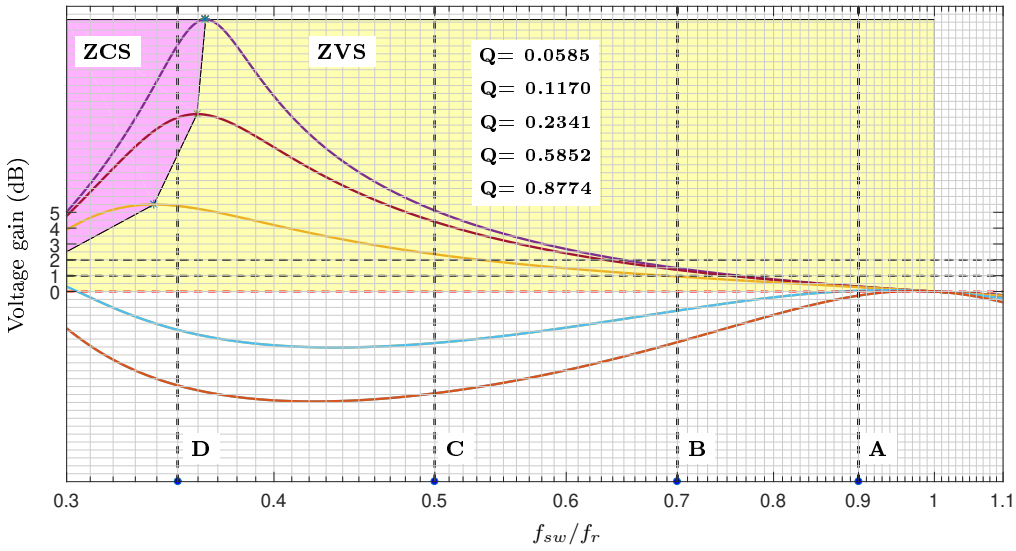

Figure 3.25. Selecting switching frequency.

are interested in, any value of m between 5 to 12.5 can be considered as appropriate. In this thesis, $m = 7.5$ is selected.

Step 3: Selecting the switching frequency

The plots of Fig. 3.23 are reproduced in Fig. 3.25 with maximum value of Q=0.85 and m=7.5 in order to select the switching frequency. The variation of voltage gain is shown with respect to the ratio of switching frequency to resonant frequency. For choosing the switching frequency this ratio has to be selected in such a way that it meets the following requirements for all load we are interested in: (a) the voltage gain of the converter has to be more or close to *unity* (b) the operating points of the converter have to be in inductive region in order to achieve ZVS, at least for the light loads.

Figure 3.25 shows three possible points noted as A, B, and C where ZVS can be achieved for light loads of our interest. However, only point A can meet both requirements mentioned above. For the case of operating the converter at point B and C, although ZVS can be achieved for light loads, the voltage gain does not meet our requirement for the heavier loads. In case of point D, neither ZVS nor required voltage gain can be achieved for the loads of our interested. Hence, if the converter can be operated at point A, at light loads ZVS can be achieved and voltage gain will be either more than *unity* or close to the unity for the range of loads of our interest.

The switching frequency of the converter can be selected considering that even if higher switching frequency can reduce the size of the resonant component, the penalties

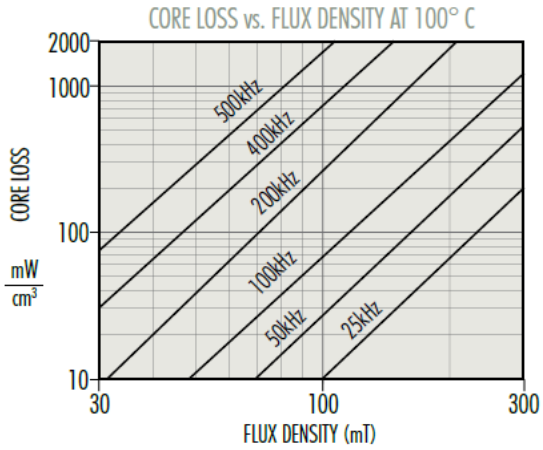

Figure 3.26. The effect of switching frequency on core loss (from [5]).

are higher switching loss, gate charge loss and core loss. Although, higher switching frequency may also improve the performance of low pass filter from critical noise-sensitive frequency bands, increase in core loss is a tradeoff. As an example, core loss dependence of ferrite material on switching frequency is shown in Fig. 3.26. It can be seen that the core loss can be minimized by reducing the switching frequency to 25 kHz or even less. However, in that case, the increase in cost and size of the resonant element may disinterest the designers.

Considering all the aspects discussed above, we have decided to select the switching frequency between 100 kHz and 200 kHz. For instance, switching frequency of 150 kHz is selected in this thesis and hence the resonant frequency of the converter can be calculated by considering the operating point of the converter at point A in Fig. 3.25, where $f_{sw}/f_r = 0.9$. Therefore,

$$\begin{aligned} f_r &= f_{sw}/0.9 \\ &\approx 165 \text{ kHz} \end{aligned} \tag{3.18}$$

Table 3.4. Parameters of LLC converter.

Parameter	Value
Resonant Capacitor, C_r	0.21 µH
Resonant Inductor, L_r	4.43 µH
Magnetizing Inductor, L_m	28.8 µH

Step 4: Calculating Resonant Component

The results from the previous three steps are summarized as follows,

$$R_{ac} = 5.40\ \Omega$$
$$Q = 0.85$$
$$m = 7.5$$
$$f_{sw} = 150\ \text{kHz}$$
$$f_r = 165\ \text{kHz}$$

From Eq. 3.7,

$$Q = 0.85 = \frac{\sqrt{L_r/C_r}}{5.40} \tag{3.19}$$
$$f_r = 165\ \text{kHz} = \frac{1}{2\pi\sqrt{L_r C_r}} \tag{3.20}$$

By solving Eq. 3.18 to Eq. 3.20, the parameters of the resonant tank can be found for power rating of maximum 15 W. The parameters of the proposed LLC resonant converter are listed in Table 3.4.

3.4.6 Control Scheme

A very simple control approach for the symmetric LLC converter is proposed in this section. When the primary voltage is sufficiently higher than the secondary voltage, the power is transferred from primary to secondary. Similarly, if the primary voltage is lower than the secondary by a certain limit, the power is transferred in the opposite direction. In order to do that, one of the full-bridges is activated at the switching frequency, while the other full-bridge acts as a non-active rectifier. To improve the low power efficiency of

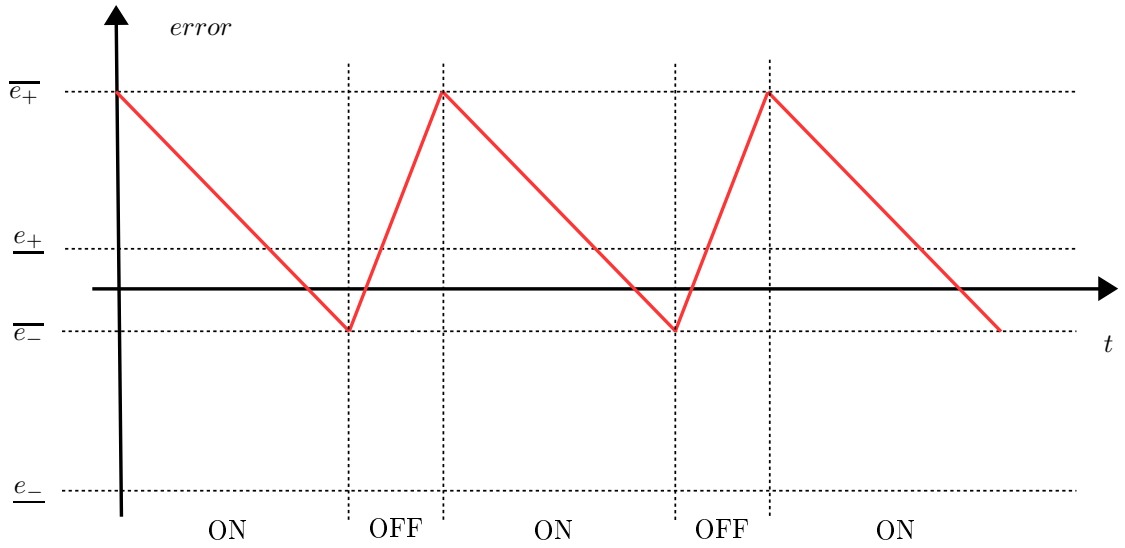

(a) Example of error trajectory in case of power transfer from primary to secondary.

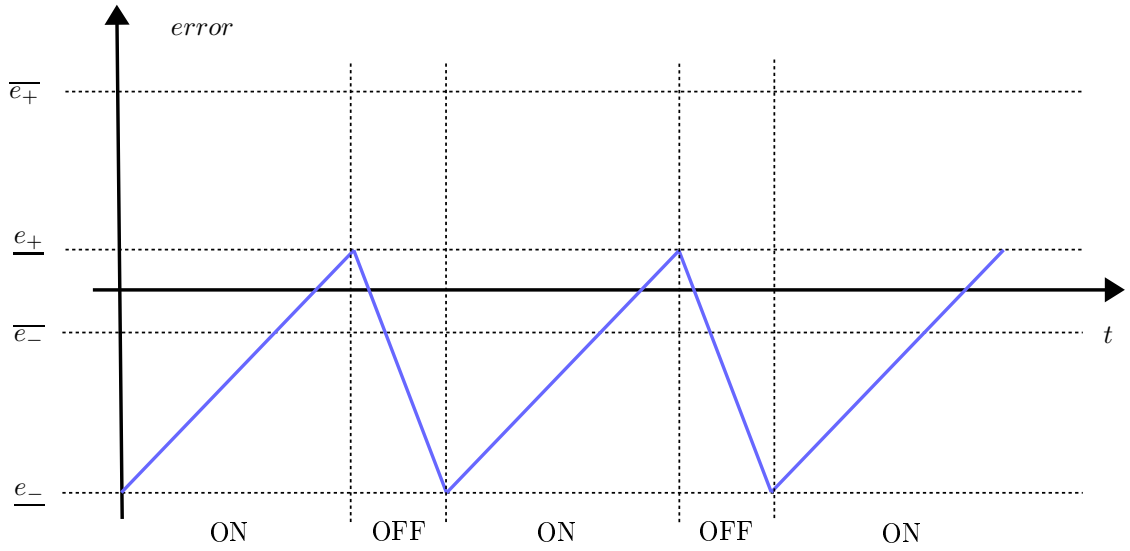

(b) Example of error trajectory in case of power transfer from secondary to primary.

Figure 3.27. Double-band hysteresis control limits error and allows burst-mode operation.

the converter, Schottky diode can be used in parallel with each switch. If the converter is switched at the resonant frequency, the input-output gain is approximately one, and only enabling the appropriate full-bridge, the converter balances voltages in the primary and secondary ports. However, the switching frequency is selected below the resonant frequency such that the output voltage will be higher than the input voltage, specially for light loads. In this context, regulation is carried out by enabling a burst-mode or, in other words, by turning ON and OFF the corresponding switching network. This is achieved by realizing a double-band hysteresis comparator that turns ON and OFF the appropriate

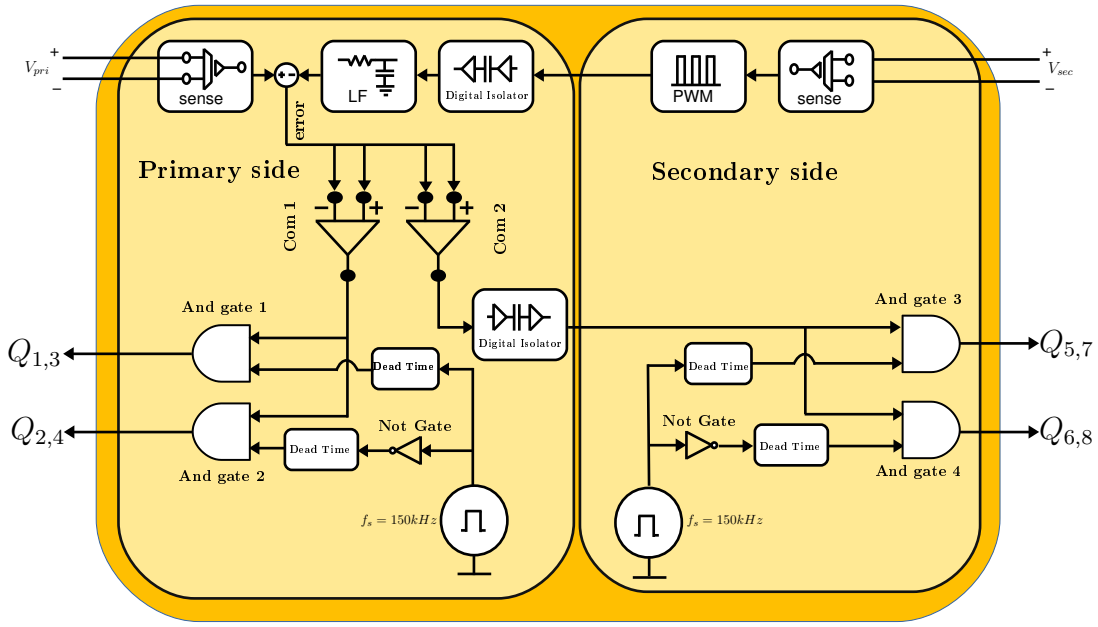

Figure 3.28. Block diagram of the proposed controller.

full-bridge, depending on the error voltage between the primary and secondary ports. Considering $error = v_{pri} - v_{sec}$, Fig. 3.27 shows the double-band hysteresis regions and two example trajectories of the error. It can be observed that, if the error is positive and reaches $\overline{e_+}$, the primary-side full-bridge is switched at the frequency f_{sw}. In case of a light load, the voltage of the secondary side will rise above the primary voltage and the error will become negative and reaches $\overline{e_-}$ point at which the primary-side full-bridge is disabled. The opposite case of a large negative error equal to $\underline{e_-}$ activates the secondary side full-bridge, which is deactivated when the error becomes positive and equal to $\underline{e_+}$.

The proposed controller is realized according to the block diagram shown in Fig. 3.28. It can be seen that voltage sensors are used to generate the error between the primary and the secondary voltages. The secondary voltage is isolated by a digital isolator. The error is compared with the required thresholds $\overline{e_+}$, $\underline{e_+}$, $\overline{e_-}$ and $\underline{e_-}$, and generates two enabling signals for the primary and secondary full-bridges. The enable signals are used in simple AND gates together with an oscillator whose output is a constant frequency square wave signal and goes through a dead time generator circuit.

In order to validate the performance of the proposed controller, an LTSpice simulation of the proposed converter along with the controller is carried out in steady-state condition considering that the power is transferred from primary to secondary. The primary and secondary voltage waveforms of the simulation are shown in Fig. 3.29. It can be seen that the secondary voltage is rising to a certain value defined by the controller and then the

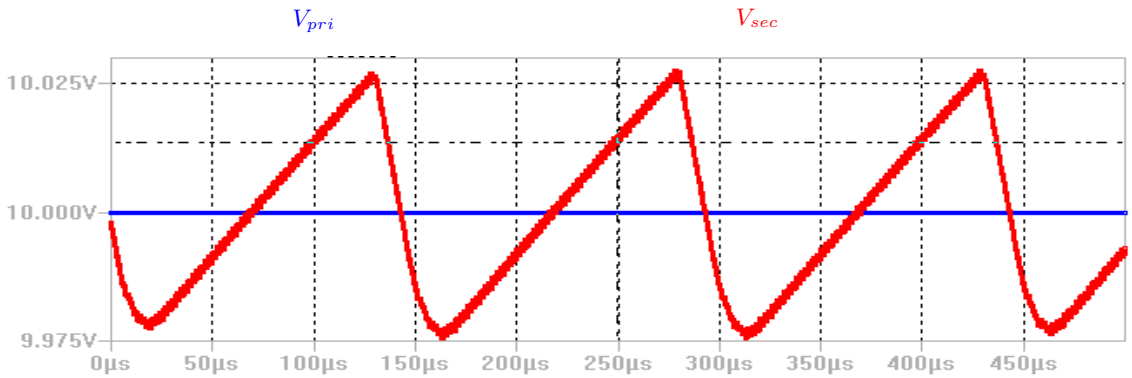

Figure 3.29. Primary and secondary side voltages of the proposed LLC converter with hysteresis control.

switches at the primary side are turned OFF. Again, when the secondary voltages falls below the primary voltage to a value also defined by the controller, the switches at the primary side are turned ON again and power delivery is restarted. The duration of the ON-OFF time depends on the output capacitor of the converter.

3.5 Realization of the Proposed Bidirectional LLC Converter

The experimental realization of the proposed bidirectional isolated LLC converter is presented in this section. The block diagram of the proposed converter is presented first. A design example of the transformer and the resonant inductor is discussed. Later, details of the circuits of the converter at various stages are also shown with brief descriptions. Also, the relevance of the double-band hysteresis thresholds is discussed.

Finally, experimental results are shown. The performance of the converter is verified in two steps. First, for a set of resistive loads, the efficiency of the converter in both directions is analyzed. The voltage and current waveforms at various stages of the converter are observed. Secondly, in the laboratory, three converters are employed to balance mismatch voltages among the submodules of a PV module.

3.5.1 Block Diagram of the Proposed Converter

The block diagram of the proposed converter along with the controller section is shown Fig. 3.30. First, considering that the power is transferred from primary to secondary, a

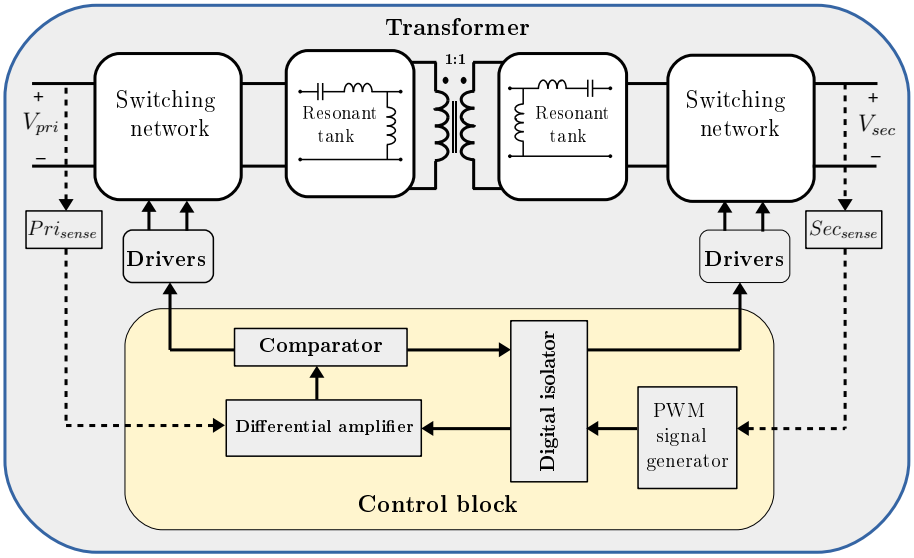

Figure 3.30. Block diagram of the prototype converter.

dc input voltage is inverted to an *ac* voltage by the switching network. The *ac* voltage is then passed through a resonant network and a high frequency transformer. At the secondary side of the converter, that *ac* voltage is rectified by a bridge rectifier. The control section of the converter decides the power transfer direction and activates the corresponding switching network.

3.5.2 Resonant Tank of the Proposed LLC Converter

Transformer and Resonant Inductor:

The isolated LLC converter features a transformer and resonant inductors that can be constructed with the same magnetic component by intentionally increasing the leakage inductance up to the required value. One possible approach is to place the windings separately in the core. Following the specifications of Table 3.4, the transformer of the LLC converter presents a magnetizing inductance of 28.8 µH, and resonant inductances of 4.43 µH,. The required turns ratio between the primary and secondary is 1:1. Considering that the power rating is 15 W, according to the input impedance, the *rms* current through the primary inductor is approximately $I_{r1,rms} = 1.5$ A, which approximately matches the secondary current $I_{r2,rms} = 1.5$ A. The total *rms* winding current referred to the primary is $I_{tot} = I_{r1,rms} + I_{r2,rms} = 3$ A

According to the requirement, the transformer is to be designed for self inductance of

$$L_{11} = L_M + L_{lk} = 28.8{+}4.43 = 33.23 \text{ µH},$$

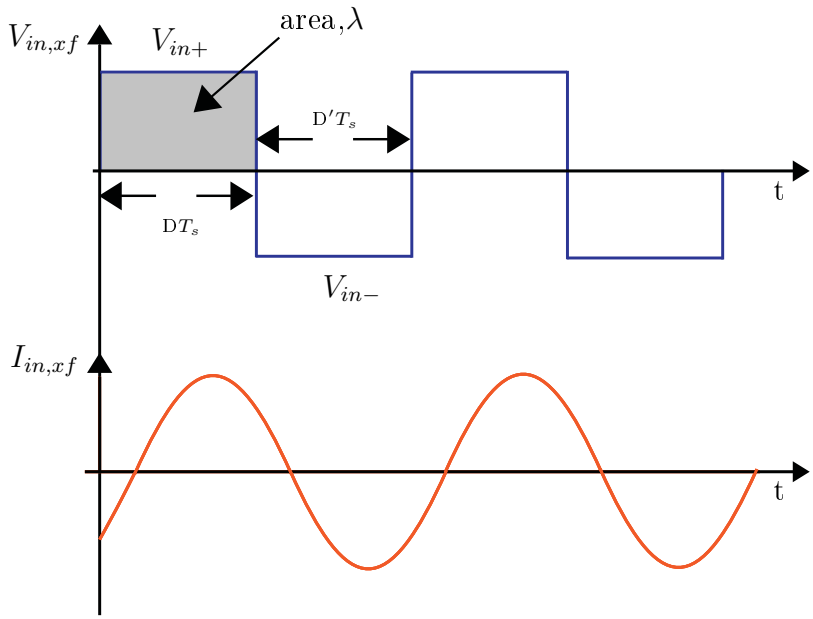

Figure 3.31. Input voltage and current of the transformer of the LLC converter.

where L_M is the magnetizing inductance of the transformer and L_{lk} is the leakage inductance which will be considered as primary and secondary resonant inductances.

Based on the method described in [54], the core size of the transformer can be determined by the following equation

$$K_{gfe} = \frac{\rho {\lambda_1}^2 {I_{tot}}^2 {K_{fe}}^{2/\beta}}{4K_u P_{tot}^{(\beta+2)/\beta}} \times 10^8 \tag{3.21}$$

Where, k_u = winding fill factor, ρ = wire effective resistivity, β = core loss exponent, K_{fe} = core loss coefficient, P_{tot}= allowed total power dissipation, λ_1 = applied primary volt-second and I_{tot}= total *rms* winding current. A fill factor of $k_u = 0.5$ is assumed and total power loss of $P_{tot} = 0.25$ W is allowed. A ferrite RM core consisting of the Magnetic, Inc. P-material is to be used. At 150 kHz, this material is described by the following parameters: K_{fe}= 18 W/Tβcm^3, β =2.6. Copper wire, having a resistivity of 1.724x10-6 Ω-cm, is to be used. The voltage and current waveforms of the modified resonant tank are shown in Fig. 3.31. It should be noted that, if the LLC converter is switched at resonant frequency, square wave voltage whose peak value is equal to the input voltage will appear across the transformer primary and secondary of the LLC converter but the current through the resonant inductor will be sinusoidal.

The volt-second applied to the primary reported in Fig. 3.31 is,

$$\lambda_1 = DT_sV_{in} = (0.5)(\frac{1}{150 \times 10^3} \text{ sec})(10 \text{ V}) \tag{3.22}$$

$$= 33.33 \text{ V} - \mu\text{sec}$$

By evaluating Eq. 3.21 the lowest size of the core for this application can be found

$$K_{gfe} \geq \frac{(1.724 \times 10^{-6})(33.33 \times 10^{-6})^2(4)^2(18)^{2/2.6}}{4(0.5)(0.25)^{(4.6/2.6)}} \times 10^8$$

$$= 92.5 \times 10^{-6} \tag{3.23}$$

Ferrite cores of various shapes provided by several manufactures can be used. However, the geometric constant, K_{gfe} of the selected core has to be higher than what has been found from Eq. 3.23. For instance, RM 12 core can be considered. The dimensions of the core are as follows,

Cross sectional area, $A_c = 1.46$ cm^2

Bobbin winding area, $W_A = 0.73$ cm^2

Mean length per turn, MLT=1.90 cm

Magnetic path length, $l_m = 6.1$ cm

K_{gfe} of the core RM 12 can be found by the following equation,

$$K_{gfe} = \frac{W_A A_c^{2(1-1/\beta)}}{MLT l_m^{2/\beta}} u(\beta) \tag{3.24}$$

For $\beta = 2.7$, $u(\beta)$ is equal to 0.305 [54]. Hence, K_{gfe} of the selected core can be found by evaluating Eq. 3.24 as

$$K_{gfe} = 0.0163$$

For $\beta = 2.6$, the geometrical constant K_{gfe} can be found by the following equation

$$K_{gfe} = \frac{W_A {A_c}^{2(\beta-1)/\beta}}{(MLT){l_m}^{(2/\beta)}} \left[\left(\frac{\beta}{2}\right)^{-(\frac{\beta}{\beta+2})} + \left(\frac{\beta}{2}\right)^{(\frac{2}{\beta+2})} \right]^{-(\frac{\beta+2}{\beta})} \tag{3.25}$$

$$= 0.0150$$

In both cases of β, the geometrical constant K_{gfe} of the selected core is higher than the required value.

In order to verify that the core will not be saturated by the peak current, the peak ac flux density can be found by the following equation,

$$\Delta B = \left[\frac{\rho\lambda_1^2(I_{tot})^2}{2K_u}\frac{(MLT)}{W_A{A_c}^3 l_m}\frac{1}{\beta K_{fe}} \times 10^8\right]^{\frac{1}{\beta+2}} \tag{3.26}$$

$$= 0.0206 \text{ Tesla}$$

The flux density calculated by Eq. 3.26 is considerably less than the saturation flux density of 0.47 Tesla of the P material from Magnetic Inc. [5].

The number of turns required for the transformer can be determined by the following equation,

$$n = \frac{\lambda_1}{2\Delta B A_c} \times 10^4 \tag{3.27}$$

$$\approx 6$$

If μ is the permeability of the core, then $\mu = \mu_r\mu_0$; where μ_r is relative permeability of the core material and μ_0 is the permeability of the air which is equal to $4\pi \times 10^{-7}$ H/m. The P material from Magnetics has a relative permeability of 3500 at 60^0C [5]. Hence, the self inductance of the primary winding can be determined by Eq. 3.28,

$$L_{11} = \frac{n^2\mu A_c}{l_m} \tag{3.28}$$

$$\approx 378 \text{ µH}$$

As mentioned before, a self inductance of L_{11}=33.23 µH is required for the proposed LLC converter. To achieve the required self inductance, air gap can be employed. The self inductance of a core, having an air gap of l_g and magnetic path length of l_m, can be calculated by the following equation,

$$L_{11} = \frac{n^2}{\frac{l_m}{\mu A_c} + \frac{l_g}{\mu_0 A_c}} \tag{3.29}$$

By taking a convenient number of turns and air gap, the desired self inductance can be achieved. For instance, considering an air gap of (2×0.127) mm and a number of turns equal to 7, the inductance can be found from Eq. 3.29 is $L_{11} = 33.24$ µH. It must be noted that addition of air gap will allow a higher value of winding current without saturation in the transformer.

Table 3.5. Transformer parameters of the proposed LLC converter.

Parameter	Value
# Turns (primary and secondary)	7
# Strings (primary and secondary)	130
String diameter	0.04 mm
Core type	RM12 (with bobbin)
Core material	N49
Air gap	(0.127×2) mm

Table 3.6. Parameters of the resonant tank of the proposed LLC converter.

Parameters	Value
Primary self inductance, L_{11}	30-33 µH
Secondary self inductance, L_{22}	30-33 µH
Primary leakage inductance, L_{12}	4.5-4.7 µH
Secondary leakage inductance, L_{22}	4.5-4.7 µH

The transformer is wired in such a way that the leakage inductance is sufficiently large and behaves as the resonant inductance. For that purpose, the coupling coefficient is reduced deliberately by using a large bobbin former and by placing the two coils in different limbs of the transformer. The parameters of the transformer that provide the desired leakage and magnetizing inductances are presented in Table 3.5. The properties of the resonant tank is also presented in Table 3.6.

Resonant Capacitors:

To realize the resonant capacitor according to the Table 3.4, two COG/NPO capacitors of 0.1 µF connected in parallel are placed in series with both sides of the transformer.

3.5.3 Power and Control Stages of the Converter

The description of the various stages of the schematic diagram of the proposed converter is presented as follows,

Power Stage: The full-bridge switching network of the primary and secondary side of the converter consists of low voltage IRFML8244TRPBF MOSFETs and DFLS230L-7

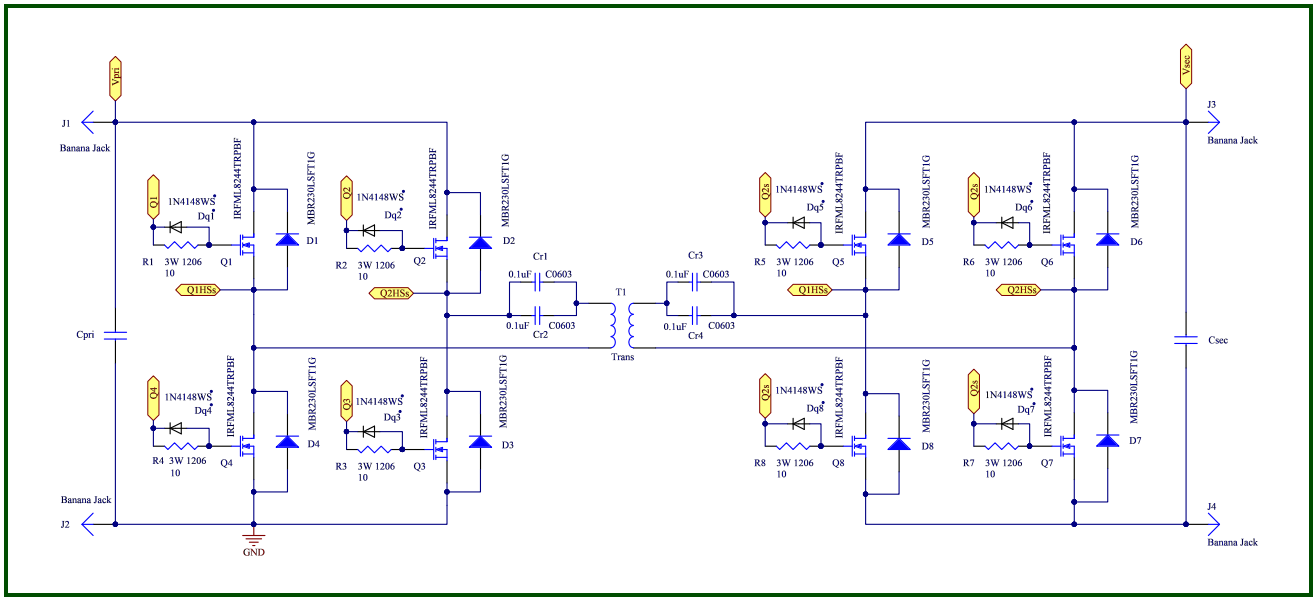

Figure 3.32. Schematic of the power stage of the proposed converter.

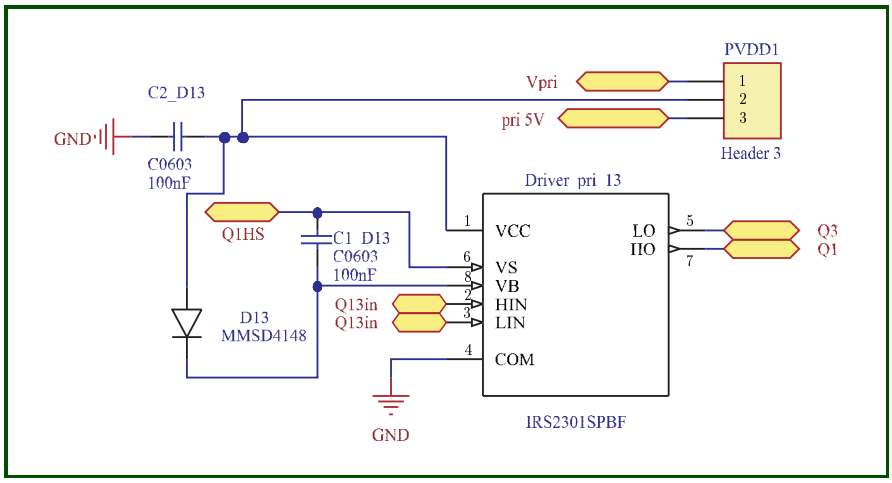

Figure 3.33. Schematic of the buck converter for 5 V supply.

Schottky rectifiers. 10 Ω resistance is connected at the gates of the MOSFETs to reduce ringing. MMSD4148T3G diodes are used in parallel with the gate resistor to discharge the gate voltage during the turning OFF of the MOSFETs. The switching networks and their components are shown in Fig. 3.32.

Power Supply: High efficient step-down dc-dc synchronous buck converters from Texas Instrument (TPS62120DCNT) are used to supply the circuitry of both primary and secondary. The operating input voltage range of the buck converter is 2 V to 15 V which is compatible with the typical output voltages of the submodules. The buck converter can provide 75 mA current with an efficiency up to 96%. The buck converters are configured to supply 5 V which matches the supply needed by the ICs in the control circuit and all

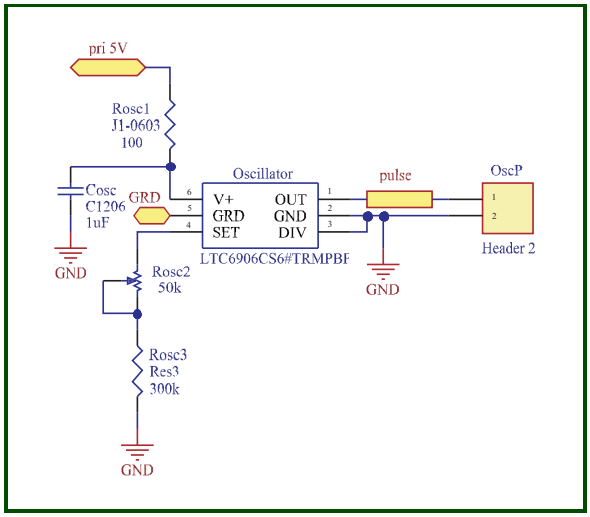

Figure 3.34. Schematic of the pulse generator circuit.

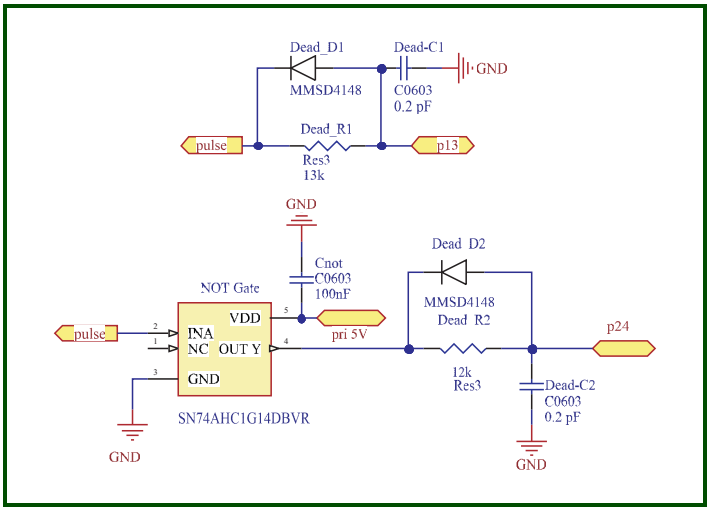

Figure 3.35. Dead time generation to avoid cross conduction.

other components. The schematic diagram is shown in Fig. 3.33.

Pulse Generator: A square wave voltage with an amplitude of 5 V is generated by a precision programmable oscillator from Linear Technology (LTC6906). A RC filter circuit is added to make the component compatible with 5 V input supply. The schematic diagram is shown in Fig. 3.34.

Dead Time Generator: In order to avoid cross-conduction among the switches, a small delay is required between the turn ON and turn OFF of the switches. One of the possible ways to introduce this delay is using RC circuit before the inputs of the MOSFET drivers. The schematic diagram of the circuit that is used in the prototype converter is shown in Fig. 3.35. It is important to note that the delay time has to be chosen carefully. Dead time should be sufficiently long to allow ZVS but short enough to prevent losses

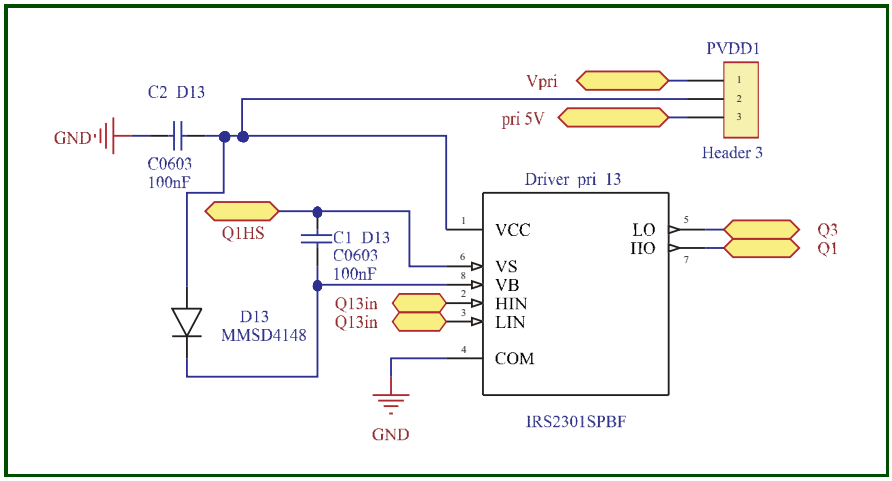

Figure 3.36. MOSFET driver circuit.

and other undesired behaviour.

MOSFET Driver: MOSFET drivers with independent high and low side referenced output channels are used. Two drivers are required for each primary and secondary sides. Both high side and low side inputs of the drivers are shorted and fed by a 5 V square wave and inverted square wave accordingly to switch each pair of MOSFETs. The schematic diagram of the driver connections of the primary side MOSFETs $Q1, Q3$ is shown in Fig. 3.36.

PWM Signal Generator: In order to compare the secondary voltage with the primary voltage, a scaled down version of the secondary voltage has be to transferred to the primary side of the converter. With the purpose of employing a low power digital isolator, which will help in improving light load efficiency, a pulse width modulation (PWM) technique is used [58]. The digital isolator is used to fetch the PWM signal from secondary to primary so that the isolation between them remains unaffected. First, a triangular wave is generated by low power op-amp and comparators. The triangular wave is then passed through another comparator to produce a pulse width modulated signal whose duty-cycle is inversely proportional to the secondary scaled signal amplitude. The schematic diagram of the PWM signal generator is shown in Fig. 3.37(a). In addition to that, as shown in Fig. 3.37(b), an error amplifier is introduced in order to ensure the accuracy and linearity of the PWM signal.

Digital Isolator: The digital isolator of the converter has two purposes. First, in order to keep the isolation between primary and secondary, the scaled secondary signal has to pass through the digital isolator after pulse width modulation. Secondly, the sec-

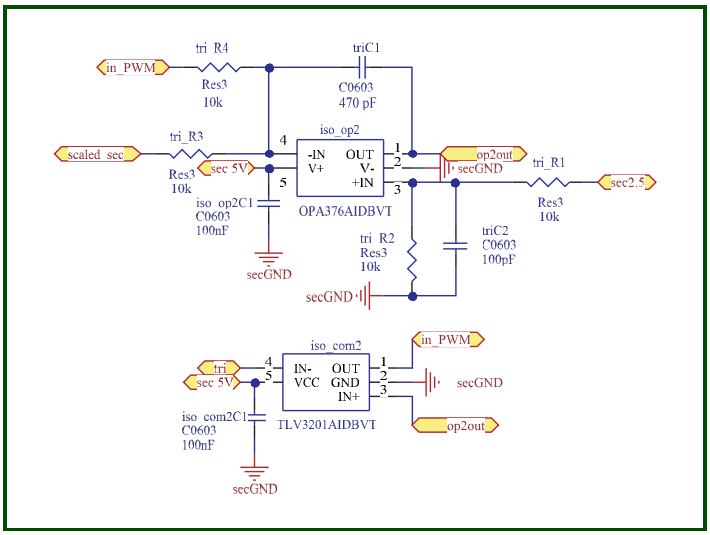

(a) Triangular wave generator.

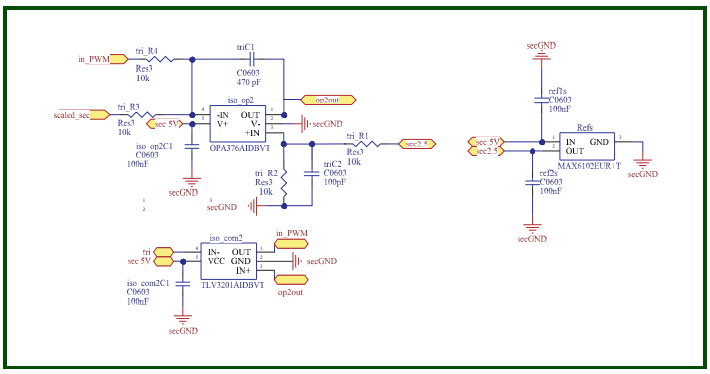

(b) Error amplifier.

Figure 3.37. PWM signal generator.

ondary enable and disable signals are generated by the primary side circuitry. Therefore, secondary enable or disable signals have also to be passed through the digital isolator. A MAX12931BASA+ digital isolator is used in this prototype. It is worth mentioning that the MAX12931BASA+ has the special property of being high at the output with no input (floating). The circuit diagram is presented in Fig. 3.38. Since the PWM circuitry generates an inverted signal, a NOT gate is used between the digital isolator and the filter circuit.

Differential Amplifier: In order to get the difference between the scaled primary and secondary voltages, a differential amplifier as shown in Fig. 3.39, is used in this prototype. The voltage gain of the differential amplifier is set to 20. In addition to that, the differential amplifier is configured with a reference of 2.5 V so that the output or the

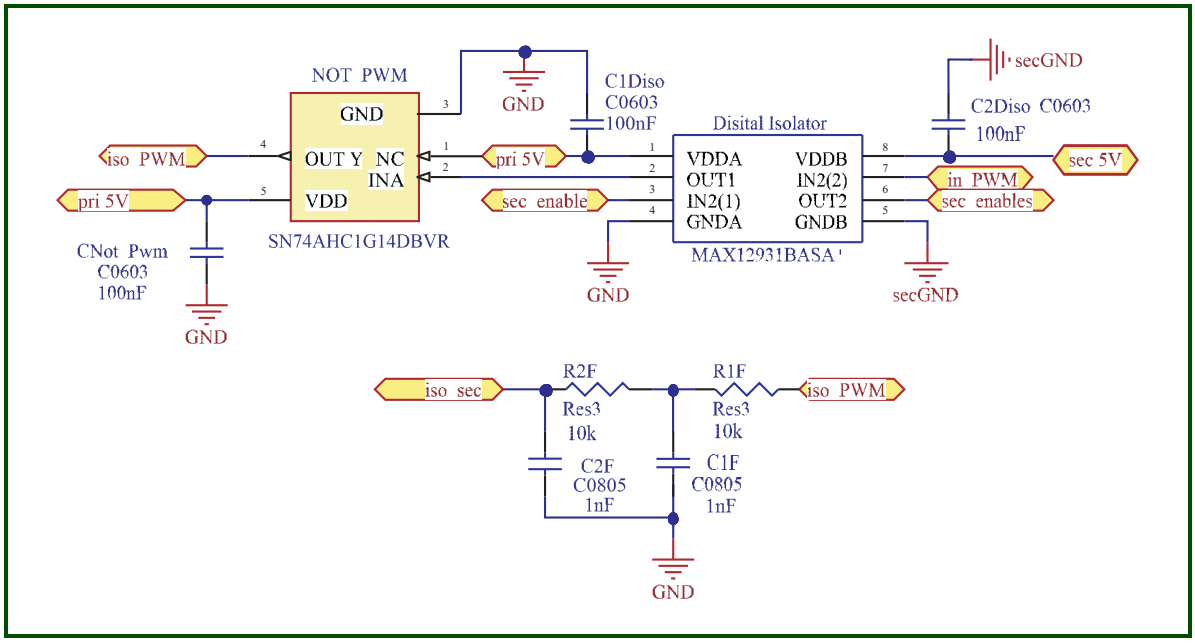

Figure 3.38. Digital isolator and NOT gate.

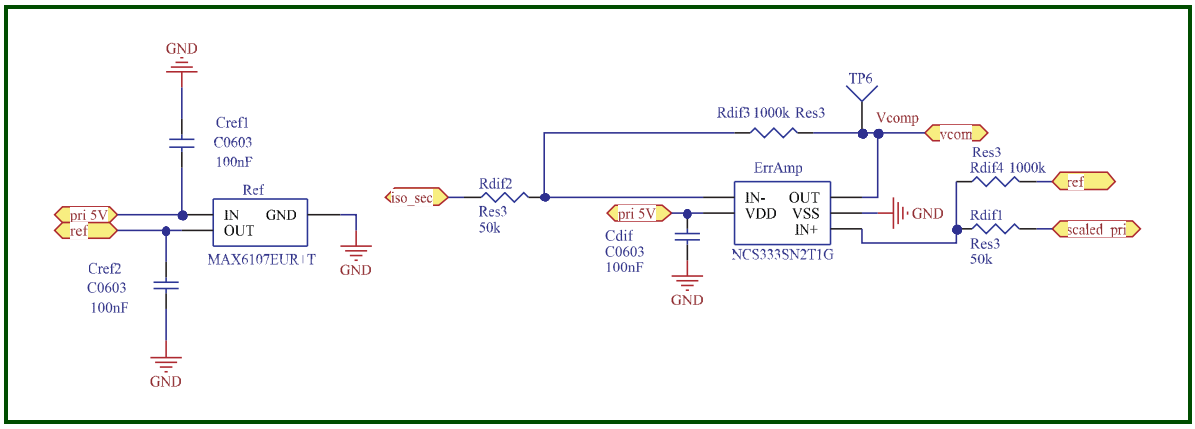

Figure 3.39. Differential amplifier.

error signal follows Eq. 3.30.

$$error = 2.5 + (V_{pri,scaled} - V_{sec,scaled}) \times 20 \qquad \text{V} \tag{3.30}$$

The *error* (V_{com}) signal is then compared with the predefined threshold voltages in order to select the power transfer direction of the converter.

Hysteresis Control with Comparator: The control scheme of the converter is realized by the hysteresis operation of the general purpose comparator. A threshold voltage of 150 mV of 75 mV is set for turning ON and OFF the converter respectively. In other words, when the primary voltage is 150 mV higher than the secondary voltage, the primary H-bridge will be activated and when the secondary voltage is higher than the

primary voltage by 75 mV, the power transfer from primary to secondary will be stopped. Similarly, if the voltage difference between primary to secondary goes below negative 150 mV, the secondary will start transferring power and the power transfer process will be ceased if the difference is 75 mV. The conditions of turning ON and OFF of the converters are summarized below,

(i) V_{pri} - $V_{sec} \geq$ 150 mV - - - - - - - - - - - - Primary turns ON,

(ii) V_{pri} - $V_{sec} \leq$ -75 mV - - - - - - - - - - - - Primary turns OFF,

(iii) V_{pri} - $V_{sec} \leq$ -150 mV - - - - - - - - - - - Secondary turns ON,

(iv) V_{pri} - $V_{sec} \geq$ 75 mV - - - - - - - - - - - - - - Secondary turns OFF.

Following Eq. 3.30 and the conditions listed above, the threshold voltage of the comparators are set. For instance, if the nominal value and, the scaled value of the primary and secondary sides are 10 V and 3 V respectively, the realization of the hysteresis control of the converter can be achieved by the following procedure,

Condition 1 : Primary ON The primary will be turned ON when the primary voltage is $(10 + 0.15)$ V $= 10.15$ V and the secondary voltage remains 10 V. Hence,

$$V_{pri} = 10.15 \text{ V}$$
$$V_{sec} = 10 \text{ V}$$
$$\text{Scaled primary, } V_{pri,scaled} = \frac{3 \times 10.15}{10} = 3.045 \text{ V}$$

Output of the differential amplifier,

$$V_{com} = 2.5 + (3.045 - 3) \times 20 = 3.4 \text{ V}$$

Therefore, the upper threshold of the first comparator is set to 3.4 V, i.e. when the output voltage of the differential amplifier reaches 3.4 V, the primary will be activated.

Condition 2 : Primary OFF The primary side will stop transferring power when the secondary voltage is $(10.15 + 0.075)$ V $= 10.225$ V and the primary voltage remains as before 10.15 V. Hence,

$$V_{pri} = 10.15 \text{ V}$$

$$V_{sec} = 10.225 \text{ V}$$

$$\text{Scaled secondary}, V_{sec,scaled} = \frac{3 \times 10.075}{10} \text{ V} = 3.0675 \text{ V}$$

Output of the differential amplifier,

$$V_{com} = 2.5 + (3.045 - 3.0675) \times 20 = 2.05 \text{ V}$$

Therefore, the lower threshold of the first comparator is set to 2.05 V, i.e. when the output voltage of the differential amplifier reaches 2.05 V, the primary will be deactivated.

Condition 3 : Secondary ON Similarly, considering the secondary side voltage 10 V, the power transfer from secondary to primary will be done if the primary side voltage is lower than the secondary voltage by 150 mV. Hence,

$$V_{sec} = 10 \text{ V}$$

$$V_{pri} = 9.85 \text{ V}$$

$$\text{Scaled secondary}, V_{sec,scaled} = 3 \text{ V}$$

$$\text{Scaled primary}, V_{pri,scaled} = \frac{3 \times 9.85}{10} = 2.955 \text{ V}$$

Output of the differential amplifier,

$$V_{com} = 2.5 + (2.955 - 3.0) \times 20 = 1.6 \text{ V}$$

Therefore, the lower threshold of the second comparator is set to 1.6 V, i.e. when the output voltage of the differential amplifier reaches 1.6 V, the secondary side of the converter starts transferring power to the the primary side.

Condition 4 : Secondary OFF The secondary side of the converter will be turned OFF when the voltage difference between primary and secondary reaches a certain value. However, the condition for turning OFF threshold of the secondary side has to be such that it does not turn ON the primary side while the secondary side is still ON. To maintain this condition, the secondary turn OFF threshold is set by considering the difference between primary to secondary voltage as 75 mV, i.e. the secondary side will stop transferring power when the primary voltage is $(10 + 0.075)$ V $= 10.075$ V and the secondary voltage remains as before 10 V. Hence,

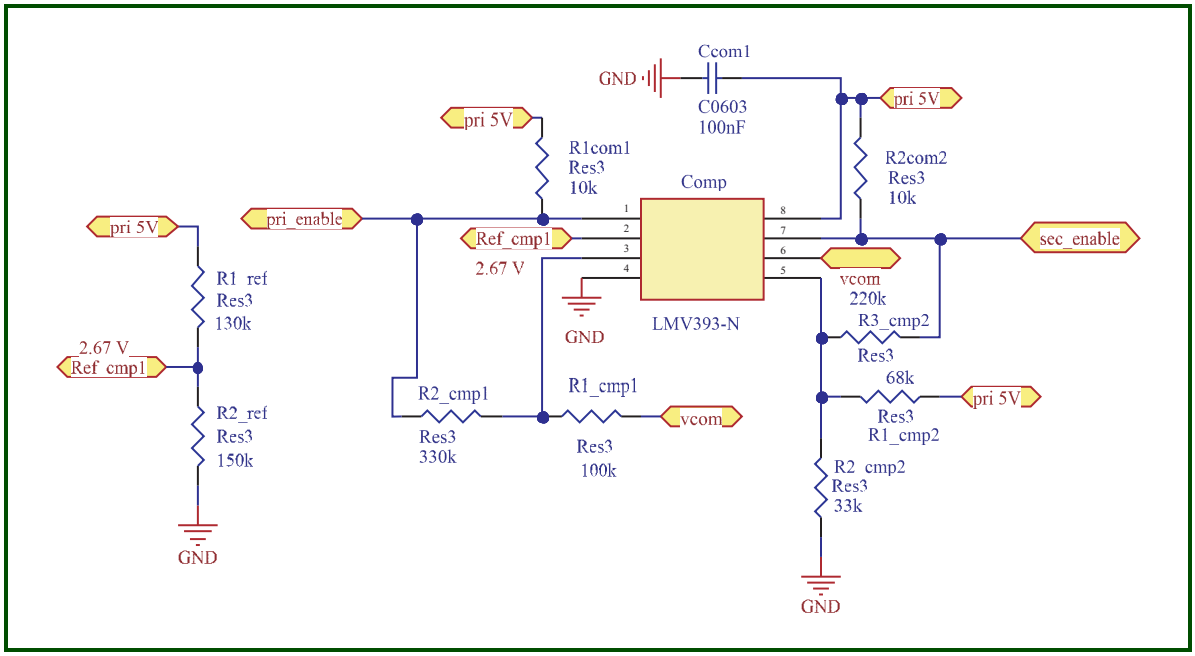

Figure 3.40. Hysteresis control circuit of the converter.

$$V_{pri} = 10.075 \text{ V}$$

$$V_{sec} = 10 \text{ V}$$

$$\text{Scaled primary, } V_{pri,scaled} = \frac{3 \times 10.075}{10} \text{ V}$$

$$= 3.0225$$

Output of the differential amplifier,

$$V_{com} = 2.5 + (3.0225 - 3) \times 20 = 2.95 \text{ V}$$

Therefore, the threshold voltage to turn OFF the secondary side of the converter is set to 2.95 V by the second comparator.

These turn ON and OFF conditions are established by two simple comparators with hysteresis. The schematic of hysteresis control circuitry developed by the LMV393N comparators is depicted in Fig. 3.40. The non-inverting hysteresis control connection is required for the activation-deactivation of the primary side. The secondary side is controlled by inverting hysteresis connections.

3.5.4 Steady-State Error

The proposed hysteresis-based controller inherently produces a steady-state error between the primary and secondary voltages. In our experiment, as mentioned earlier, we have

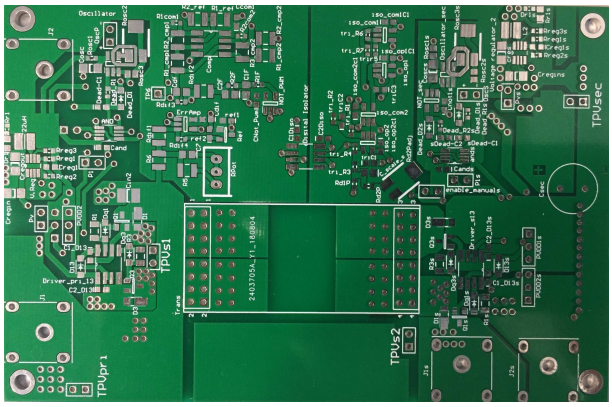

Figure 3.41. PCB of the bidirectional LLC resonant converter.

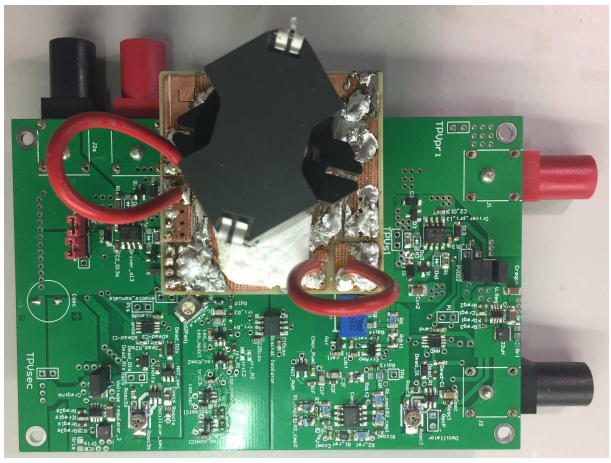

Figure 3.42. Experimentally realized bidirectional LLC resonant converter.

used thresholds $\overline{e_+} = 150$ mV, $\underline{e_+} = 75$ mV, $\overline{e_-} = -75$ mV and $\underline{e_-} = -150$ mV. This setup maintains the average error well below 200 mV. Nonetheless, a smaller error might be achieved by improving the immunity to noise of the circuit.

3.5.5 Steady-State Performance of the Converter

The commercially manufactured Printed Circuit Board (PCB) of the converter designed by Altium Designer is shown in Fig. 3.41. In this research Surface Mounted Devices (SMD) are used to realize the converters. One of the experimentally realized bidirectional LLC resonant converters is shown in Fig. 3.42. The performance of the converter is verified with a range of resistive loads of 500 mW to 8 W. Figure 3.43 shows a detail of the resonant tank input voltage, input current, output voltage and output current when the converter is ON in burst mode (for light load). The resonant tank of the converter is fed by a square-wave voltage, shown in Fig. 3.43(a), generated by switching the H-bridge alternatively with a *dc* input of 10 V. This square input voltage waveform of the resonant

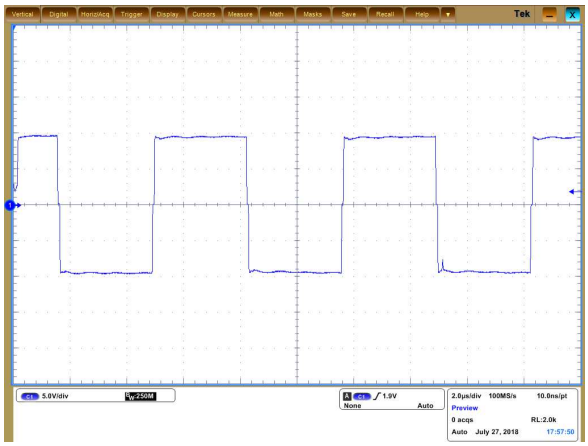

(a) Resonant tank input voltage.

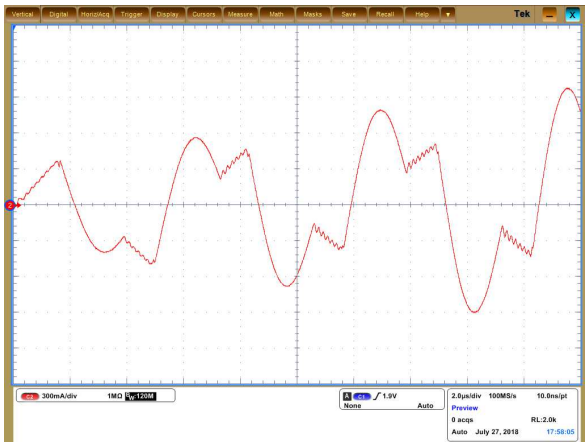

(b) Resonant tank input current.

(c) Resonant tank output voltage.

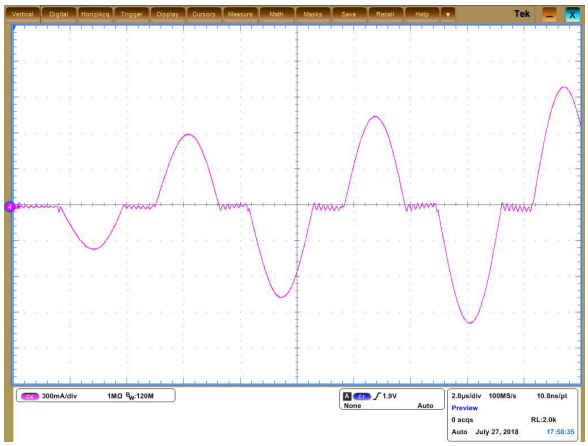

(d) Resonant tank output current.

Figure 3.43. Detail of the converter waveforms.

tank produces sinusoidal input current to the resonant tank as shown in Fig. 3.43(b). Since the switching frequency of the converter is lower that the resonant frequency, the current of resonant inductor reaches the magnetizing current before the end of the switching half cycle and forces the converter in boost mode operation. Figure 3.43(c) presents the output voltage of the resonant tank where an oscillation of voltage can be seen near the end of each half cycle. This happens because of the boost mode operation of the converter. The oscillation starts when the primary resonant inductor current reaches the magnetizing current and the secondary rectifier input current, shown in Fig. 3.43(d), reaches zero. Since the secondary rectifier stops conducting, the charge stored in the secondary side of the transformer generates an oscillation due to the parasitic elements of the circuit.

Figure 3.44(a) shows the input voltage (CH1) and the output voltage (CH3) of the converter in *ac* mode with a load of 1 W. It can be seen that the output voltage rises above the input voltage and the switching of the converter is stopped when the error reaches

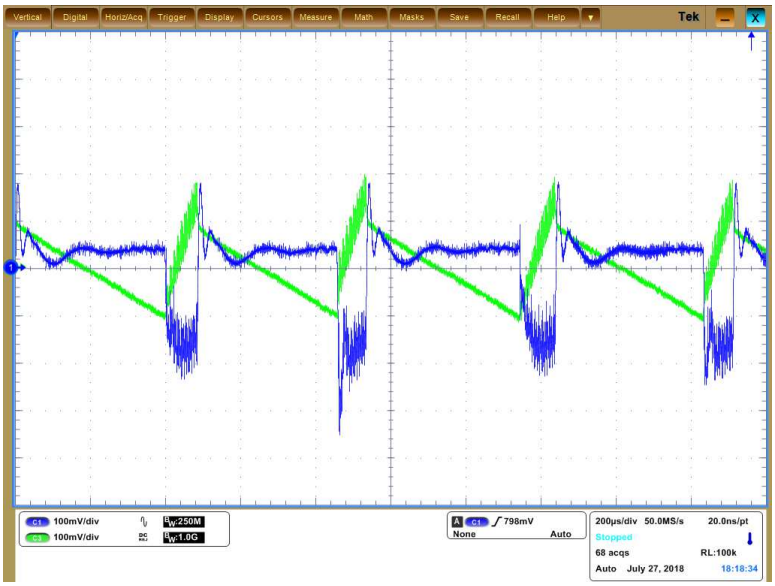

(a) Input/output voltage of the converter.

(b) Output voltage detail.

Figure 3.44. Detail of the converter waveforms.

the threshold. This results in a ON/OFF ratio of approximately 15%. For a heavier load it takes shorter time to discharge the output capacitor and the burst mode ratio will be increased. The ON/OFF threshold can be verified in Fig. 3.44(b). It can be seen that the difference between maximum and minimum value of the secondary voltage is 200 mV.

The realization of zero voltage switching operation of the converter in case of light load can be validated in Fig. 3.45. In case of 1 W, the resonant tank input voltage (CH1, blue) and current (CH2, red) along with resonant tank output voltage (CH3, green) and current (CH4, magenta) are shown Fig. 3.45(a). It can be seen that the resonant tank

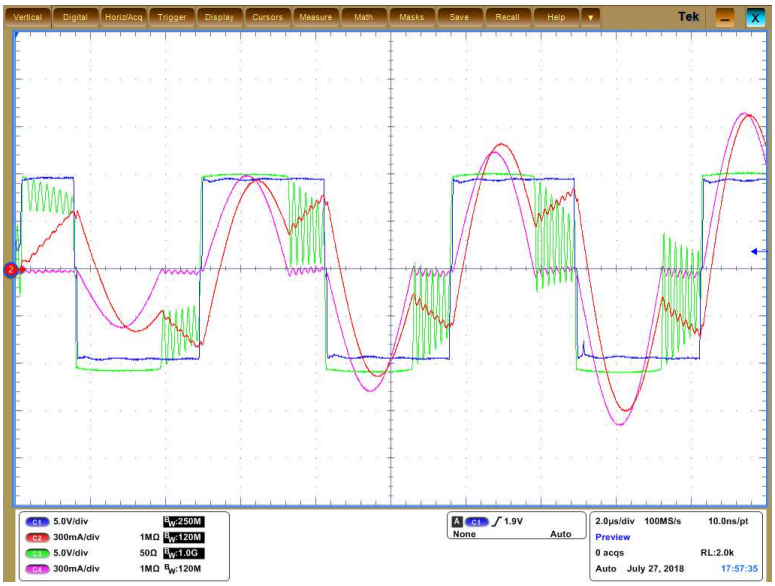

(a) ZVS at 1 W.

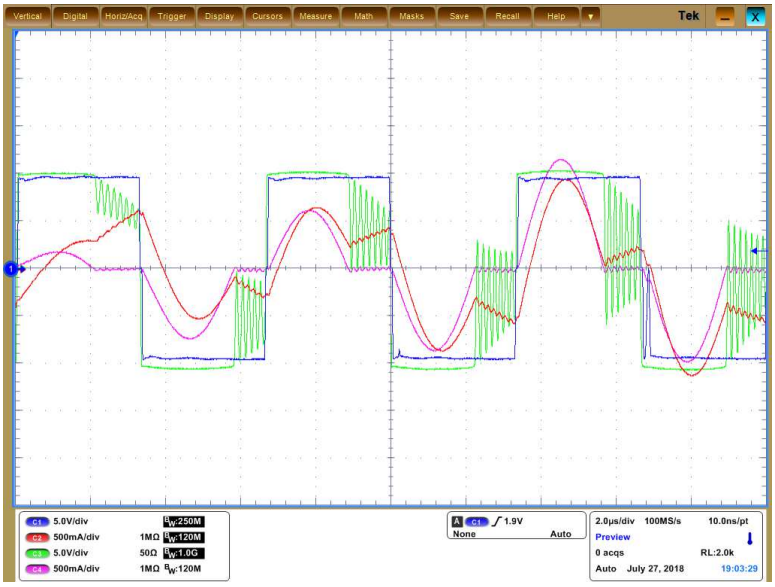

(b) ZVS at 2 W.

Figure 3.45. Zero voltage switching realization.

input current lags the resonant tank input voltage by approximately 30^0. Hence, zero voltage switching is achieved. Similarly, in case of 2 W (Fig. 3.45(b)), the resonant tank input voltage leads the current by approximately 25^0 and the converter operates at inductive region.

The efficiency curves of the converter in both forward (solid line with x mark) and backward (dotted line with o mark) directions for the loads from 500 mW to 8 W are shown in Fig. 3.46. The experimental results show an efficiency of 89% in case of 500 mW load using the burst-mode and maximum efficiency close to 93% at 3 W. For a load of 8 W,

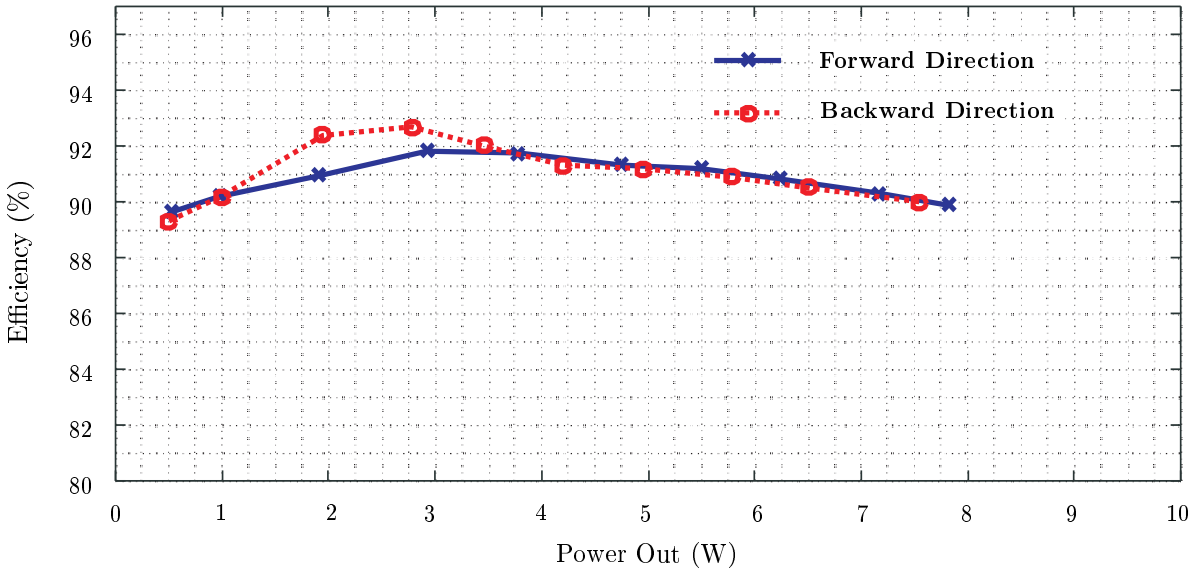

Figure 3.46. Efficiency of the proposed converter for loads between 500 mW and 8 W.

the converter is always ON and the efficiency drops to 90%. It must be noted that the converter does not present exactly identical properties in both power transfer directions. This happens due to several reasons. For instance, the leakage inductances which have been used as resonant inductances are not exactly the same. Therefore, the power transfer efficiency in both directions are not exactly equal. Nonetheless, the converter presents over 90% efficiency in both directions for the loads of our interest.

3.5.6 Verification of Mismatch Mitigation Performance

In order to verify the performance of the converters in presence of mismatch, three converter prototypes are attached in parallel with the bypass diodes of the submodules of a SUNTECH 175 WATT STP175S-24/Ac PV Module. The STP175S-24/Ac is a mono-si module which contains 72-cells and three substrings, connected in series. The specifications of the module is presented in Table 3.7. The experimental setup is shown in Fig. 3.47.

First, all the submodules are excited with 4 A DC current and a DC electronic load is connected with the module. The voltage of the DC electronic load is set such that maximum power can be obtained. It is observed that the electronic load dissipates a maximum power of 140.8 W at approximately 37.5 V and 3.75 A. Next, mismatches among the submodules are generated by varying the excitation currents and the performance of the converters is investigated by observing the primary and secondary voltages of the

Table 3.7. Module and submodule Parameters.

Electrical Data@STC (Model: STP175S-24/Ac)	Module	Submodule
Peak Power Watts-P_{MAX} (Wp)	175	58.33
Maximum Power Voltage-V_{MP} (V)	35.2	11.73
Maximum Power Current-I_{MPP} (A)	4.95	4.95
Open Circuit Voltage-V_{OC} (V)	44.2	14.73
Short Circuit Current-I_{SC} (A)	5.2	5.2
Module Efficiency η_m (%)	14.1	14.1

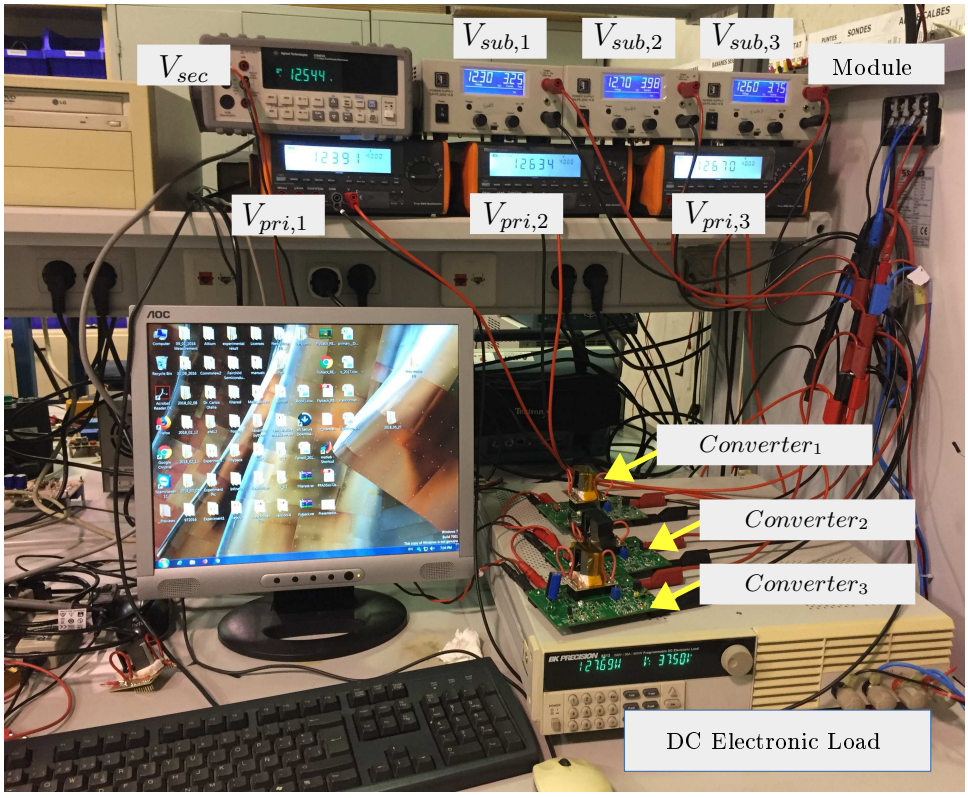

Figure 3.47. Experimental setup of three converters for voltage balancing (for Case. 1).

converters. In addition to that, output power is also observed. The irradiance has a direct linear relationship with the maximum power current. Reduction of irradiance, in this case the excitation current, forces maximum power current accordingly. For instance, reduction of 1 A current excitation will result in 1 A current reduction in the maximum power current. Three cases of mismatches are studied and presented as follows:

Case 1. In this case, mismatch among submodules is generated by reducing the current of the submodule 1 and the submodule 3 to 3.25 A and 3.75 A respectively. The

Table 3.8. Mismatch: Case 1.

$V_{sub,1}$	$V_{sub,2}$	$V_{sub,3}$	V_{sec}	P_{out} (W)
12.40	12.63	12.673		
$I_{sub,1}$	$I_{sub,2}$	$I_{sub,3}$	12.54	127.7
3.25	4	3.75		

submodule 2 is excited with 4 A as before. The submodules are operated at approximately 12.5 V. The results are summarized in Table 3.8.

If all the submodules operate at their maximum power points, the total maximum power output can be derived as follows,

$$\begin{aligned}
\text{Reduction of maximum power current of submodule 1} &= (4 - 3.25)\ \text{A} = 0.75\ \text{A} \\
\text{Reduction of maximum power current of submodule 2} &= (4 - 4)\ \text{A} = 0\ \text{A} \\
\text{Reduction of maximum power current of submodule 3} &= (4 - 3.75)\ \text{A} = 0.25\ \text{A} \\
\text{Total maximum power} &= (3.75 - 0.75) \times 12.5 \\
&\quad + (3.75 - 0) \times 12.5 \\
&\quad + (3.75 - 0.25) \times 12.5\ \text{W} \\
&= 128.125\ \text{W}
\end{aligned}$$

It can be seen that the expected power, if all submodules operate at their maximum power in presence of mismatch, is very close to the output power, as presented in Table 3.8, of the PV module after balancing the submodule voltage.

Case 2. A higher mismatch conditions are created in this case. The currents of the submodules 1, 2 and 3 are reduced to 3.5 A, 3.25 A and 3.75 A respectively. As before, the submodules are operated at approximately 12.5 V. The experimental results are summarized in Table 3.9. The derivations of Case 2 are as follows,

Table 3.9. Mismatch: Case 2.

$V_{sub,1}$	$V_{sub,2}$	$V_{sub,3}$	V_{sec}	P_{out} (W)
12.52	12.41	12.75		
$I_{sub,1}$	$I_{sub,2}$	$I_{sub,3}$	12.48	121.16
3.5	3.25	3.75		

Table 3.10. Mismatch: Case 3.

$V_{sub,1}$	$V_{sub,2}$	$V_{sub,3}$	V_{sec}	P_{out} (W)
12.38	12.7	12.6		
$I_{sub,1}$	$I_{sub,2}$	$I_{sub,3}$	12.48	130.625
3.5	4	3.75		

$$\begin{aligned}
\text{Reduction of maximum power current of submodule 1} &= (4 - 3.50)\ \text{A} = 0.50\ \text{A} \\
\text{Reduction of maximum power current of submodule 2} &= (4 - 3.25)\ \text{A} = 0.75\ \text{A} \\
\text{Reduction of maximum power current of submodule 3} &= (4 - 3.75)\ \text{A} = 0.25\ \text{A} \\
\text{Total maximum power} &= (3.75 - 0.50) \times 12.5 \\
&\quad + (3.75 - 0.75) \times 12.5 \\
&\quad + (3.75 - 0.25) \times 12.5\ \text{W} \\
&= 121.875\ \text{W}
\end{aligned}$$

The expected power after balancing the submodule voltages are close to the output power (shown in Table 3.9) as in Case 1.

Case 3: In this case, according to the mismatch conditions presented in Table 3.10, the V-I and V-P curves are generated by a voltage sweep of the DC electronic load and shown in Fig. 3.48 while only bypass diodes are connected in parallel to the submodules. The effect of mismatch can be seen in those figures.

Later, in presence of the same mismatch conditions presented in Table 3.10, the V-I and V-P curves are generated again while three converters are connected in parallel to the three submodules according to the PV-IP approach of the DPP architecture. The results are shown in Fig. 3.49. It can be seen that the prototype converters can mitigate

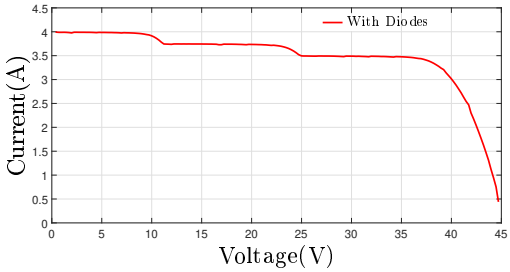

(a) V-I curve in presence of mismatch according to Table 3.10.

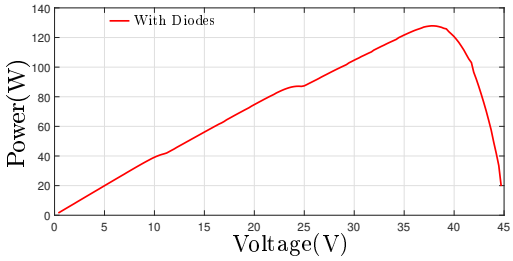

(b) V-P curve in presence of mismatch according to Table 3.10.

Figure 3.48. Voltage-current and voltage-power curves in presence of mismatch with conventional bypass diode.

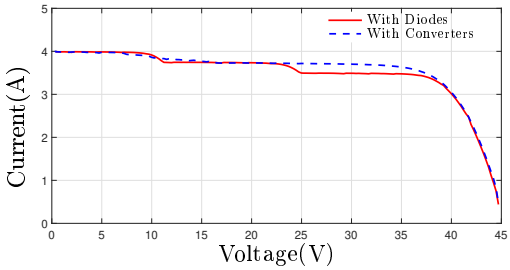

(a) V-I curve in presence of mismatch according to Table 3.10.

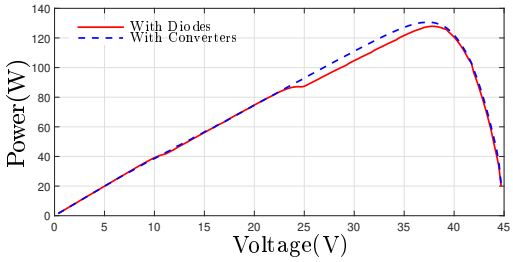

(b) V-P curve in presence of mismatch according to Table 3.10.

Figure 3.49. Voltage-current and voltage-power curves in presence of mismatch with the proposed converters.

Table 3.11. Power yield improvement by the converters with DPP architecture.

Module power production with the bypass diodes	127.7 W
Module power production with the converters	130.7 W

the mismatch and improve the energy production by balancing the submodule voltages. The summary of Case 3 is presented in Table 3.11.

3.6 Conclusions

An isolated bidirectional dc-dc converter for mitigating ageing mismatch in PV systems has been proposed in this chapter. The topology selection of the converter has been done by considering that it can meet the required characteristics to mitigate ageing mismatch at submodule level. A detailed design procedure of the converter has also been presented. Experimental realization of the converter and performance analysis has been done. First, steady-state performance of the converter has been verified by observing the voltage and

current waveforms at various stages of the converter for a set of resistive loads. It has been shown that for a range of load (1 W to 8 W), the converter provides an efficiency of more than 90%. In case of 500 mW, the converter provides an efficiency of 89%. It has also been verified that at light loads, the converters operate in the inductive zone and ZVS is achieved. The peak efficiency of the converter has been found as 93% at the range of 3 W to 5 W. The relevant captures of voltage and current waveforms have been presented.

Secondly, the performance of the converters in case of mismatch mitigation of a PV module has been verified in the laboratory. In order to create mismatch among the submodules of a module, three submodules of a PV module have been excited with different values of currents. DPP PV-IP approach has been followed to connect three prototype converters in parallel with the submodules to mitigate mismatch. It has been observed that, in presence of mismatch, these converters can force each submodule to operate very close to their maximum power point by balancing the voltages.

Chapter 4

Levelized Cost of Energy (LCOE)

One of the objectives of this thesis is to demonstrate that mitigation of ageing mismatch with distributed power electronics can decrease the cost of photovoltaic energy. In order to fulfil that objective, the cost of the power converters has to be reasonable with respect to the increase of the energy yield. This chapter evaluates the cost of the converters and estimates their influence on the levelized cost of energy (LCOE) for different types of PV systems.

4.1 LCOE

The LCOE is a well known term which represents the cost (in euros) of per unit energy production over the lifetime of a power plant. It is an internationally recognized method to compare the per unit energy production cost among different energy sources. In a very generalized way, the LCOE of a power plant can be defined as

$$LCOE = \frac{\text{Total cost of the power plant throughout the life}}{\text{Energy production throughout the life}}$$

4.2 Comparison of LCOE Between PV Systems and Other Form of Energy Sources

The LCOE of PV systems has decreased significantly due to an impressive decline in PV system cost during the last 30 years. It has been reported that the cost of PV systems has been decreased steadily to less than 1 € per installed peak W since 2012 [59]. The per unit peak power installation cost difference in the United States between Q1 2016 and Q1 2017 is \$0.18/Wdc (residential), \$0.32/Wdc (commercial), and \$0.42/Wdc (fixed-tilt utility-scale) [6]. The reduction in power production cost can be observed more clearly in Fig. 4.1.

Due to the decrease in per unit installation cost, the LCOE also has been declined accordingly. In 2010 the LCOE of small PV systems has been reported to be in the range of USD 0.36/kWh and USD 0.71/kWh. In case of utility-scale PV systems, the LCOE was estimated to be between USD 0.26/kWh and USD 0.59/kWh [60]. In contrast, the LCOE has been significantly decreased in 2018, reported as 3.17 $€_{Cents}$/kWh to 11.54 $€_{Cents}$/kWh [7]. A comparison of LCOE of renewable energy technologies and conventional power plants located in Germany in 2018 is shown in Fig. 4.2 [7]. It can be seen that the current LCOE of utility scale PV systems is below wind offshore and brown

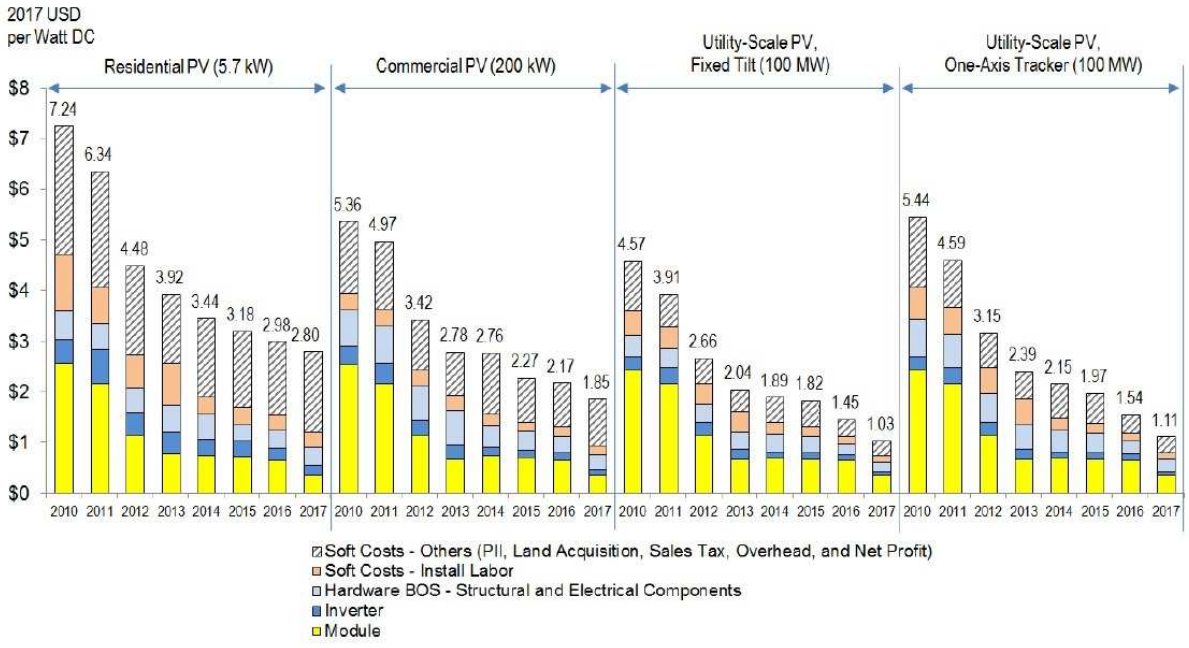

Figure 4.1. PV system cost decrease characteristics in U.S.A: year 2010 to year 2017 (from [6]).

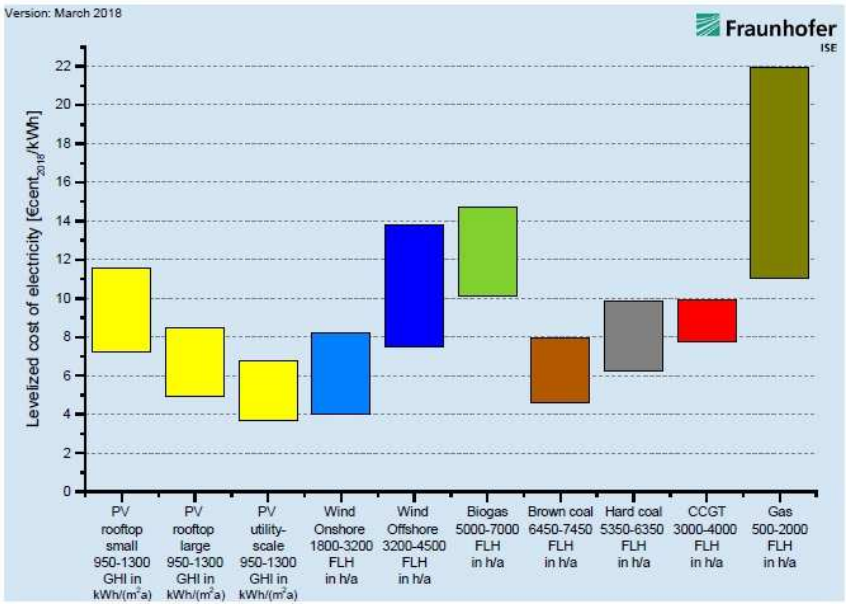

Figure 4.2. LCOE of renewable energy technologies and conventional power plants at locations in Germany in 2018. The value under the technology refers in the case of PV to the global horizontal irradiance (GHI) in kWh/(m^{2}a), for the other technologies to the annual full load hours (FLH). Specific investments are taken into account with a minimum and maximum value for each technology (from [7]).

coal power plants.

A further decrease in LCOE of PV systems could make this technology more competitive with respect to wind onshore power plants. In Chapter 2, the measured submodule level data estimates an energy yield increase in the range of 4-6% and therefore, an almost linear decrease of the LCOE is expected as:

$$\mathrm{LCOE}^* = \frac{\mathrm{Cost}}{\mathrm{Energy}(1+\frac{\Delta}{100})}\bigg|_{\frac{\Delta}{100}\to 0} \approx \mathrm{LCOE}(1-\frac{\Delta}{100}). \tag{4.1}$$

In other words, the LCOE could decrease approximately 4-6%, if the energy could be recovered. Such improvement requires power electronic converters whose cost is below the reported 4-6% gain. However, Eq. 4.1 is a simple approximation that disregards the cost of the additional power converters, and requires further analysis.

4.3 LCOE of PV Systems

In this section, the effect of introducing DPP converters on LCOE of PV systems is investigated. The calculation of initial LCOE is very complex since many variables have to be estimated and predicted with a long horizon. Considering $Cost_\phi$ as the initial total

cost of the energy of the system over 25 years and $Energy_\phi$ as the total energy yield by the system without the submodule converters over 25 years, the initial levelized cost of energy of the PV system, $LCOE_\phi$ can be expressed as follows,

$$LCOE_\phi = \frac{Cost_\phi}{Energy_\phi} \tag{4.2}$$

Now, if we introduce DPP converters in the system, the total lifetime energy yield as well as the total cost will be increased. This change in total energy yield and total cost will also modify the LCOE. Therefore, considering $LCOE_s$, $Cost_s$ and $Energy_s$ as the levelized cost of energy, the total cost of the system, the total energy yield by the system over 25 years respectively when converters are deployed in a PV system, the modified $LCOE_s$ can be expressed as,

$$LCOE_s = \frac{Cost_s}{Energy_s} = \frac{Cost_\phi + \Delta Cost}{Energy_\phi + \Delta Energy} \tag{4.3}$$

where,
$\Delta Energy$ is the energy improvement of the total system after introducing converters,
$\Delta Cost$ is the cost of the converter.

The linear approximation of Eq. 4.3 is

$$LCOE_s \approx \frac{Cost_\phi}{Energy_\phi} + \frac{\Delta Cost}{Energy_\phi} - \frac{Cost_\phi\ \Delta Energy}{Energy_\phi^2} \tag{4.4}$$

The difference from final LCOE ($LCOE_s$) to initial LCOE ($LCOE_\phi$) can be expressed as $\Delta LCOE$ and,

$$\begin{aligned}\Delta LCOE =& LCOE_s - LCOE_\phi \\ \approx& \frac{\Delta Cost}{Energy_\phi} - \frac{Cost_\phi \Delta Energy}{Energy_\phi^2}\end{aligned} \tag{4.5}$$

It can be seen from Eq.4.5 that the decrease in LCOE of the system can be achieved if $\frac{Cost_\phi \Delta Energy}{Energy_\phi^2} > \frac{\Delta Cost}{Energy_\phi}$. Additionally, it is also evident that the improvement of LCOE does depend on the initial system cost and energy.

Table 4.1. Average daily irradiance in Tarragona, Berlin and Jeddah.

	Irradiance		
Location	Tarragona	Berlin	Jeddah
Average Irradiance (kWh/m^{2}Day)	4.603333	2.72	5.86

4.4 Improvement of LCOE by Mitigating Ageing Mismatch

This section presents an estimation of the decrease of LCOE when power converters are introduced at submodule level. Analyses are done for a large utility-scale and a small rooftop PV system. Three different locations around the world are considered in order to observe the effect of irradiance variation on the modified LCOE. The average daily irradiances of Tarragona (Spain), Berlin (Germany) and Jeddah (Saudi Arabia) are shown in Table 4.1. The total cost of a PV system also varies according to the capacity. Typically, the LCOE of a utility-scale PV system is significantly lower than that of a small rooftop PV system.

4.4.1 Utility-scale PV Systems

A large utility-scale PV system of 100 MW located in Tarragona, Spain and operating in NOCT (45^{0}C) is considered first. The output power of the system at NOCT can be calculated as follows,

$$\begin{aligned} \text{Peak Power @ STC} &= 100000 \text{ kW} \\ \text{Peak Power @ NOCT} &= 90000 \text{ kW} \end{aligned} \tag{4.6}$$

Total Initial Energy, $Energy_\phi$**:** According to the Table 4.1, the average irradiance of Tarragona, Spain is 4.603333 kWh/m^{2}Day. From Eq. 4.6, the daily energy output of

Table 4.2. Yearly energy output of a Utility-scale PV system of 100 MW at Tarragona, Spain

1% degradation per year.					
Year	Energy	Unit	Year	Energy	Unit
1	151219500	kWh	14	131560965	kWh
2	149707305	kWh	15	130048770	kWh
3	148195110	kWh	16	128536575	kWh
4	146682915	kWh	17	127024380	kWh
5	145170720	kWh	18	125512185	kWh
6	143658525	kWh	19	123999990	kWh
7	142146330	kWh	20	122487795	kWh
8	140634135	kWh	21	120975600	kWh
9	139121940	kWh	22	119463405	kWh
10	137609745	kWh	23	117951210	kWh
11	136097550	kWh	24	116439015	kWh
12	134585355	kWh	25	114926820	kWh
13	133073160	kWh			
Total Energy over 25 years				3326829000	kWh

the system will be,

$$\begin{aligned} \text{Daily energy output @ Tarragona} &= (90000 \times 4.603333)\ \text{kWh} \\ &= 414300\ \text{kWh} \\ \text{and, the yearly energy output} &= (414300 \times 365)\ \text{kWh} \\ &= 151219500\ \text{kWh} \end{aligned} \tag{4.7}$$

Now, since it has been shown that the yearly degradation of a PV system is approximately 1%, the energy yield of every year of the PV system over a lifetime of 25 years is calculated from Eq. 4.8 and listed in Table 4.2.

$$Energy_{i+1} = Energy_i - Energy_1 \times 1\% \tag{4.8}$$

Hence, the total energy over 25 years @ Tarragona, $Energy_\phi$ is,

$$\begin{aligned} Energy_\phi &= \sum_{\phi=1,2,3\ldots}^{25} Energy_\phi \\ &= 3326829000\ \text{kWh} \end{aligned} \tag{4.9}$$

Initial Cost of the Total Energy, $Cost_\phi$: In order to calculate the initial cost of the system, Fig. 4.2 is redrawn in Fig. 4.3 indicating the average LCOE of the utility scale (solid red line) and small rooftop (dashed red line) PV systems. It can be seen that the average LCOE of the utility scale PV system is approximately 5.2 $€_{\text{Cents}}$/kWh. Therefore,

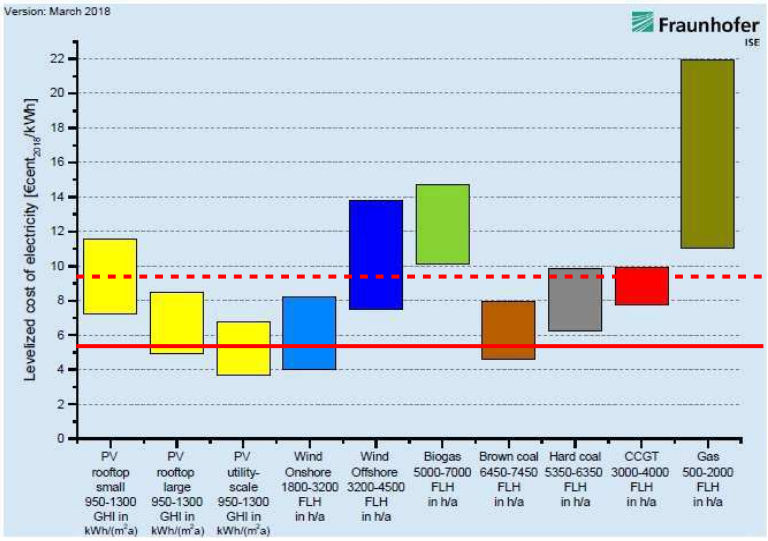

Figure 4.3. Cost calculation of a small rooftop and utility scale PV system based on reported LCOE in [7].

according to the Table 4.2 the total cost of the energy $Cost_\phi$ is

$$Cost_\phi = \frac{5.2 \times 3326829000}{100} \text{ €}$$
$$= 172995108 \text{ €} \tag{4.10}$$

Energy Improvement, $\Delta Energy$: In Chapter 2, Table 2.8, it has been shown that in case of utility scale PV system, by introducing 90% efficient converters, the recoverable energy improvement is approximately 5%. Therefore, from Eq. 4.9, $\Delta Energy$ is

$$\Delta Energy = 3326829000 \times 5\% \text{ kWh}$$
$$= 166341450 \text{ kWh} \tag{4.11}$$

Cost Increase, $\Delta Cost$: The cost of the converters depends on the price of many components such as semiconductors, magnetics, PCBs, and passive components. Most of the components of our prototype converter could easily be incorporated in an integrated circuit and thus overall cost of converters could be minimized to large extent. However, the cost of these components also varies according to the quantities and provider. Hence, it is difficult to estimate the exact cost of the converter. However, similar types of converters have been developed in [48] and estimated cost of a set of 3 converters has been reported to be 7 \$ (approximately 6 €). Since the PV module we are considering also has 3 submodules, the price of the set of 3 converters presented in [48] can be taken as an example.

The number of the required set of converters is equal to the number of PV modules

Table 4.3. $\Delta LCOE$ for residential and utility-scale PV systems at various irradiance conditions.

Location	System Type	W/m^{2}Day	Capacity (kW)	$LCOE_\phi$ (€$_{Cents}$/kWh)	$\Delta LCOE$ (€$_{Cents}$/kWh)	% Decrease
Tarragona	Residential	4.60	10	9.25	-0.34	3.70
	Utility-scale		100000	5.2	-0.182	3.50
Berlin	Residential	2.72	10	9.25	-0.29	3.11
	Utility-scale		100000	5.2	0.13	2.45
jiddah	Residential	5.86	10	9.25	- 0.36	3.88
	Utility -scale		100000	5.2	-0.2	3.81

in this utility-scale PV system. Based on the power rating of typical PV module, the number of the converters can be derived as follows,

$$\begin{aligned} \text{Module power} &= 0.23 \text{ kW} \\ \text{Utility scale system power} &= 100000 \text{ kW} \\ \text{No. of modules required for utility scale} &= \frac{90000}{0.23} \text{ Pcs} \\ \text{Set of converters required} &= 434782.6087 \approx 434783 \text{ Pcs} \\ \text{Hence,} \quad \Delta Cost &= 434783 \times 6 \text{ €} \\ &= 2608698 \text{ €} \end{aligned} \tag{4.12}$$

Improved LCOE, $\Delta LCOE$: The improvement of LCOE after introducing the converters can be derived by using the values of Eqs. 4.9, 4.10, 4.11 and 4.12 in Eq. 4.5.

$$\Delta LCOE = -0.181586121 \text{ €}_{\text{Cents}}/\text{kWh} \tag{4.13}$$

Eq. 4.13 represents an improvement of approximately -3.5% of the initial LCOE.

4.4.2 Effect of System Capacity and Irradiance Variation

It is our interest to investigate how the system capacity and irradiance variation may affect the improvement of LCOE with power converters. In order to examine the effect of different irradiance conditions, the same utility-scale system of 100 MW mentioned in the previous subsection is reinvestigated for different irradiance conditions as presented in Table 4.1. The results are summarized in Table 4.3.

The role of the system capacity of a PV installation on LCOE improvement is also

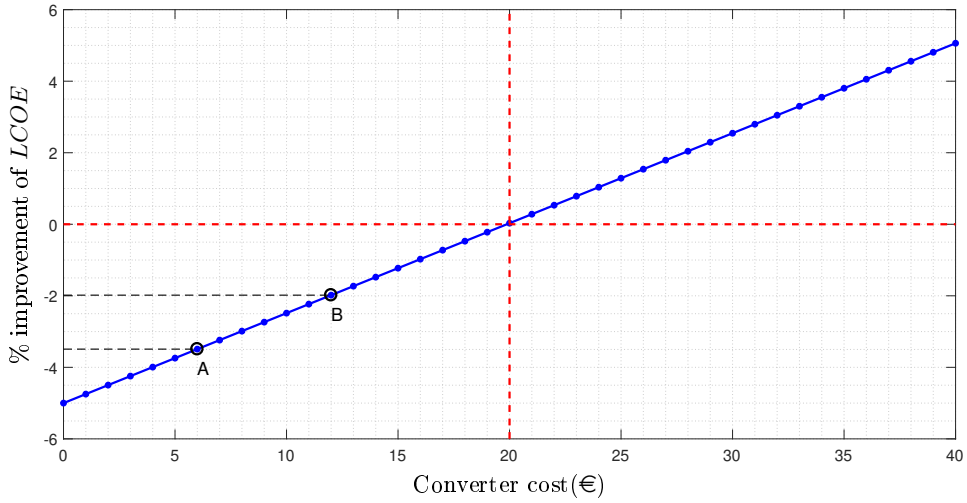

Figure 4.4. Effect of converter cost on LCOE for a utility-scale PV system located in Tarragona, Spain

examined. It is observed that the proposed solution for mitigation of ageing mismatch is relatively more effective with higher irradiance conditions and lower system capacity. The results of the investigations of a smaller rooftop at different irradiance conditions are also presented in Table 4.3.

In order to observe the effect of the change in cost of the converter on the improvement of LCOE, an analysis is done considering a utility-scale PV system of 100 MW located in Tarragona, Spain and improvement of the LCOE with respect to the cost of the converter is shown in Fig. 4.4. It can be seen that, if the converter cost is zero, the percentile improvement is exactly equal to the percentile improvement of the energy yield as predicted by the Eq. 4.1. In Fig. 4.4, it can also be seen that, when the converter cost exceeds 20 € the percentage improvement of LCOE becomes positive. In other words, for the case of aforementioned utility-scale PV system, the converter cost cannot exceed 20 € in order to reduce the LCOE by mitigating ageing mismatch.

In this research, the cost of the converters has been considered to be approximately 6 € and corresponding reduction of LCOE, for a specific case, is shown 3.5% as indicated by point A in Fig. 4.4. However, if the converters are required to be replaced in future, once in a lifetime of 25 years, the improvement of LCOE could be estimated by considering the converter cost as $6 \times 2 = 12$ € and the corresponding reduction of LCOE would be approximately 2% as indicated by point B in Fig. 4.4.

4.5 Conclusions

The LCOE of PV systems for both small rooftop and large utility-scale have been estimated based on 25 years of lifetime. There are several factors that could improve the LCOE to some extent. For instance, according to the datasheet provided by the manufacturer, even after 25 years the PV modules are able to produce 80% power of their initial rating. Therefore, it is very conservative approach to calculate the LCOE based on 25 years lifetime of a PV system. It would be more interesting to examine the effectiveness of the proposed converter based DPP architecture on LCOE studies in such cases where it has been considered that the lifetime of PV systems would be more than 25 years. Furthermore, it is expected that if the converters could be integrated within the modules by minimizing the size and cost, additional reduction in LCOE could be possible.

One important limitation of estimating the improvement of LCOE in this chapter is that the cost associated with the additional cabling, required to establish the connections among the submodules, has not been considered. Such cost could penalize the overall LCOE as well. It is important to note that, in this chapter, failure events of the DPP converters have not been considered since it has been reported that even in case of converter failure, the DPP architecture does not hamper the operation of the PV system, and can provide significant mismatch mitigation performance for a relatively large percentage of faults [18].

Chapter 5

Conclusions

This research has focused on the measurement and the modeling of submodule-level ageing effects. A detailed measurement procedure of I-V parameters of a population of 42 submodules has been presented with emphasis on the differences with respect to previously reported module level measurements. Attention has been paid to differences between short-circuit and maximum power currents as the number of results showing both measurements is scarce. Although the degradation rate should have remained unaffected by the granularity level, it has been shown that the CV of maximum power current at submodule level exhibits a higher value with respect to previous results at module level.

Since there is potential for unmeasured energy yield penalty due to submodule-level mismatch, the research has also aimed to quantify the recoverable power loss. First, the skewness of the distributions have been analyzed and non-gaussian statistical models in PV parameter modeling have been explored. It has been shown that previously reported negative skewness in the power and current distributions of PV systems impacts on long-term forecasts. Then, the efficiency and the 25 years power yield of several PV systems has been assessed by means of Monte Carlo simulations and compared with the previous results reported on the lifetime. In addition to that, it also has been shown that the distributed power electronics could effectively extend the lifetime of PV systems.

Based on the findings of the measured submodule level data, a resonant converter for submodule level mismatch mitigation has been analyzed and designed. First, power rating of the converter has been determined by comparing the required power processing ranges by different DPP architectures. Later, the topology of the converter has been selected based on the requirement of this specific application. A detailed design procedure and

experimental realization of the converter have also been presented. The performance of the converter has been evaluated in the following steps,

- Steady-state performance of the converter has been verified. The experimental results show an efficiency of 89% in case of 500 mW load using the burst-mode and maximum efficiency close to 93% at 3 W. For a load of 8 W, the converter is always on and the efficiency drops to 90%.
- The performance of the converters for mitigation of mismatch in a PV module has been verified by connecting three converters to the PV module. It has been observed that these converters can extract the maximum available power in presence of mismatch among the submodule currents.

In Chapter 4, a brief discussion has been done regarding the potential improvement of the LCOE by mitigating ageing mismatch. It has been shown that there is a linear relationship between the cost of the converters and improvement rate of LCOE. Based on the irradiance, three example cases have been studied. It has been shown that regarding LCOE, mitigation of ageing mismatch is relatively more effective, where annual irradiance is higher. For an example case, the maximum cost of the converters that could improve LCOE has been also presented. Using the statistical model proposed in this thesis, it has been shown that the LCOE can be reduced up to 3.5% for the mentioned example case.

References

[1] Fraunhofer Institute for Solar Energy Systems ISE, "Photovoltaics report," *[Online] Available here: https://www.ise.fraunhofer.de/en/publications/studies/photovoltaics-report.html.*, 2018.

[2] C. Chamberlin, M. Rocheleau, M. Marshall, A. Reis, N. Coleman, and P. Lehman, "Comparison of PV module performance before and after 11 and 20 years of field exposure," in *Photovoltaic Specialists Conference (PVSC), 2011 37th IEEE*, pp. 000101–000105, IEEE, 2011.

[3] D. C. Jordan, J. H. Wohlgemuth, and S. R. Kurtz, "Technology and climate trends in PV module degradation," *27th EU PVSEC*, pp. 3118–3124, 2012.

[4] C. Olalla, C. Deline, D. Clement, Y. Levron, M. Rodriguez, and D. Maksimovic, "Performance of power-limited differential power processing architectures in mismatched PV systems," *IEEE Transactions on Power Electronics*, vol. 30, no. 2, pp. 618–631, 2015.

[5] Magnetics®, *Ferrite Cores Catalog 2017*.

[6] R. Fu, D. J. Feldman, R. M. Margolis, M. A. Woodhouse, and K. B. Ardani, "Us solar photovoltaic system cost benchmark: Q1 2017," tech. rep., National Renewable Energy Lab. (NREL), Golden, CO (United States), 2017.

[7] Fraunhofer Institute for Solar Energy Systems ISE, "Levelized cost of electricity : Renewable energy tecgnologies," March 2018.

[8] J. Wohlgemuth and W. Herrmann, "Hot spot tests for crystalline silicon modules," in *Photovoltaic Specialists Conference, 2005. Conference Record of the Thirty-first IEEE*, pp. 1062–1063, IEEE, 2005.

[9] N. D. Kaushika and N. K. Gautam, "Energy yield simulations of interconnected solar pv arrays," *IEEE Transactions on Energy Conversion*, vol. 18, no. 1, pp. 127–134, 2003.

[10] M. Alonso-Garcia, J. Ruiz, and F. Chenlo, "Experimental study of mismatch and shading effects in the I–V characteristic of a photovoltaic module," *Solar Energy Materials and Solar Cells*, vol. 90, no. 3, pp. 329–340, 2006.

[11] D. C. Jordan, S. R. Kurtz, K. VanSant, and J. Newmiller, "Compendium of photovoltaic degradation rates," *Progress in Photovoltaics: Research and Applications*, vol. 24, no. 7, pp. 978–989, 2016.

[12] M. Vázquez and I. Rey-Stolle, "Photovoltaic module reliability model based on field degradation studies," *Progress in photovoltaics: Research and Applications*, vol. 16, no. 5.

[13] D. C. Jordan and S. R. Kurtz, "Photovoltaic degradation rates-an analytical review," *Progress in photovoltaics: Research and Applications*, vol. 21, no. 1, pp. 12–29, 2013.

[14] D. Polverini, M. Field, E. Dunlop, and W. Zaaiman, "Polycrystalline silicon PV modules performance and degradation over 20 years," *Progress in photovoltaics: research and applications*, vol. 21, no. 5, pp. 1004–1015, 2013.

[15] G. Makrides, B. Zinsser, M. Schubert, and G. E. Georghiou, "Performance loss rate of twelve technologies under field conditions using statistical techniques," *Solar Energy*, vol. 103, pp. 28–42, 2014.

[16] M. A. Mikofski, D. F. Kavulak, D. Okawa, Y.-C. Shen, A. Terao, M. Anderson, S. Caldwell, D. Kim, N. Boitnott, J. Castro, *et al.*, "PVLife: an integrated model for predicting PV performance degradation over 25+ years," in *Photovoltaic Specialists Conference (PVSC), 2012 38th IEEE*, pp. 001744–001749, IEEE, 2012.

[17] C. Olalla, C. Deline, and D. Maksimovic, "Performance of mismatched PV systems with submodule integrated converters," *IEEE Journal of Photovoltaics*, vol. 4, no. 1, pp. 396–404, 2014.

[18] C. Olalla, D. Maksimovic, C. Deline, and L. Martinez-Salamero, "Impact of distributed power electronics on the lifetime and reliability of PV systems," *Progress in Photovoltaics: Research and Applications*, 2017.

[19] G. R. Walker and P. C. Sernia, "Cascaded dc-dc converter connection of photovoltaic modules," *IEEE transactions on power electronics*, vol. 19, no. 4, pp. 1130–1139, 2004.

[20] L. Linares, R. W. Erickson, S. MacAlpine, and M. Brandemuehl, "Improved energy capture in series string photovoltaics via smart distributed power electronics," in *Applied Power Electronics Conference and Exposition, 2009. APEC 2009. Twenty-Fourth Annual IEEE*, pp. 904–910, IEEE, 2009.

[21] S. Poshtkouhi, V. Palaniappan, M. Fard, and O. Trescases, "A general approach for quantifying the benefit of distributed power electronics for fine grained MPPT in photovoltaic applications using 3-D modeling," *IEEE Transactions on Power Electronics*, vol. 27, no. 11, pp. 4656–4666, 2012.

[22] R. C. Pilawa-Podgurski and D. J. Perreault, "Submodule integrated distributed maximum power point tracking for solar photovoltaic applications," *IEEE Transactions on Power Electronics*, vol. 28, no. 6, pp. 2957–2967, 2013.

[23] R. H. Wills, S. Krauthamer, A. Bulawka, and J. P. Posbic, "The ac photovoltaic module concept," in *Energy Conversion Engineering Conference, 1997. IECEC-97., Proceedings of the 32nd Intersociety*, vol. 3, pp. 1562–1563, IEEE, 1997.

[24] Q. Li and P. Wolfs, "A review of the single phase photovoltaic module integrated converter topologies with three different dc link configurations," *IEEE Transactions on Power Electronics*, vol. 23, no. 3, pp. 1320–1333, 2008.

[25] R. W. Erickson and A. P. Rogers, "A microinverter for building-integrated photovoltaics," in *Applied Power Electronics Conference and Exposition, 2009. APEC 2009. Twenty-Fourth Annual IEEE*, pp. 911–917, IEEE, 2009.

[26] A. Trubitsyn, B. J. Pierquet, A. K. Hayman, G. E. Gamache, C. R. Sullivan, and D. J. Perreault, "High-efficiency inverter for photovoltaic applications," in *Energy Conversion Congress and Exposition (ECCE), 2010 IEEE*, pp. 2803–2810, IEEE, 2010.

[27] D. Meneses, O. Garcia, P. Alou, J. Oliver, R. Prieto, and J. Cobos, "Single-stage grid-connected forward microinverter with constant off-time boundary mode control," in *Applied Power Electronics Conference and Exposition (APEC), 2012 Twenty-Seventh Annual IEEE*, pp. 568–574, IEEE, 2012.

[28] D. Shmilovitz and Y. Levron, "Distributed maximum power point tracking in photovoltaic systems-Emerging architectures and control methods," *automatika*, vol. 53, no. 2, pp. 142–155, 2012.

[29] P. S. Shenoy, K. A. Kim, B. B. Johnson, and P. T. Krein, "Differential power processing for increased energy production and reliability of photovoltaic systems," *IEEE Transactions on Power Electronics*, vol. 28, no. 6, pp. 2968–2979, 2013.

[30] K. A. Kim, P. S. Shenoy, and P. T. Krein, "Converter rating analysis for photovoltaic differential power processing systems," *IEEE Transactions on Power Electronics*, vol. 30, no. 4, pp. 1987–1997, 2015.

[31] C. Olalla, D. Clement, M. Rodriguez, and D. Maksimovic, "Architectures and control of submodule integrated dc–dc converters for photovoltaic applications," *IEEE Transactions on Power Electronics*, vol. 28, no. 6, pp. 2980–2997, 2013.

[32] P. Sánchez-Friera, M. Piliougine, J. Pelaez, J. Carretero, and M. Sidrach de Cardona, "Analysis of degradation mechanisms of crystalline silicon PV modules after 12 years of operation in southern europe," *Progress in photovoltaics: Research and Applications*, vol. 19, no. 6, pp. 658–666, 2011.

[33] A. M. Reis, N. T. Coleman, M. W. Marshall, P. A. Lehman, and C. E. Chamberlin, "Comparison of PV module performance before and after 11-years of field exposure," in *Photovoltaic Specialists Conference, 2002. Conference Record of the Twenty-Ninth IEEE*, pp. 1432–1435, IEEE, 2002.

[34] T. Shimizu, M. Hirakata, T. Kamezawa, and H. Watanabe, "Generation control circuit for photovoltaic modules," *IEEE Transactions on Power Electronics*, vol. 16, no. 3, pp. 293–300, 2001.

[35] Y. Nimni and D. Shmilovitz, "A returned energy architecture for improved photovoltaic systems efficiency," in *Circuits and Systems (ISCAS), Proceedings of 2010 IEEE International Symposium on*, pp. 2191–2194, IEEE, 2010.

[36] J. Stauth, M. Seeman, and K. Kesarwani, "A high-voltage CMOS IC and embedded system for distributed photovoltaic energy optimization with over 99% effective conversion efficiency and insertion loss below 0.1%," in *Solid-State Circuits Conference Digest of Technical Papers (ISSCC), 2012 IEEE International*, pp. 100–102, IEEE, 2012.

[37] I. E. Commission *et al.*, "Photovoltaic devices-part 1: Measurement of photovoltaic current-voltage characteristics," *IEC 60904-1*, 2006.

[38] I. E. Commission *et al.*, "Determination of the equivalent cell temperature (ECT) for photovoltaic (PV) devices by the open-circuit voltage method," *IEC norm*, no. 60904-5, 2011.

[39] J. Zoellick, "Testing and matching photovoltaic modules to maximize solar electric array performance," *Senior project presented to the Department of Environmental Resources Engineering Humboldt State University*, 1990.

[40] J. Konings and A. Habte, "Uncertainty evaluation of measurements with pyranometers and pyrheliometers," tech. rep., National Renewable Energy Lab. (NREL), Golden, CO (United States), 2016.

[41] D. Berman, S. Biryukov, and D. Faiman, "EVA laminate browning after 5 years in a grid-connected, mirror-assisted, photovoltaic system in the negev desert: effect on module efficiency," *Solar energy materials and solar cells*, vol. 36, no. 4, pp. 421–432, 1995.

[42] J. M. Bing, "Decades in the installed environment: do silicon modules really last more than 20 years," in *NREL PV Module Reliability Workshop*, 2010.

[43] G. G. Koch, S. Kotz, N. Johnson, and C. Read, "Encyclopedia of statistical sciences," *New York J Wiley*, vol. 213, p. 7, 1982.

[44] S. Pulver, D. Cormode, A. Cronin, D. Jordan, S. Kurtz, and R. Smith, "Measuring degradation rates without irradiance data," in *2010 35th IEEE Photovoltaic Specialists Conference*, pp. 001271–001276, IEEE, 2010.

[45] N. L. Johnson, S. Kotz, and N. Balakrishnan, "Continuous univariate distributions, vol. 2 of wiley series in probability and mathematical statistics: applied probability and statistics," 1995.

[46] J. R. Stedinger, "Fitting log normal distributions to hydrologic data," *Water Resources Research*, vol. 16, no. 3, pp. 481–490, 1980.

[47] C. Olalla, D. Clement, D. Maksimović, and C. Deline, "A cell-level photovoltaic model for high-granularity simulations," in *Power Electronics and Applications (EPE), 2013 15th European Conference on*, pp. 1–10, IEEE, 2013.

[48] B. Choi, "Differential power processing submodule integrated converters for photovoltaic power systems," *Ph.D. dissertation*, 2015.

[49] H. Jeong, H. Lee, Y.-C. Liu, and K. A. Kim, "Review of differential power processing converters techniques for photovoltaic applications," *IEEE Transactions on Energy Conversion*, 2018.

[50] T. Florencki and Y. Han, "High frequency resonant bidirectional sepic converter suitable for battery equalization and charger applications," in *Applied Power Electronics Conference and Exposition (APEC), 2014 Twenty-Ninth Annual IEEE*, pp. 2087–2092, IEEE, 2014.

[51] H. Choi and P. C. Team, "Design considerations for an LLC resonant converter," in *Fairchild Power Seminar*, pp. 82–3, 2007.

[52] D. Fu, *Topology investigation and system optimization of resonant converters.* PhD thesis, Virginia Tech, 2010.

[53] R. L. Steigerwald, "A comparison of half-bridge resonant converter topologies," *IEEE transactions on Power Electronics*, vol. 3, no. 2, pp. 174–182, 1988.

[54] R. W. Erickson and D. Maksimovic, *Fundamentals of power electronics*. Springer Science & Business Media, 2007.

[55] S. Abdel-Rahman, "Resonant LLC converter: Operation and design," *Infineon Technologies North America (IFNA) Corp.*, 2012.

[56] W. Chen, P. Rong, and Z. Lu, "Snubberless bidirectional dc–dc converter with new CLLC resonant tank featuring minimized switching loss," *IEEE Transactions on industrial electronics*, vol. 57, no. 9, pp. 3075–3086, 2010.

[57] J.-H. Jung, H.-S. Kim, J.-H. Kim, M.-H. Ryu, and J.-W. Baek, "High efficiency bidirectional LLC resonant converter for 380 V dc power distribution system using digital control scheme," in *Applied Power Electronics Conference and Exposition (APEC), 2012 Twenty-Seventh Annual IEEE*, pp. 532–538, IEEE, 2012.

[58] J. Caldwell, "Analog pulse width modulation," *TI precision Designs: Verified Design (Texas Instruments application recommendations)*, pp. 1–21, 2013.

[59] Fraunhofer Institute for Solar Energy Systems ISE, "Photovoltaics report,levelized cost of electricity renewable energy technologies," *[Online] Available here: www.ise.fraunhofer.de/en/publications/studies/photovoltaics-report.html.*, 2018.

[60] International Renewable Energy Agency (IRENA), "Renewable energy technologies: Cost analysis series," 2012.

UNIVERSITAT ROVIRA I VIRGILI
DISTRIBUTED POWER ELECTRONICS FOR EXTENDED EFFICIENCY AND LIFETIME OF UTILITY-SCALE PHOTOVOLTAIC SYSTEMS
MD Nazmul Hasan

Appendix A

Comparative Study Between the Ćuk and the LLC Converter for Very Low Power Applications

Conduction Loss of the LLC and the Ćuk Converter

With the aim of comparing the conduction losses in both converters, a loss model is developed in this section. For the LLC converter, a resistance of 200 mΩ is assumed for each primary and secondary winding of the transformer. No loss component is considered for the resonant inductors, since leakage inductance of the transformer of the LLC converter can be used as resonant inductor. In total 400 mΩ of loss resistance is included in both the analytical model and simulation. For the Ćuk converter, an equivalent resistance of 50 mΩ for each primary and secondary winding is considered. Another equivalent series resistance of 50 mΩ is taken for primary winding and 50 mΩ of loss resistance is considered for secondary winding for the coupled inductor. Therefore loss associated with the total resistance of 200 mΩ is considered as conduction loss for the Ćuk converter. The expressions of conduction loss for both converters are given below,

$$\text{LLC:} \qquad P_{cond} = I_{in,rms}^2 R_{pri,LLC} + I_{out,rms}^2 . R_{sec,LLC} \tag{A1}$$

$$\text{Ćuk:} \qquad P_{cond} = I_{L,1}^2 R_{L,1} + I_{L,2}^2 . R_{L,2} + I_{pri}^2 . R_{pri,cuk} + I_{sec}^2 . R_{sec,cuk} \tag{A2}$$

where,

I_{in} is the *rms* input current of the LLC converter,

I_{out} is the *rms* output current of the LLC converter,

$R_{pri,LLC}$ is the resistance of the primary winding of the transformer of the LLC converter,

$R_{sec,LLC}$ is the resistance of the secondary winding of the transformer of the LLC con-

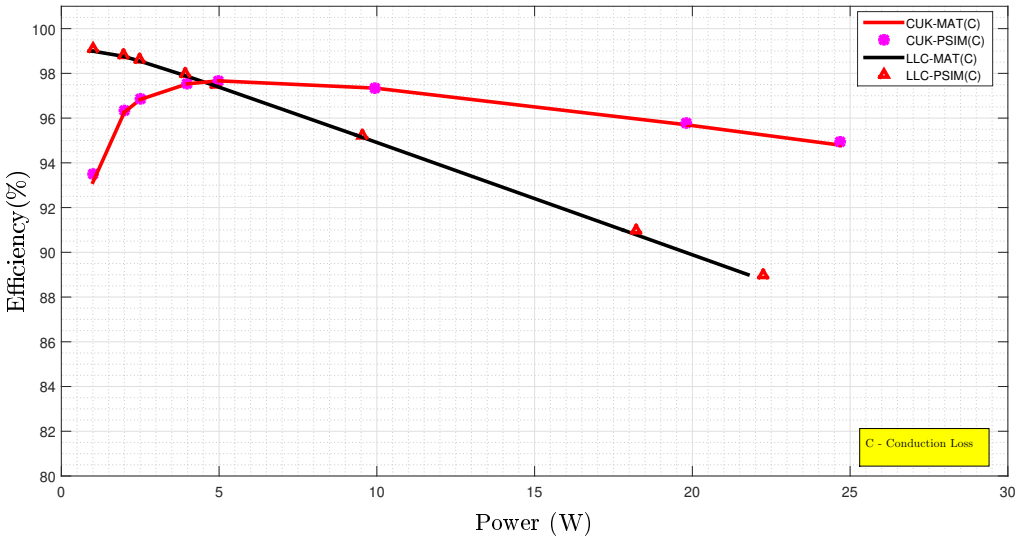

Figure A1. Efficiency comparison of the LLC and the Ćuk converter, considering conduction loss.

verter,

$I_{L,1}$ is the *rms* primary inductor current of the Ćuk converter,

$I_{L,2}$ is the *rms* secondary inductor current of the Ćuk converter,

$R_{L,1}$ equivalent series resistance of the primary inductor of the Ćuk converter,

$R_{L,2}$ equivalent series resistance of the secondary inductor of the Ćuk converter,

$R_{pri,cuk}$ is the resistance of the primary winding of the transformer of the Ćuk converter,

$R_{sec,cuk}$ is the resistance of the secondary winding of the transformer of the Ćuk converter.

Analytical expressions are derived to calculate efficiency of the LLC and the Ćuk converter. Later PSIM simulations are carried out with the same parameter to validate the mathematical model. Like the LLC converter, a total inductance of 25 µH is considered for the Ćuk converter. Since the Ćuk converter consists of two inductors, the total inductor has to be spited by two i.e. both primary and secondary side should contain 12.5 µH of inductance each. However, if the inductors can be combined in a single core, the effective inductance will be doubled. Therefore simulations and algorithms are constructed considering that the primary inductance is 25 µH and the secondary inductance is also 25 µH instead of 12.5 µH. Figure A1 shows the efficiency curves of the Ćuk and the LLC converter.

Gate Charge Loss and Switching Loss

In a switched mode power converter there are three types of losses associated with the switches. They are as follows,

- Gate charge losses due to charging and discharging the gate of the MOSFET.
- Conduction losses due to the drain to source 'ON' resistance of the MOSFET.
- Switching losses due to the non zero fall time and rise time of drain to source voltage and drain current respectively during turning 'ON'. Vice versa during turning 'OFF'.

As discussed in the previous section due to the leakage inductance, a high voltage transient appears across the switch of the Ćuk converter. Due to the circuit nature of the Ćuk converter, MOSFETs with relatively high voltage rating are required even if the power rating is the same as the LLC converter. For the investigation of gate charge and switching loss, two different MOSFET are selected for those two candidates. For instance, for the LLC converter PSMN6R125MLD MOSFET from NXP having voltage rating of 25 V and IPB123N10N3 MOSFET from Infineon having voltage rating of 100 V for the Ćuk converters are considered. To observe the effect of gate charge and switching loss on the efficiency of the converters, the simulations are carried out in LTspice (a simulation tool provided by Linear Technology).

Gate Charge Losses in MOSFET

The loss associated with the MOSFET due to the charging and discharging of the gate is called gate charge loss, which can be derived by the following equation,

$$P_{QG} = Q_{GTOT@VGDR} V_{GDR} F_{sw} \tag{A3}$$

where,

P_{QG} is the total gate charge losses, $Q_{GTOT@VGDR}$ is the total gate charge of the MOSFET at corresponding gate to source voltage, F_{sw} is switching frequency, V_{GDR} is gate driver supply voltage.

Table A1. Gate charge loss in MOSFETs.

MOSFET Part number	Total gate charge nC	R_{on} (mΩ) Typ.	Max.	V_{DS} mV	Calculated power mW	Simulation power mW
PSMN6R125MLD	10.7	6.46	7.24	14	25	11.225
PSMN6R125MLD	26	10.7	12.3	100	26/35	25.15

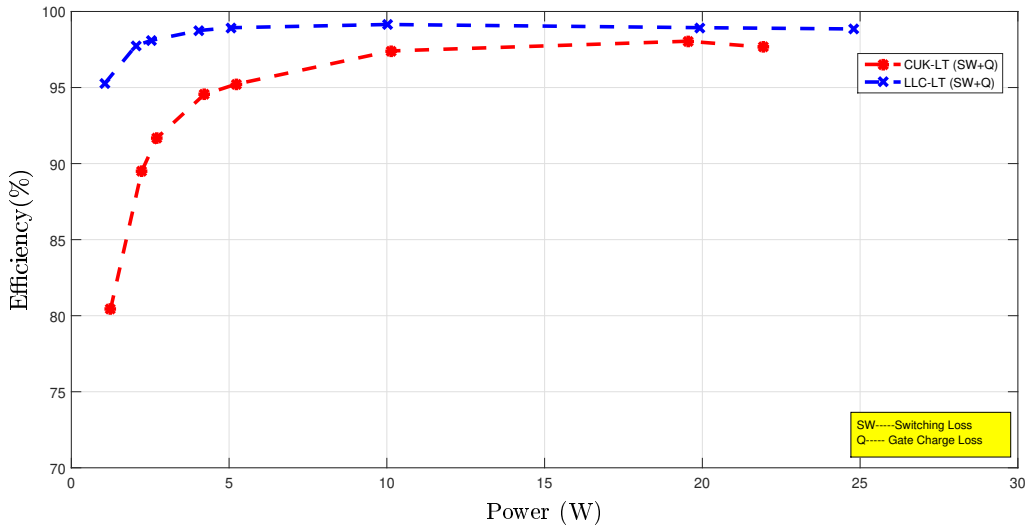

Figure A2. Efficiency comparison of the LLC and the Ćuk converter, considering switching and gate charge loss.

Switching Loss in MOSFET

Due to the overlapping of voltage and current during turn 'ON' and 'OFF' of the transistor, another type of power loss is produced in switching converters. Following the method described in [10], switching losses of a MOSFET can be calculated by the following equations,

$$P_{sw}(Inductive) = 0.5 V_{DD} I_D [T_{sw(on)} + T_{sw(off)}] \tag{A4}$$

$$P_{sw}(Resistive) = 0.25 V_{DD} I_D [T_{sw(on)} + T_{sw(off)}] \tag{A5}$$

where, $T_{sw(on)} = 0.5 \frac{V_{GDR} - V_{GP}}{R_{DR} + R_G}$,

$T_{sw(off)} = 0.25 \frac{V_{GDR} - V_{GP}}{R_{DR} + R_G}$,

V_{GP} is the plateau voltage,

V_{GDR} is the gate driver voltage,

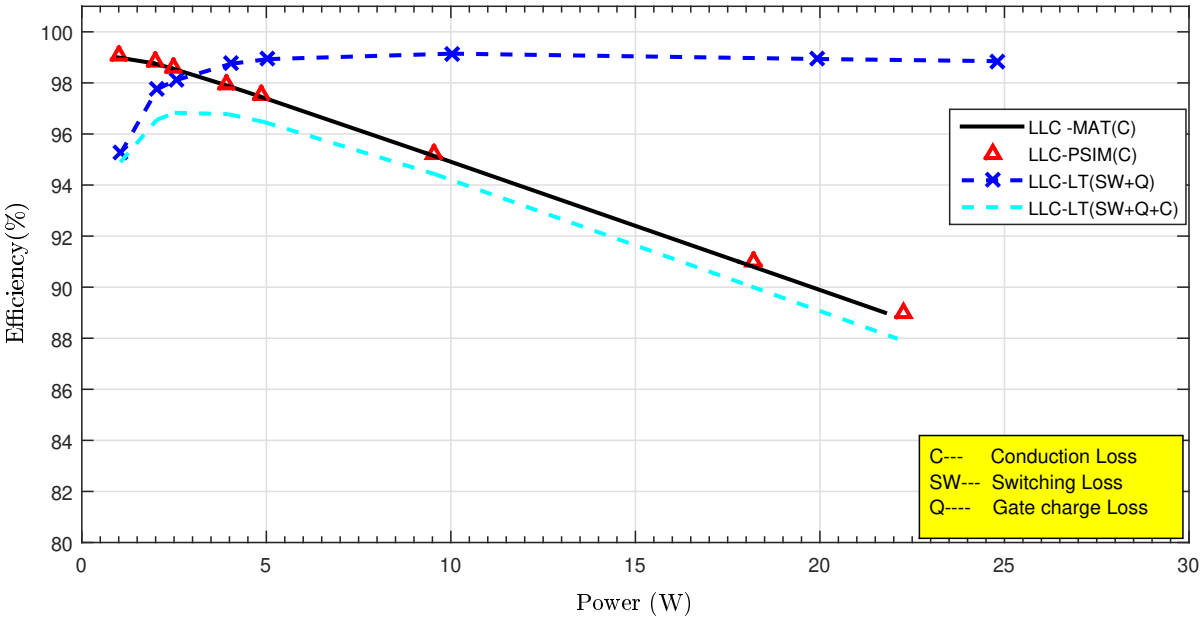

Figure A3. Performance of the LLC converter.

R_{DR} is the driver resistance,

R_G is the gate resistance of the MOSFET.

Figure A2 shows the efficiency of the LLC and the Ćuk converter considering gate charge and switching losses.

Conduction Loss, Gate Charge Loss and Switching Loss

In order to investigate the performance of the converters considering conduction, gate charge and switching losses, equivalent loss resistances as mentioned earlier are added and simulated again in LTspice. Figure A3 and Fig. A4 shows the efficiency of the LLC and the Ćuk converter with switching, gate charge and conduction losses respectively. Another reason of selecting relatively high voltage rated MOSFET for the Ćuk converter is that due to the leakage inductance, large voltage spike appears across the switch of the Ćuk converter. On the contrary, MOSFET with relatively small voltage rating with low gate charge and, turn 'ON', turn 'OFF' time is selected for the LLC resonant converter.

Leakage Inductance of the Ćuk Converter

Leakage inductance exhibited by the transformer plays an important role on the performance of the Ćuk converter. For instance, switches with higher voltage ratings are

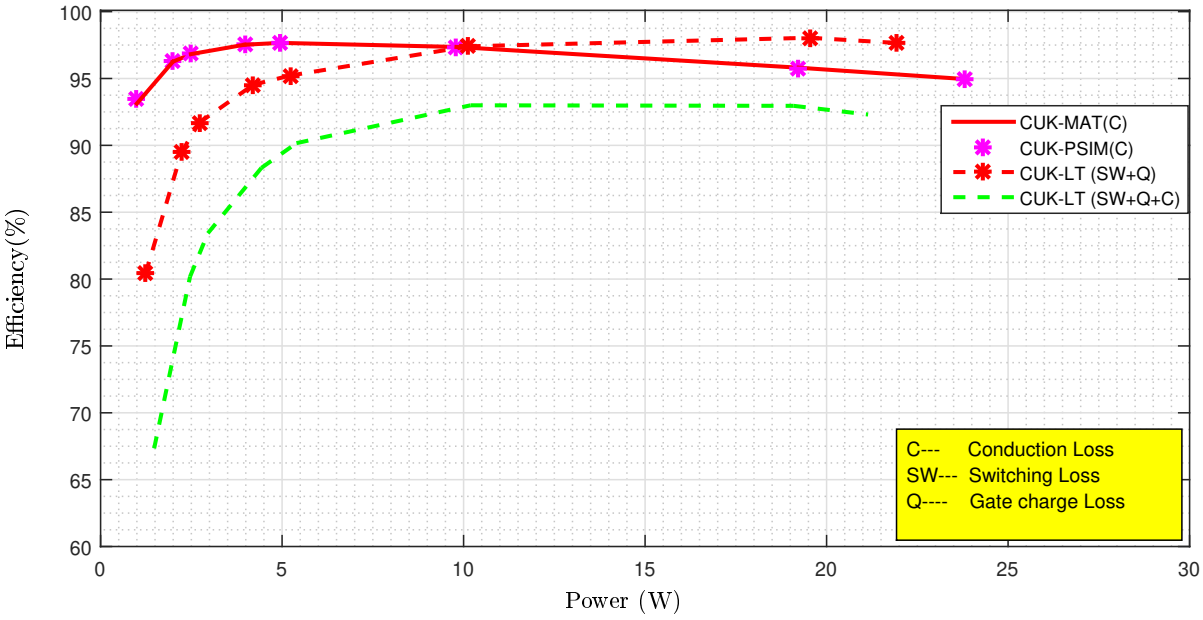

Figure A4. Performance of the Ćuk converter.

required which increase the size and cost of the converter. In addition to that, due to the leakage inductance, efficiency of the converter is affected severely, specially at light loads. In order to observe the effect of leakage inductance on the efficiency of the Ćuk converter, a simulation is carried out considering 96% coupling coefficient of the transformer and the result is presented in Fig. A5.

Total Loss

Figure A6 combines conduction, gate charge and switching losses of the LLC converter and in addition to all these losses for the Ćuk converter, leakage inductance losses is also shown. In that figure, it can be seen that from 1 W to 15 W the LLC converter provides a very good efficiency of more than 90%. In contrast, at low power from 1 W to 8 W the Ćuk converter provides less than 90% efficiency. At very low power, for example, for 1 W, the Ćuk converter provides only around 63% efficiency. This is because the switching loss is comparatively more significant at low power. Since ZVS can be achieved in the LLC converter, it exhibits very good efficiency at low power.

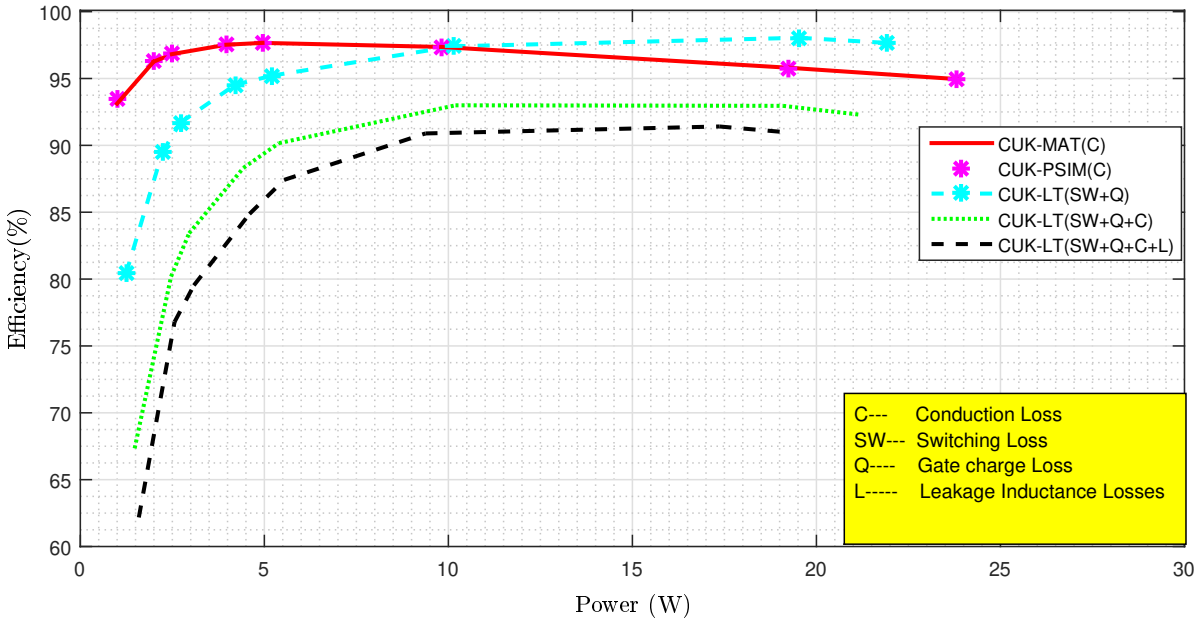

Figure A5. Performance of the Ćuk converter with 96% coupling coefficient. Conduction loss by analytical model (red line), conduction loss by PSIM (magenta *), switching loss and gate charge loss by LTspice (dashed * cyan), combined conduction, gate charge loss and switching loss in LTspice (green dot), and conduction loss, gate charge, switching loss and the effect of coupling coefficient in LTspice (dashed black).

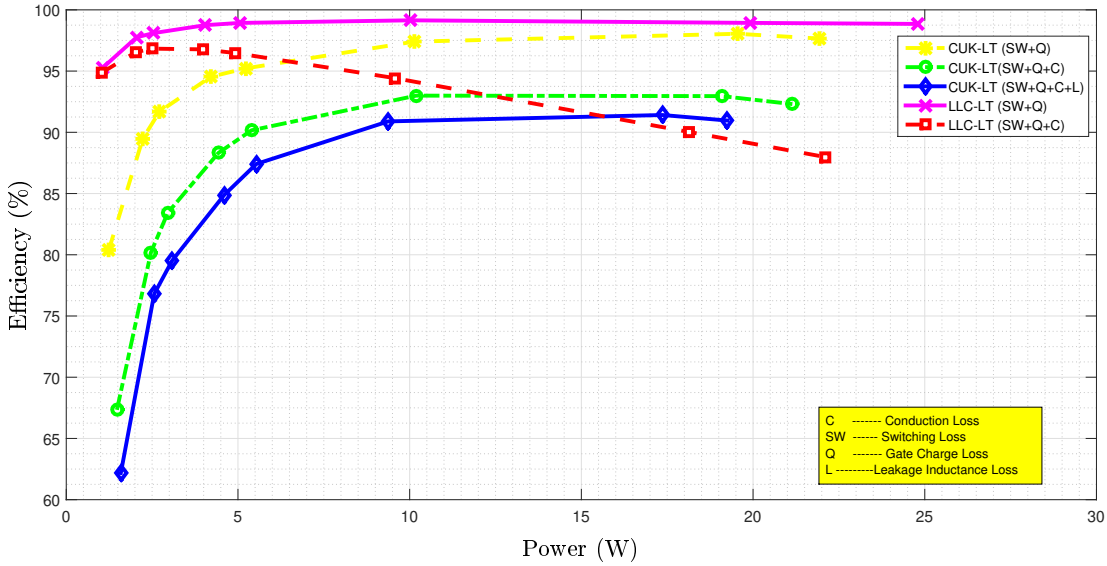

Figure A6. LTspice simulation of the performance of the LLC and the Ćuk converter. Switching loss and gate charge loss of the LLC (solid magenta x), combined conduction, gate charge loss and switching loss of LLC (dashed red square), switching loss and gate charge loss of the Ćuk (dashed * yellow), combined conduction, gate charge and switching loss of the Ćuk (green dashed-dot o), and conduction loss, gate charge, switching loss and effect of coupling coefficient in LTspice of Ćuk (solid blue diamond).

UNIVERSITAT ROVIRA I VIRGILI
DISTRIBUTED POWER ELECTRONICS FOR EXTENDED EFFICIENCY AND LIFETIME OF UTILITY-SCALE PHOTOVOLTAIC SYSTEMS
MD Nazmul Hasan

2019

Distributed Power Electronics for Extended Efficiency and Lifetime of Utility-Scale Photovoltaic Systems

MD NAZMUL HASAN

DOCTORAL THESIS

UNIVERSITAT
ROVIRA i VIRGILI